Science of Remote Sensing 11 (2025) 100187

Contents lists available at ScienceDirect

Science of Remote Sensing

journal homepage: www.sciencedirect.com/journal/science-of-remote-sensing

Detecting shallow subsurface anomalies with airborne and spaceborne remote sensing: A review

Adam M. Morley *, Tamsin A. Mather, David M. Pyle, J-Michael Kendall

Department of Earth Sciences, University of Oxford, South Parks Road, Oxford, OX1 3AN, UK

ARTICLE INFO

Keywords:
Remote sensing
Subsurface
Airborne
Spaceborne
Photogrammetry
Multispectral
Thermal
Hyperspectral
Gravity
Aeromagnetic
LiDAR
SAR
Archaeological
Environmental
Exploration
Defence
Speleological

ABSTRACT

Advances in air and space sensor technology reveal new opportunities and innovative ways to remotely sense the Earth's subsurface. Considerable spatial coverage, fast and frequent image acquisition and very high radiometric, spectral, spatial and temporal resolution imaging systems can now detect near subsurface anomalies with impressive accuracy. The merits are extensive, with archaeological prospecting, environmental risk mitigation, natural resource exploration, defence and security and speleological research all benefitting from subsurface imaging capabilities over unknown territory, difficult terrain, hazardous environments and inaccessible ground. In this paper, we categorise the ground indicators and potential field characteristics of a general subsurface anomaly before reviewing and documenting over seventy air and space subsurface detection techniques using: photogrammetry, multispectral sensors, thermal infrared, hyperspectral imaging, synthetic aperture radar (SAR), airborne light detection and ranging (LiDAR), airborne gravity and aeromagnetics. The capabilities of each technique are evaluated by reviewing their ability to detect specific characteristics from subsurface anomalies and then they are tabulated by investigable feature and sensor type in seven technique tables. Research trends in motive, sensor type and subsurface anomaly characteristic are discussed and a short review of the major ground-truthing techniques used to verify airborne and spaceborne observations is considered. To close, we take a brief look at future research opportunities with very high resolution (VHR) datasets, multi-branch convolutional neural networks (CNNs) and active remote sensing in variable potential fields.

1. Introduction

Remote sensing is a field of techniques which use non-direct contact devices from land, air and space to observe targets of interest on or below the Earth's surface (Omali, 2021). In this review, we consider the applications and techniques of airborne and spaceborne remote sensing to identify subsurface anomalies where, for the purpose of this research, the subsurface is defined as the region immediately below the Earth's surface, and extending tens or hundreds of metres below ground level. We appraise the value of rapid image acquisition, large spatial coverage and high spectral, spatial, radiometric and temporal resolution datasets across 113 academic papers and 91 use cases (Fig. 1). These use cases vary, representing different examples of subsurface detection in archaeological prospecting, environmental risk mitigation, natural resource exploration, defence and security and speleological research. Given this diversity, we generically define a subsurface anomaly as a near-surface causative body constituting: 1). different material properties to that of the surrounding soil and rock; 2). a different density; 3). a different magnetic susceptibility. If the subsurface anomaly is geologic, the anomalous structure is usually hundreds of metres deep, adopting numerous forms like dyke intrusions, ore deposits, volcanic conduits, karstic caves, salt domes, buried valleys, structural faults, fracture zones, granite plutons, shallow hydrocarbon prospects and geothermal reservoirs. However, if the subsurface anomaly is anthropogenic, it is generally much shallower, usually existing at depths of 1–10 m and rarely deeper than 50 m. Although our compilation is not exhaustive, we find that anthropogenic subsurface anomalies presented in the published literature are typically buried archaeological features, pipelines, drainage systems, tunnels, mines, adits, buried trenches and landfills.

Some of the most common, versatile and accessible forms of air and space remote sensing use photogrammetry and multispectral imagery to detect subsurface irregularities (Pisani and De Waele, 2021). Over the past 20 years, the potential of thermal and hyperspectral imagery,

* Corresponding author.
E-mail address: adam.morley@stx.ox.ac.uk (A.M. Morley).

https://doi.org/10.1016/j.srs.2024.100187
Received 13 September 2024; Received in revised form 5 December 2024; Accepted 20 December 2024
Available online 24 December 2024

airborne light detection and ranging (LiDAR), synthetic aperture radar (SAR), airborne gravity and aeromagnetics have become well recognised and widely applied as subsurface remote sensing techniques (Casana et al., 2017; Chen et al., 2017; Fairhead et al., 2017; Jia et al., 2020; Luo et al., 2019). Consequently, shallow subsurface features are now identified from numerous air and space sensor types in significant degrees of detail and assurance.

Recent advances in platform and sensor technology, data processing algorithms and open access data policies have begun to unlock the true potential of air and space remote sensing. Airborne and spaceborne optical sensors can acquire data at very high spatial, spectral, radiometric and temporal resolution, unlocking the ability to process, analyse and interpret high-quality 2D and high-density 3D data from remote platforms (Gruen, 2021). For example, Airbus' Pléiades Neo satellite constellation is capable of acquiring panchromatic images at 0.3 m spatial resolution and six-band multispectral images at 1.2 m resolution (Appendix A). Planet's Super Dove constellation is one of several multispectral revisit platforms, providing a continuous eight-band spaceborne view of the entire Earth's surface every day (Sakuma and Yamano, 2020). Similarly, since the development of new SAR imaging modes, the spatial resolution of SAR has dramatically increased (Appendix B), unlocking new subsurface detection capabilities. There are numerous high-resolution satellite missions (e.g., TerraSAR-X, TanDEM-X, COSMO-SkyMed, ICEYE, Capella X-SAR) which acquire imagery in different acquisition modes (e.g., stripMap, spotlight, scanSAR) and different polarisations (Tapete and Cigna, 2019), achieving spatial resolutions of 1 m or less (Table B1 and Figure B1).

Such advances in sensor technology and data acquisition present new opportunities to apply sophisticated remote sensing capabilities to challenging subsurface detection problems like the remote detection of: subsurface magmatic features and volcanic conduits (Biondi, 2022), cross border tunnel excavation (Perez et al., 2017), ancient settlements (e.g., Dana Negula et al., 2020), unexplored cave systems (e.g., Moyes and Montgomery, 2019), geothermal potential (Abdel Zaher et al., 2018), mining activity (Ammirati et al., 2020), ore deposits (El-Raouf et al., 2023) and underground coal fires (e.g., Du et al., 2022).

To date, there is no review of the utility and success of detecting geological *and* anthropogenic structures below ground with airborne and spaceborne remote sensing. Until now, single imaging techniques from a lone sensor type or single application are most common. More recently, research has begun to explore datasets from multiple sensor types but again, the application of various remote sensing techniques therein is only considered in one particular research field. Given the recent advances in aircraft, satellite and sensor technology, it is timely to: 1) collectively review the effectiveness of general subsurface detection from air and space; 2) assemble useful air and space subsurface detection techniques from major sensor types; 3) identify research trends in motive, sensor type and subsurface anomaly characteristics.

By reviewing 113 academic papers and 91 use cases (Fig. 1), our study reveals the principal motivations for remote sensing the subsurface. The paper then introduces a categorisation scheme for the specific ground indicators and potential field characteristics of a subsurface anomaly, setting the conditions for a systematic appraisal of remote subsurface detection using airborne and spaceborne: photogrammetry, multispectral, thermal and hyperspectral imaging, SAR, airborne LiDAR, airborne gravity and aeromagnetics. The application of various datasets

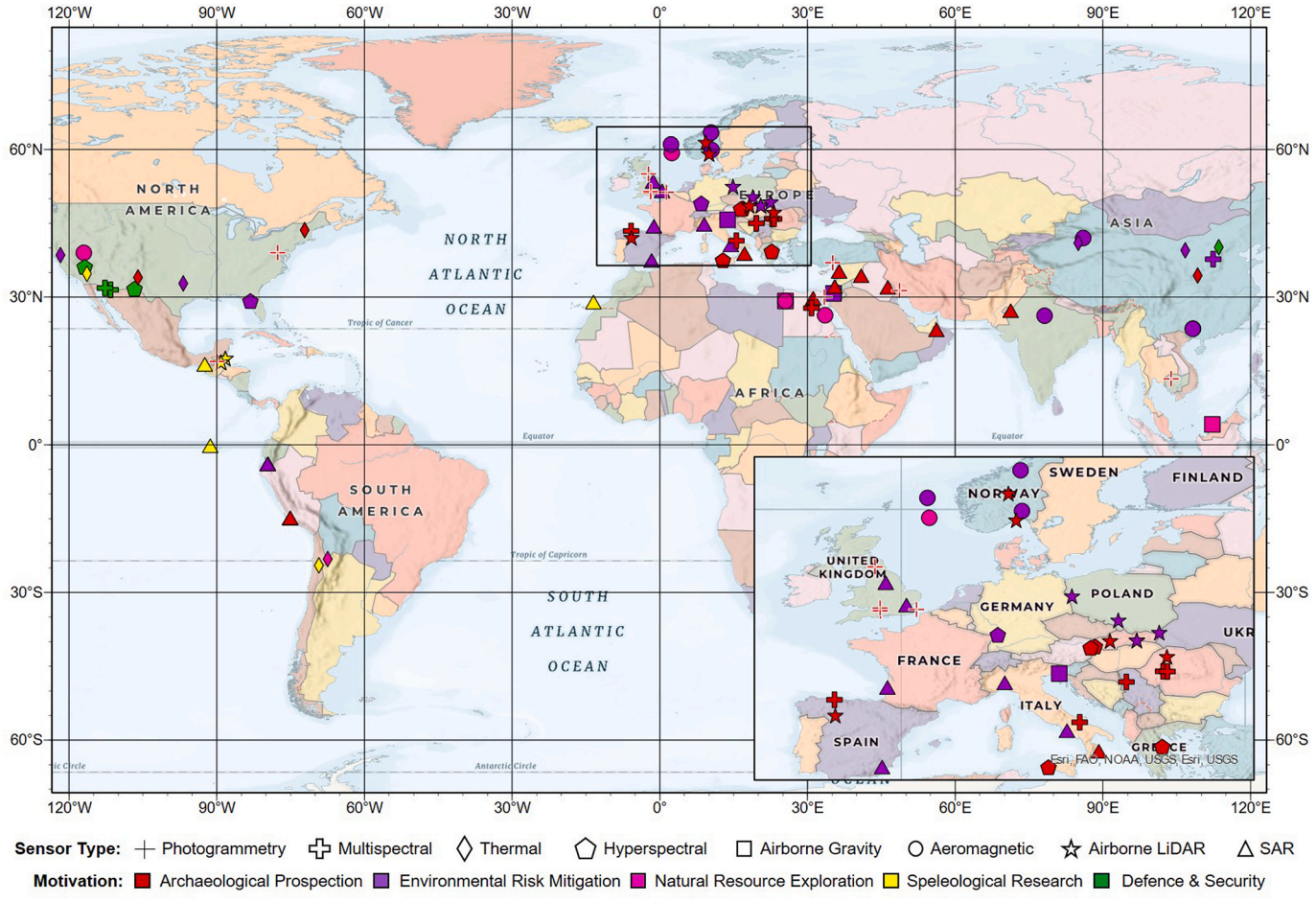

Fig. 1. Location of subterranean sites (use cases) reviewed in this paper, showing the remote sensor used (symbol shape – as shown in the legend) and the motive for their detection (symbol colour – as shown in the legend).

from each sensor type are reviewed in separate sections, ordered by the subsurface characteristic being investigated and then by the type of sensor used. The various subsurface detection techniques for each sensor are documented in a series of technique tables, initially structured by the subsurface anomaly characteristic being pursued and then the investigable feature being studied. Major research trends in the utility and application of remote sensing the subsurface are then assessed. To close, the paper considers the major ground-truthing techniques needed to verify air and space observations followed by a brief examination of some promising future research themes.

2. Motivations for remotely sensing the subsurface

From air and space, five overarching motivations for remote sensing the subsurface have been identified in this review (Fig. 2). Each research motive is discussed in descending order of prevalence, acknowledging our assumption that the sample of papers reviewed is representative of the body of subsurface remote sensing publications. The specific number of papers reviewed in support of each motivation and supporting statistics are presented in Figure C1 (Appendix C), where search strings were used to systematically trawl for publications by sensor category and subsurface target type.

2.1. Archaeological prospecting

The most popular research motive (38% of the papers reviewed) is archaeological prospecting. Here, the detection, cataloguing, differentiation and classification of ancient subsurface structures and the gathering of information, at scale and at speed, is greatly beneficial to the archaeological research community (Luo et al., 2019). Airborne and spaceborne remote sensing can unlock the ability to conduct large scale archaeological investigations without expensive (and sometimes impossible due to scale or location) field studies. This reduces the need for pedestrian survey in the early phases of an archaeological project and enables archaeologists to detect and prioritise prospective sites before deploying.

As discussed by authors like El-Behaedi (2021), air and space remote sensing is a useful means to detect, classify and monitor archaeological sites without significant ground disturbance or destruction to the archaeological area. Harnessing air and space remote sensing techniques also allows archaeologists to conduct large scale archaeological investigations over areas which are often inaccessible by foot, broadening the number, type and size of landscape in which they are able to conduct archaeological research (Pisani and De Waele, 2021). From a preservation perspective, quick and frequent spaceborne acquisition methods allow an archaeologist to locate, manage and preserve cultural heritage sites from urbanisation, industrialisation, looting and rising water levels (Dana Negula et al., 2020; Trier et al., 2015; Trier and Pilø, 2012). Aerial and spaceborne studies of archaeological features may also reveal spatial characteristics and geometrical relationships with surrounding archaeological sites; observations which would often be imperceptible from the ground (Zanni and De Rosa, 2019).

2.2. Environmental risk mitigation

One of the most diverse research motives in airborne and spaceborne remote sensing of the subsurface is environmental risk mitigation (31% of appraised papers). The use of various remote sensing techniques to locate sinkholes, shake holes, swallow holes, soil pipes and land subsidence in karstic rich environments and above voids is a popular research objective (Barla et al., 2016; Bernatek-Jakiel and Jakiel, 2021; Hofierka et al., 2018; Zhang et al., 2023). Once detected, air and space remote sensing can be used to monitor the spatial extent and depression rate of ground subsidence in order to manage and mitigate any adverse impacts on urban development projects, tunnel construction and agronomic productivity (Bonì et al., 2017; Braitenberg et al., 2016; Sun et al., 2023). Other remote sensing objectives include the detection and behaviour of underground coal fires and sand dune migration (Du et al.,

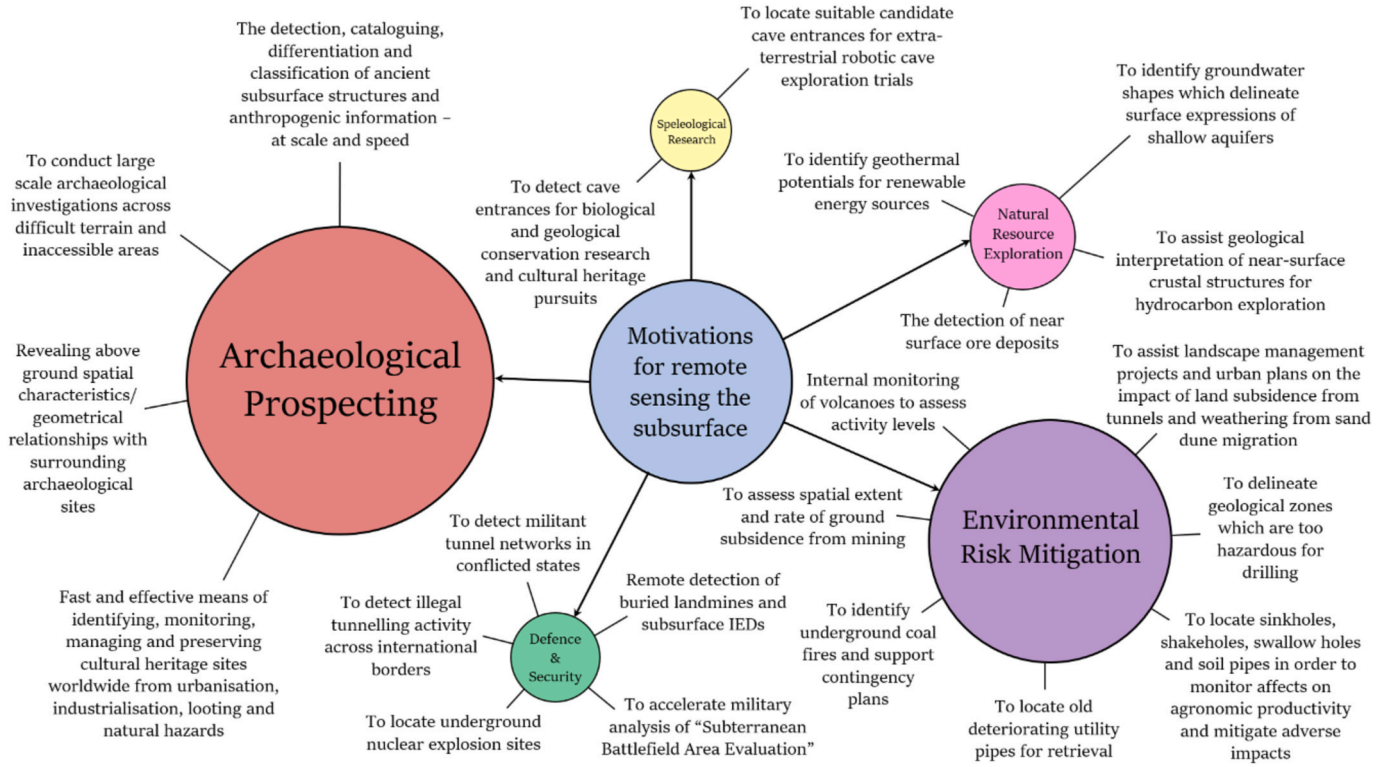

Fig. 2. Motivations for remote sensing the subsurface; motivation bubble is proportional, in size, to the quantity of papers appraised in this review as per the paper statistics in Figure C1, Appendix C.

2022; Grandjean et al., 2001; Wang et al., 2015), the internal monitoring of volcanoes (Biondi, 2022) and the identification of specific geological structures which present drilling hazards during exploration programmes e.g. tunnel valleys containing shallow gas (Ottesen et al., 2020).

Hartshorn et al. (2022) present an interesting use case for the aerial detection of old utility pipes which, prior to retrieval, can have a detrimental effect on nearby ground conditions. Alternatively, Kuzia (2018) and Mi et al. (2019) consider the utility of airborne and spaceborne remote sensing to monitor the secondary impacts of underground mining.

2.3. Natural resource exploration

The remote detection of near-surface natural resources comprises 13% of the academic papers reviewed in this study. Research objectives include the detection and demarcation of subsurface ore deposits (El-Raouf et al., 2023) and the remote identification of shallow geothermal regions; the former supporting national economic levels and the latter supporting national ambitions to transition to renewable energy sources (Abdel Zaher et al., 2018). Air and space remote sensing techniques are also seen to detect unique groundwater shapes, patterns, tones and textures, revealing drainage patterns and surface lineament characteristics which delineate surface expressions from shallow aquifers (Gaber et al., 2020; Waters et al., 1990). This research motive also reveals the utility of airborne and spaceborne remote sensing as an augmentation toolset, where the execution of niche acquisition surveys like airborne gravity can assist with the geological interpretation and characterisation of crustal structures like faults, fracture zones, domes and tunnel valleys, all in direct support of shallow-subsurface hydrocarbon exploration (Jamaludin et al., 2021).

2.4. Defence and security

In total, 11% of the papers appraised in this review present a defence and security research motive. Given the sensitive nature of these applications, other studies will exist but are not necessarily published openly in international journals. Among the most important of these applications is that of tunnel detection, where the motivation to detect clandestine tunnel activity under built-up areas and international borders is considerable.

In conflict, tunnels allow combatants to move between fighting positions safely and freely. Urban tunnel networks and more widely, cross border tunnels (CBTs), also provide covert lines of communication for transporting hostages, human trafficking, asylum seekers and drug smuggling. They are also useful for the concealment of weapons, soldiers, insurgents, food and water supplies (Richemond-Barak, 2018). In modern-day conflict, CBTs are specifically known to exist between Israel and Lebanon; Israel and Syria; Israel and Gaza; Egypt and Gaza; North and South Korea; Cambodia and Vietnam; US and Mexico; India and Pakistan (Olson and Speidel, 2020; Richemond-Barak, 2018).

Airborne and spaceborne remote sensing are useful for several defence and security-related applications. These techniques can, at scale and at speed, locate and prevent hostile militant activity and clandestine CBT exchanges by employing specialised change detection techniques (Kwan, 2019) and feature detection algorithms like the identification of excavated spoil heaps (Perez et al., 2017). Further, remote sensing is used to accelerate the military analysis of 'subterranean battlefield area evaluation', allowing armed forces to observe, orient, decide and act off the interpretation of high-resolution imagery that is up-to-date and readily available across the chain of command (Olson and Speidel, 2020). Additionally, multispectral and hyperspectral imagery is frequently used by various Defence and Government Intelligence experts to classify adversary vehicles, equipment and troops near tunnels and caves and under forested terrain and camouflage constructs (Shimoni et al., 2019). Pending burial depth and specific ground conditions, buried landmine and improvised explosive device (IED) detection is also achievable using specialist air and space remote sensing techniques (Shimoni et al., 2019). Similar specialism is also replicated by the Comprehensive Nuclear-Test-Ban Treaty Organisation (CTBTO) who can, during on-site inspections, perform multi-sensor subsurface detection routines to locate underground nuclear explosion sites (Mathew et al., 2023).

2.5. Speleological research

The effective employment of airborne and spaceborne remote sensing to detect cave entrances is the focus of 7% of the papers reviewed. The generation of various algorithms and workflows to detect candidate cave entrances (CCEs) offer several advantages to speleological research. For example, the detection of new cave systems in select and often restricted parts of the world can accelerate research prospects for conservation biologists and geologists, recognising that caves can host rare species, fragile ecosystems and unusual geological formations (Wynne et al., 2021). In support of speleological studies and ancient cultural heritage investigations, the ability to detect cave systems remotely in steep and rugged terrain, dense vegetation and relatively remote regions of the world is extremely beneficial (e.g. Moyes and Montgomery, 2019). Here, the remote detection of CCEs allows specific sites to be prioritised for follow-up ground investigation and in parallel, suitable access routes can be identified using the remotely sensed imagery (Weishampel et al., 2011).

In order to inform future robotic cave exploration missions on extra-terrestrial bodies like the Moon and Mars, the need to detect suitable CCEs on Earth is also gaining momentum. Several papers in this review employ air and space remote sensing techniques to identify suitable cavernous training sites for robotic exploration trials (Carrer et al., 2015). The motivation to explore extra-terrestrial caves is multifaceted. Research objectives include: the search for water, dry ice, brines and organic matter, the need to understand the subsurface geology of extra-terrestrial bodies and the detection of prospective human outposts safe from cosmic radiation (Pisani and De Waele, 2021).

3. Characterisation of subsurface anomalies

Whether natural or anthropogenic, shallow structures and objects beneath the Earth's surface can produce unique ground characteristics and surface proxies directly above the ground anomaly, which can then be used for detection. We group these distinct subsurface anomaly characteristics into seven categories: 1). visual identification; 2). soil matrix irregularity; 3). anomalous groundwater behaviour; 4). surface elevation change; 5). heat retention anomaly; 6). subsurface density change; 7). magnetic field variation. The field observations related to each category are reviewed in the following subsections, summarised in Table 1 and illustrated in Fig. 3.

3.1. Visual identification

Several visible features on and above the ground can signify the presence of subsurface structures and underground anthropogenic activity. By definition, these are visible indicators which can be seen in situ with the naked eye or, pending the spatial resolution of the air or spaceborne remote sensor, identified in visible Red-Green-Blue (RGB) imagery. Typical indicators include changes in land use and land cover (Mi et al., 2019), prominent and regular shaped crop marks (Melillos et al., 2019) and geomorphic surface anomalies like sinkholes (Hofierka et al., 2018), shake holes, soil pipes (Bernatek-Jakiel and Jakiel, 2021), lava tubes and skylights (Carrer et al., 2015). Pending the size of the opening and the amount of concealment, vertical and horizontal entrances to tunnels, mines and caves (Moyes and Montgomery, 2019) can also be detected remotely. Finally, any objects or features which depict clear signs of underground excavation are usually clear evidence of

Table 1
Ground indicators, potential field characteristics and typical field observations generated by a subsurface anomaly, as illustrated in Fig. 3.

Subsurface Anomaly Characteristic	Field Observations	Example References
Visual identification	Changes in land use/land cover; geomorphic surface anomalies (e.g. sinkholes, shake holes, soil pipes, lava tubes, skylights); prominent and regular shaped crop marks; entry points to tunnels, mines and caves; tunnelling indicators (e.g. new tracks, spoil heaps, tunnel boring machinery, plant vehicles, hand/power tools, field generators)	Carrer et al. (2015); Dao et al. (2017); Mi et al. (2019); Moyes and Montgomery (2019); Bernatek-Jakiel and Jakiel (2021)
Soil matrix irregularity	Crop marks – tall/vigorous over buried ditches, short/stressed over buried archaeological features, stone intrusions and lined tunnels; steady drainage, soil moisture content and soil composition over buried ditches; excessive drainage over buried features, stone intrusions and lined tunnels; soil marks; mineralogical modification from migration of leachates	Lasaponara and Masini (2007); Rowlands and Sarris (2007); Dana Negula et al. (2020); El-Behaedi (2021)
Anomalous groundwater behaviour	Lateral variations in rock permeability from excavation activity triggers fracturing and affects ground water percolation; altered groundwater regimes reveal anomalous drainage behaviour and lineament characteristics at the surface; underground voids can behave like drains, affecting groundwater level; alterations in chemical composition of soil affects water storage and recharge rates from infiltration	Grandjean et al. (2001); Finn et al. (2011); Waters et al. (2019); Gaber et al. (2020); Lv et al. (2020)
Surface elevation change	Micro-relief from near-surface features and soil degradation activity; land subsidence from superficial and deep deformations e.g. swelling/shrinkage of clay soils, soil consolidation, aquifer compaction, solid and fluid extraction; ground subsidence from mining and tunnelling	Barla et al. (2016); Bonì et al., 2017; Luo et al. (2019); Scoular et al. (2020); Macchiarulo et al. (2021)
Heat retention anomaly	Differential heating of Earth's surface from micro-relief variations; crop marks affecting heat retention due to variations in evapotranspiration; thermal inertia distinctions and thermal emissivity contrasts above subsurface structures and at tunnel, mine and cave entrances	Tan et al. (2006); Rowlands and Sarris (2007); Hill et al. (2020); Wynne et al. (2021)
Subsurface density change	Residual gravitational field strength anomalies (using microgravity profiling) from buried archaeological features, cave systems, tunnels, mines, adits, salt domes, buried valleys, structural faults, fracture zones, granite plutons, shallow hydrocarbon prospects and geothermal reservoirs	Braitenberg et al. (2016); Abdel Zaher et al. (2018); Jamaludin et al. (2021)
Magnetic field variation	Residual magnetic field strength anomalies from dykes, large basic intrusions, magnetite ore deposits, fracture zones, weak rock units, shallow hydrocarbon prospects, shallow geothermal reservoirs, buried pipelines, archaeological features, stone, steel or concrete lined tunnels and buried trenches/infills	Ottesen et al. (2020); Hartshorn et al. (2022); El-Raouf et al. (2023); Zhang et al. (2023)

subsurface activity. These include: the formation of new tracks in sensitive regions, spoil heaps, tunnel boring machinery, plant vehicles and field generators (Olson and Speidel, 2020).

3.2. Soil matrix irregularity

An ancient underground structure like a wall or a road, or the presence of a shallow stone-lined tunnel, will directly influence the soil structure above it (Dana Negula et al., 2020). Often poor and/or excessive drainage conditions are introduced to the soil matrix above an anthropogenic structure and geochemical alterations within the soil are intensified by the mineralogical leaching of the subsurface structure, which can exacerbate with time. This results in detrimental modifications to the soil density, soil moisture content and soil composition above and around a subsurface anomaly (Rowlands and Sarris, 2007). Consequently, the growth and health status of any vegetation at the surface is expected to deteriorate (Lasaponara and Masini, 2007). Furthermore, the presence of a very shallow underground structure is expected to restrict the absorption rates of chlorophyll, chlorophyll abundance and green leaf scattering in plants and grassland, because the subsurface anomaly will impede root development and disrupt soil salinity levels (Allbed and Kumar, 2013; James et al., 2020). Such activity will typically result in stressed crops (crop marks) and soil discolouration (soil marks) over buried anthropogenic structures and pronounced crop marks over buried ditches and paleo channels (Fig. 3). The vegetation response to soil matrix irregularity and subsurface heterogeneity is particularly useful for air and space remote sensing, where near-infrared (NIR) wavelengths are well reflected by vigorous vegetation and absorbed by stressed vegetation, and red wavelengths are absorbed by vigorous vegetation and well reflected by stressed vegetation (Luo et al., 2019).

3.3. Anomalous groundwater behaviour

Lateral variations in rock permeability from tunnel excavation and mining activity can activate fracturing, affecting groundwater percolation around tunnels and mines. According to Waters et al. (2019), underground tunnelling can trigger the formation of an excavation damage zone (Fig. 3) which contains a series of newly formed radial and concentric fractures around the excavation. In turn, these fractures are expected to redistribute the rock stress in the near-surface, realign rock crystal structures and reroute groundwater percolation regimes. In particular, underground voids (e.g. tunnels) can often behave like drains, accelerating and/or disrupting soil drainage rates which then locally change the groundwater level (Lv et al., 2020; Zeng et al., 2023). Subsequently, these altered groundwater regimes have the potential to reveal anomalous drainage behaviour and lineament characteristics at the surface. Furthermore, any geochemical alterations in the soil matrix around a geological and anthropogenic subsurface anomaly can affect the water storage and recharge rates from infiltration (Gaber et al., 2020), again resulting in anomalous drainage patterns and watersheds.

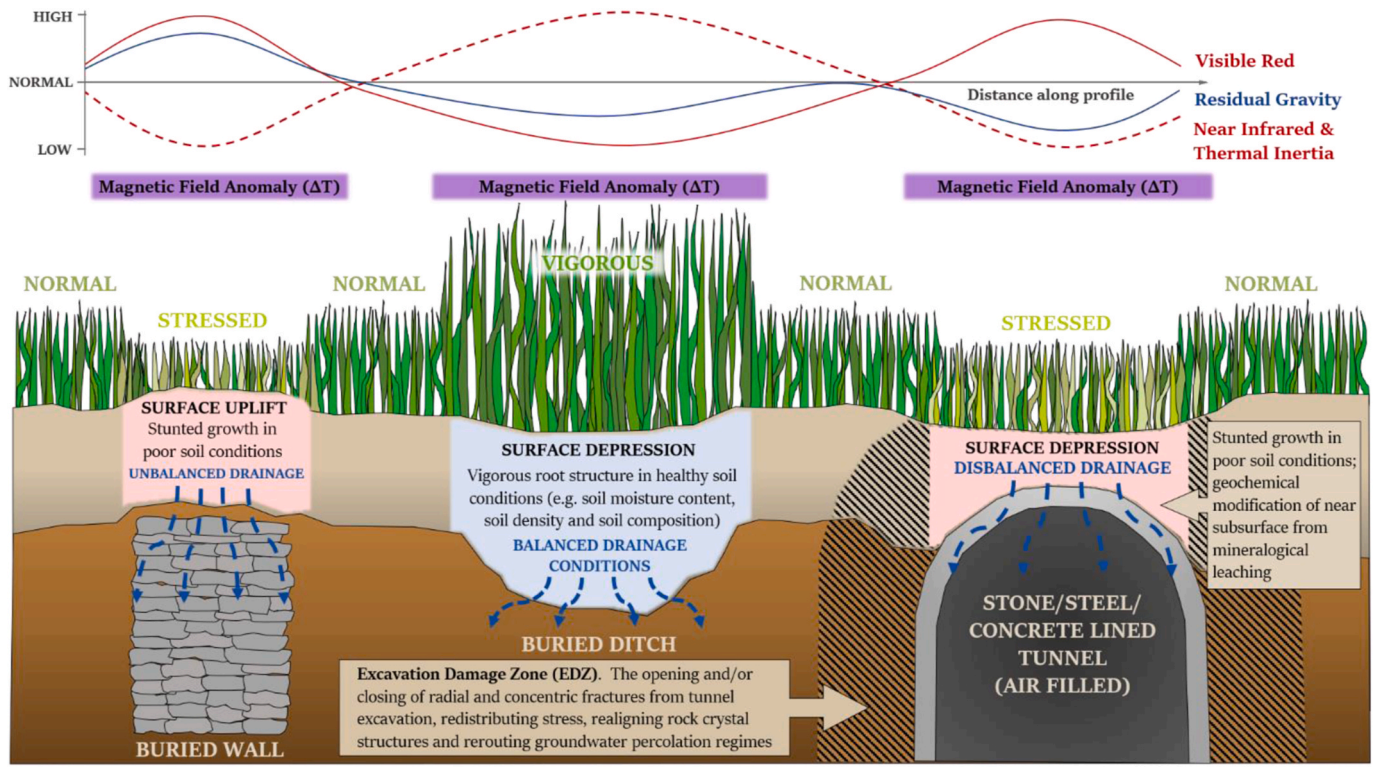

Fig. 3. Anomalous ground characteristics of three general subsurface structures that can be detected using remote sensing. An underground wall (left), buried ditch (centre) and air-filled tunnel (right) are used as examples. Top diagram illustrates how visible red light, near infrared, thermal inertia and residual gravitational field strength vary across these structures. Purple bars denote locations of total magnetic field anomalies (ΔT); ΔT is dependent on the subsurface distribution of magnetic susceptibility and the orientation of the Earth's Magnetic Field. Vegetation, micro-relief and drainage variations are also illustrated pictorially, although some or all may not be present in every real-world scenario.

3.4. Surface elevation change

Near-surface objects like archaeological remains and buried river channels may produce micro-relief variations along the Earth's surface (Chase et al., 2017). These small adjustments in surface elevation and topography are rarely noticed by the naked eye but aerial reconnaissance and high-resolution air and space remote sensing can reveal subtle height distinctions (Lieskovský et al., 2022). Soil degradation, soil consolidation, variable drainage rates and the swelling and shrinkage of clay soils around subsurface anomalies are expected to contribute to surface uplift and surface slumps over shallow subsurface features (Bernatek-Jakiel and Jakiel, 2021). Also, naturally occurring ground subsidence from deeper deformation activity, groundwater withdrawal, aquifer compaction and karstic behaviour can symbolise the presence of underground inconsistencies. In parallel, human induced land subsidence can trigger similar field observations, where anomalous surface depressions can signify the location of underground solid and fluid extraction, lateral and vertical mining activity and tunnel excavation (Anantrasirichai et al., 2021).

3.5. Heat retention anomaly

Micro-relief anomalies (e.g. localised surface depressions and ground uplift) above subsurface anomalies can instigate differential heating effects across a scene (James et al., 2020), where slopes directly facing the Sun capture more heat energy than slopes facing away from the Sun. Corrections must therefore be made for the Sun's azimuth, elevation and local ground conditions. Additionally, differences in the density, chemical composition and moisture content of the ground above a subsurface feature can cause the ground surface to absorb, emit, transmit and reflect thermal infrared (TIR) radiation at different rates from that of the surrounding ground (Casana et al., 2017). This is due to anomalous thermal emissivity contrasts in the subsurface, generated by the materials constituting that particular subsurface entity. Such anomalous geologic and anthropogenic entities have distinct diurnal radiant temperature curves which are defined by the subsurface anomaly's 'thermal conductivity', 'thermal capacity' and 'thermal inertia' (Lillesand et al., 2015). As illustrated in Fig. 3, this thermal inertia is a measure of the response of a material to temperature change and in general, subsurface features with high thermal inertia (e.g., buried ditches) express greater uniform surface temperatures throughout the day than subsurface bodies that introduce low thermal inertia properties into the surrounding ground (e.g., buried walls and air-filled tunnels). Crop marks created by shallow subsurface objects can also generate heat retention anomalies, where they express unique variations in evapotranspiration (Tan et al., 2006).

3.6. Subsurface density change

Geological and anthropogenic subsurface anomalies can be identified on the basis of variations in the Earth's gravitational field, arising from differences in density between the target subsurface object and the surrounding ground (Kearey et al., 2002). A causative subsurface structure like a large air-filled cave will present a lower density than its bulk 'soil and rock' surroundings, generating a subsurface zone of anomalous mass and a localised perturbation in the Earth's gravitational field known as a gravity anomaly (Milsom, 2003). A wide range of geological and anthropogenic settings will generate zones of anomalous mass which in turn, will produce residual gravitational field strength anomalies. Geological structures expected to generate residual gravitational field strength anomalies include caves, salt domes, buried valleys, structural faults, fracture zones, granite plutons, shallow hydrocarbon prospects and geothermal reservoirs (Jamaludin et al., 2021). Anthropogenic subsurface structures expected to generate residual

gravitational field strength anomalies include archaeological features, tunnels, mines and adits (Butler, 2008).

3.7. Magnetic field variation

Near-surface structures like concrete lined tunnels or ancient walls can present significant alterations in magnetic susceptibility (κ) underground. Magnetic susceptibility (κ) is a measure of how susceptible a material is to becoming magnetised (Persico et al., 2019). Depending on the concentration of ferro and ferro-magnetic minerals in the geological or anthropogenic subsurface anomaly, varying levels of magnetic susceptibility are introduced to the near-surface. Furthermore, this subsurface anomaly will, to a greater or lesser extent, feature an induced and remnant magnetisation different from the surrounding ground. Therefore, above the Earth's surface, these magnetisations will generate a resultant vector known as the 'intensity of magnetisation (J)' which is unique and representative of the underlying geological or anthropogenic body (Reynolds, 1997). When interpreting the magnitude and shape of the magnetic anomaly above the Earth's surface, it is important to understand that the resultant anomaly is a product of the interaction (superimposition) between the magnetic field of the subsurface body and the Earth's Magnetic Field (Campbell, 2003). Geological features which are expected to generate residual magnetic field strength anomalies include dykes, large basic intrusions, magnetite ore deposits, fracture zones, weak rock units, shallow hydrocarbon prospects, shallow geothermal reservoirs and faulted, folded and truncated lava flows (Everett, 2013). Anthropogenic structures which are expected to generate residual magnetic field strength anomalies include buried pipelines, buried archaeological features, stone, steel or concrete lined tunnels, buried trenches and landfills (Křivánek, 2017).

4. Remote sensing the subsurface: overview

Case studies demonstrating the remote detection of subsurface anomalies are considered systematically, ordered by the subsurface characteristic being investigated and then by the type of sensor used. All papers reviewed are documented in a three-dimensional reference matrix (Figure C1), where each paper is registered by sensor type, authors' motivation and the subsurface anomaly characteristic being pursued (Appendix C). In support of each section are a series of information graphics (Appendix D), each communicating the respective principles of the air and space remote sensors reviewed.

By assuming the 113 papers reviewed are representative of the total population of subsurface remote sensing publications, several trends in the utility and application of remote sensing the subsurface are revealed. As summarised in Fig. 4, 78% of reviewed photogrammetry papers study the visible indicators across archaeological sites; 43% of multispectral papers identify soil matrix irregularities over buried archaeological features; anomalous groundwater behaviour is analysed using 6/8 sensor types; heat retention anomalies are a suitable proxy for all research motives; changes in subsurface density are detected (or assisted) using airborne gravity, airborne LiDAR and SAR; 57% of LiDAR papers and 50% of SAR papers exploit changes in surface elevation.

In the remainder of this review, over 70 air and space subsurface detection techniques are summarised across seven technique tables. In each technique table, relevant acquisition methods and detection

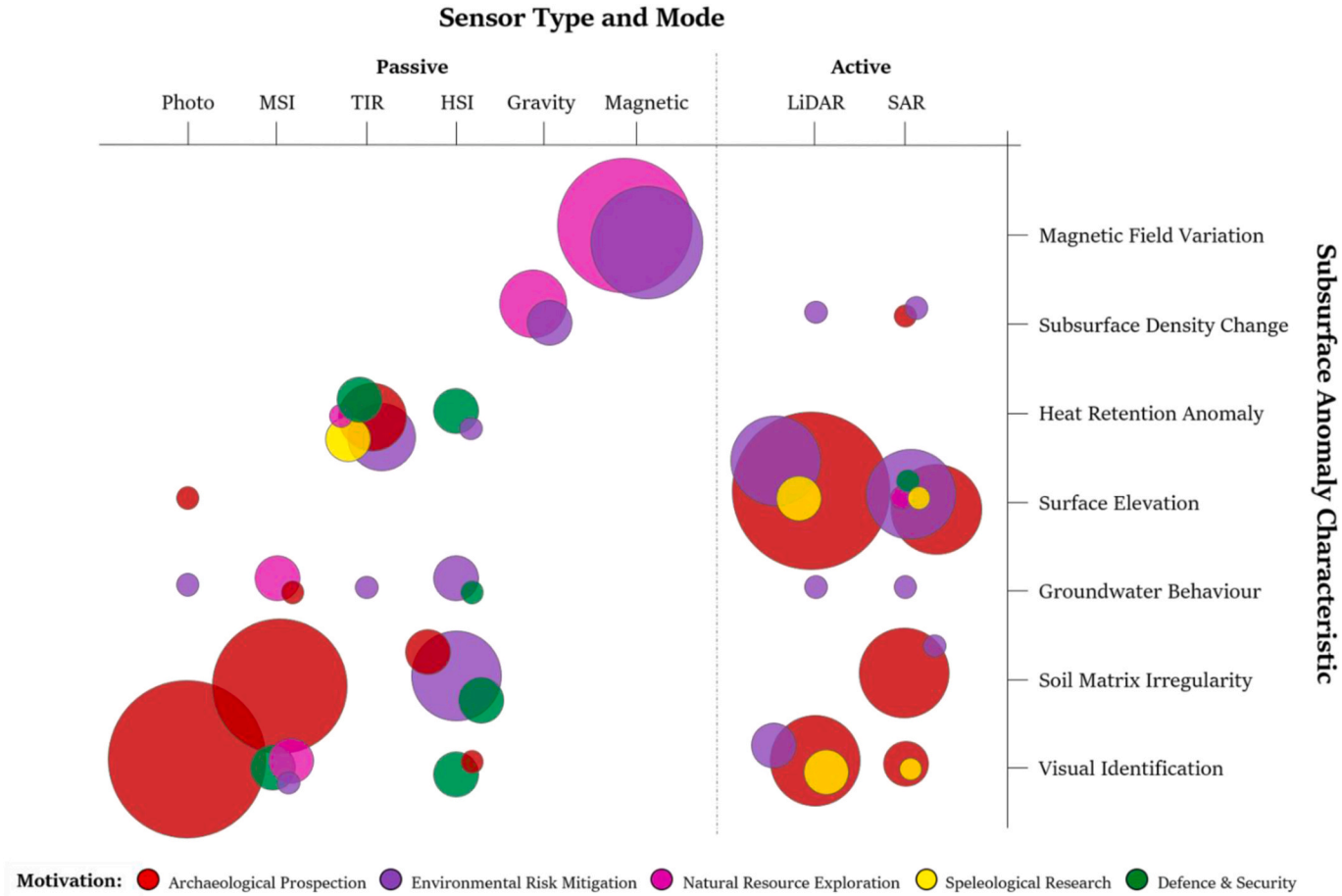

Fig. 4. Bubble chart showing the type of sensor used to detect the characteristics of subsurface anomalies for each paper in this review. The size and colour of the data bubble respectively represent the quantity of papers applicable and the author's primary motivation. In total, 113 papers were reviewed in six months. Specific paper counts and supporting statistics are recorded in Fig. C1, Appendix C.

techniques are documented by subsurface anomaly characteristic, investigable feature and sensor type. Our hope is that this organisation will maximise their value in priming future research and subsurface detection studies.

5. Visual identification

5.1. Using photogrammetry

When visually inspecting the ground for unique characteristics from subsurface features, the principles of photogrammetry can assist considerably. Examples include the detection and analysis of anomalous groundwater regimes over and around subterranean features (Sharafi and Khazaei, 2013) and the visual detection and geometrical measurement of micro-relief patterns, crop marks and soil marks (Lasaponara and Masini, 2014). In support of visually detecting micro-relief anomalies, air and space photography can also be used as stereopairs to create digital elevation models (Luo et al., 2019).

The benefits of using aerial photogrammetry in subsurface detection were first conceived in 1906 when archaeological features around the ancient UK monument of Stonehenge were identified from an aerial photograph taken from a military balloon (Bewley, 2003). Since then, developments in photography and aerial photogrammetry have accelerated and consequently, the discipline of 'aerial archaeology' began to flourish. By the 1970s, the use of infrared and multispectral photography started to detect variations in soil moisture and crop growth across historical sites (Verhoeven, 2012) and by the 1990s, aerial reconnaissance of larger study regions was beginning to identify numerous geometrical patterns across regional landscapes. For example, an aerial survey across England in 1996 revealed the distinct discolouration of plants and crops in numerous geometrical shapes, later confirmed to be crop marks from subsurface objects. These crop marks had been accentuated by the hot, dry summers across the UK from 1989 to 1996 (Featherstone et al., 1999). Using various image enhancement filters, the crop marks in multiple images revealed several new archaeological sites (Featherstone et al., 1999), with many then confirmed as Iron Age through to Roman settlements over excessively well drained limestone and ironstone foundations (Fig. 5).

Subsurface detection regimes using photogrammetry require pixel level delineation techniques. Such techniques, combined with a holistic perspective of the study area from air or space, can equip the user with a broader contextual view of the landscape. This is often crucial for the location of subsurface features like tunnels, trenches and archaeological foundations. The linear trends and geometrical patterns generated in the terrain from such subsurface features are not readily seen on the ground but aerial and space photography can reveal subtle patterns through variations in soil colour, relief shadow and the tone of overlying vegetation (Deng et al., 2010).

Fig. 5. Example of using aerial photogrammetry to detect near subsurface anomalies. Red dashed box contains several crop marks at a site in Hougham in Lincolnshire, revealing a settlement which developed from the Iron Age to Roman period. The aerial photo was taken during an aerial archaeology study in 1996, funded by the Royal Commission on the Historical Monuments of England (RCHME). Figure adapted from Featherstone et al. (1999).

Weber and Yool (1999) explore some of these delineation techniques using two different spatial contrast enhancement filters on four scanned historical photographs of Idalion, an ancient archaeological site in the Nicosia District of Cyprus. They compared the performance of median and locally adaptive spatial contrast filters (Table 2) in the detection of new archaeological features. The former operates in a neighbourhood mode which reduces image noise and smooths differently valued pixels within a group of similar valued pixels (Gonzalez and Wintz, 1987). They are also "edge preserving, smoothing" filters (Pratt, 1991), where their noise reduction qualities can produce a more interpretable image. In contrast, the locally adaptive spatial contrast filters increase the resolution of spatial detail by using local neighbourhood statistics to maximise local contrast and stretch the range of pixel brightness values across a region of interest (Fahnestock and Schowengerdt, 1983). In using the locally adaptive spatial contrast filter, Weber and Yool (1999) enhanced the radiometric resolution of the low contrast air photos and managed to detect the foundations of five towers along a 9.6 km long defensive wall of Idalion.

The subsurface detection capabilities of spaceborne photogrammetry soon followed after the successful application of airborne photogrammetry. Kennedy (1998) performed the first inspection of CORONA space photography for a virtual investigation of the Euphrates Valley in Turkey. Ur (2003) went on to examine CORONA space photography to locate archaeological sites and road foundations in northern Syria, successfully detecting the latter. Before long, subsurface prospecting using space photogrammetry migrated to commercial satellite cameras. In 2003, several buried archaeological features in Cilicia, southern Turkey, were identified using digitally processed and spatially enhanced IKONOS-2 panchromatic and colour photography. On the ground, these sites were obscured by overlying vegetation including maquis and garrigue, and by agricultural terraces supporting wheat and orchards. However, crop marks and micro-relief patterns could be identified from the IKONOS-2 space photography which were later verified with archaeological excavation as 150 BC – 650 AD building foundations (Kucukkaya, 2004).

5.2. Using multispectral imaging

Notable changes in land use and land cover can reveal structural alterations in the subsurface. Mi et al. (2019) use a continuous Landsat imagery classification (Table 2) with a random forest classifier to monitor changes in land use/land cover (LULC) across the Nanjiao mining area in Shanxi Province, China between 1987 and 2017. Initially, they use a data smoothing filter and normalised difference vegetation index (NDVI) to detect the temporal and spatial changes in cultivated forest, natural forest, buildings and farmland. They then used LULC classification techniques to reveal significant regions of LULC change from grasslands and buildings to cultivated forest, revealing regional (and spatial) trends in village abandonment from the lived effects of ground subsidence from coal mining. Temporal analyses of the spectral content in multispectral data can reveal subsurface drivers for change in LULC, benefitting regional land plans, ecological restoration strategies and the development of environmentally friendly management policies in sensitive milieus like mining districts.

Inspecting temporal change across consecutive multispectral images is also a useful technique for identifying the presence of new subterranean structures like cross border tunnels (Table 2). Kwan (2019) reviews a series of change detection algorithms, commonly employed across a full suite of multispectral and hyperspectral imaging case studies. Referring to the detection of changes between images collected at two

Table 2
Airborne and spaceborne remote sensing techniques used for *visual identification*.

Investigable Feature	Sensor Type	Remote Sensing Detection Technique	Example References
• Topographic relief patterns from buried subsurface structures • Anomalous tone, height and density of crop marks • Soil marks/ discolouration anomalies • Changes in land use/land cover related to subsurface activity • Spoil heaps and soil tracks from recent excavation of tunnels/mines	Photographic	1 Geometrical measurements of anomalous visual indicators 2 Creation of digital elevation models (DEMs) from stereopairs 3 mage enhancement filters 4 Spatial contrast enhancement filters	1 Sharafi and Khazaei (2013); Lasaponara and Masini (2014) 2 Luo et al. (2019) 3 Featherstone et al. (1999); Bewley (2003); Kucukkaya (2004) 4 Weber and Yool (1999); Deng et al. (2010)
	Multispectral	1 Spectral classification regimes 2 Change detection algorithms 3 Convolutional neural networks (CNNs)	1 Mi et al. (2019) 2 Kwan (2019) 3 Perez et al. (2017); Li et al. (2019)
• New track formation and heavy plant equipment for tunnelling • Disturbed earth from tunnel excavation or object burial (e.g. landmines) • Anthropogenic micro-relief patterns • Crop marks from subsurface abnormalities e.g. archaeological • Human activity at subsurface entry points e.g. cross border tunnels • Anomalous changes in vegetation cover, surface roughness and elevation over suspected subsurface features	Hyperspectral	1 Image resolution enhancement algorithms e.g. single super-resolution and multi-image resolution algorithms 2 Examine soil reflectance spectra for anomalies e.g. anomalous mineral radiance values along typical absorption lines	1 Kwan (2018) 2 Shimoni et al. (2019)
	Airborne LiDAR	1 DEM/DTM/DSM relief visualisation techniques e.g. analytical hillshading, colour gradient elevation, slope analysis, 3D visualisation, contour analysis, local relief models (LRMs), Openness, Sky View Factor (SVF) and Principal Component Analysis (PCA) 2 LiDAR classification studies incl LiDAR intensity, multi-temporal LiDAR and LiDAR full waveform analysis	1 Devereux et al. (2008); Zakšek et al. (2011); Roman et al. (2017); Moyes and Montgomery (2019); Lieskovský et al. (2022) 2 Challis et al. (2008); Lasaponara and Masini (2009); Challis et al. (2011); Stott et al. (2015)
	SAR	1 SAR change detection routines e.g. Coherent Change Detection (CCD), Incoherent	1 Chen et al. (2016); Comer et al. (2017); Tapete and Cigna (2019); Airbus (2022)

Table 2 (*continued*)

Investigable Feature	Sensor Type	Remote Sensing Detection Technique	Example References
		Change Detection (ICD), RGB multi-temporal composites, correlation and ratio analysis between SAR scenes 2 Temporal analysis of backscattering anomalies throughout a plant's phenological cycle	2 Chen et al. (2014)

different points in time, Kwan (2019) highlights the benefits of employing 'Direct Subtraction', 'Principal Component Analysis (PCA)' and 'Band Ratio' comparisons to detect clandestine tunnel activity across contested borders like USA–Mexico.

Li et al. (2019) also investigated the use of change detection, where change detection maps from existing unsupervised change detection methods were used to train a deep Convolutional Neural Network (CNN). Allowing deep learning to succeed without the use of supervised training data can reduce the data burden and computational time. Similarly, Perez et al. (2017) explore the utility of deep learning on multispectral data, where they use WorldView-2 (WV2) multispectral imagery and a CNN model to identify fresh soil trails and spoil heaps from cross border tunnels along the USA-Mexico border (Table 2). WorldView-2 satellite images in the visible to near infrared (VNIR) range were pansharpened to increase the spatial resolution of the eight VNIR bands to 0.31 m. A four-layer CNN was then configured and trained to classify image patches into 14 different classes (e.g., soil, building, road) using both the spatial and spectral information in the multispectral data. Once trained, the neural network could perform in real-time, computing the probability of an image patch belonging to excavated tunnel soil. A novel method for handling the imbalance in training data was also employed, overcoming the challenge of having a limited number of positive excavated tunnel soil data samples versus an unlimited number of negative training samples. Experimental results showed that the CNN successfully detected a high to low probability plot of excavated tunnel soil (Fig. 6), suggesting that the Perez et al. (2017) imbalance learning technique improved the CNN detection performance.

5.3. Using hyperspectral imaging

In support of cross border tunnel (CBT) surveillance operations, the routine use of automated feature recognition algorithms and VHR imagery to detect new tracks, spoil heaps, tunnel boring equipment and heavy plant machinery will mitigate the illegal use of CBTs (Richemond-Barak, 2018). In particular, hyperspectral imagery is well placed to support these automated feature recognition algorithms (Davis, 2019), especially when used in collaboration with image resolution enhancement algorithms (Table 2) like single super-resolution and multi-image fusion techniques (Kwan, 2018). Kwan (2018) also present a band synthesis technique for generating high resolution hyperspectral images from multispectral imagery, showcasing spectral interoperability between different sensor types.

In support of the visual detection of buried objects, Shimoni et al. (2019) consider a slightly different approach, where discrepancies in longwave infrared (LWIR) and the quartz absorption line are used as a proxy for detecting buried landmines (Table 2). In a review on

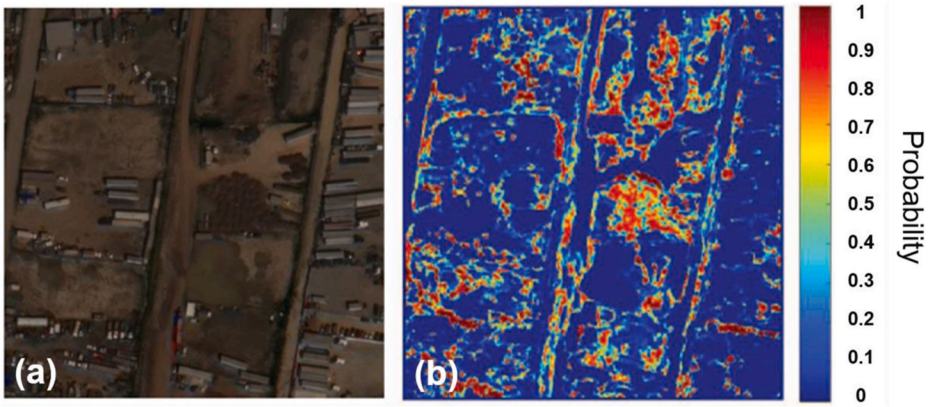

Fig. 6. Soil detection results from the excavation of clandestine tunnels along the USA-Mexico border using a four-layer CNN. a). The WV2 test image in RGB. b). A soil class probability map, where a CNN is trained as a 14-class multispectral soil classifier and then used to map the likelihood of soil deposits originating from excavated cross border tunnels. Figure adapted from Perez et al. (2017).

'Hyperspectral Imaging for Military and Security Applications' they observe physical, chemical and thermal changes in the exposure of bare subsurface soil after landmines were buried across a battlefield (McFee et al., 2005). Changes in reflectance value from quartz particles were observed from the compact soil above a buried landmine and the disturbed soil around it (Shimoni et al., 2019). Further, if a buried landmine lay undetonated for prolonged periods, leakage of the explosive compounds into the environment could contaminate the surrounding soil and vegetation, stressing the physiology of vegetation in ways that can lead to different spectral responses to those affected by natural conditions like drought and salinity (Kalderis et al., 2011).

5.4. Using airborne LiDAR

A LiDAR derived digital elevation model (DEM), digital terrain model (DTM) and digital surface model (DSM) can be inspected for the visual traces of micro-relief proxies from subsurface anomalies (Lasaponara and Masini, 2009). This typically requires the implementation of a suitable relief visualisation technique (Table 2). Within the steep and forested archaeological site of Porolissum in Romania, Roman et al. (2017) identified 79 subsurface sections of a defensive system from the ancient Roman Empire frontiers. Using PCA (Devereux et al., 2008), local relief models (LRMs) (Moyes and Montgomery, 2019), sky-view factor (SVF) (Zakšek et al., 2011) and positive openness (Yokoyama et al., 2002), the surface expression of the ancient remains supported the hypothesis that the site was once extensively deforested by the Romans for strategic purposes. Similarly, in Slovakia, ancient cultural landscape features were detected in the near-surface by identifying micro-relief anomalies in LRMs, SVF, slope gradient and colour blending (Lieskovský et al., 2022). According to Štular et al. (2012), optimal visualisation techniques are dependent on the terrain type and so for effective employment, they should be selected carefully and systematically from an all-encompassing catalogue of thirteen different visualisation methods.

Airborne LiDAR systems can also capture reflectance percentages (i.e., amplitudes) from the returning pulses, more commonly known as LiDAR intensity. The intensity of returning LiDAR pulses vary with the wavelength of the source energy and the composition of the material reflecting the incoming signal. The LiDAR measurements of these reflectance percentage values can be used to produce a georeferenced raster image that both identifies and classifies broad land cover types. During a LiDAR detection study of river valley floors in the Trent Valley of the English Midlands, UK, Challis et al. (2011) examine the various factors which influence LiDAR intensity and explore several processing steps which can be undertaken to enhance the utility of LiDAR intensity analysis. Their results suggest that LiDAR intensity imagery can assist in the interpretation of airborne LiDAR data, where an intensity analysis could be used to augment the qualitative understanding of land cover, the burial environment of archaeological remains and the identification of anthropogenic archaeological crop marks (Table 2). According to Challis et al. (2008) in Bennett et al. (2010), LiDAR intensity data could also become a potential proxy for, or comparable to, conventional geophysical techniques like earth resistivity and Ground Penetrating Radar (GPR), where the relationship between LiDAR intensity and soil moisture values could be exploited.

Notwithstanding Stott et al. (2015) consider a different approach. They experimented with multi-temporal airborne LiDAR and single-date full waveform LiDAR to detect variations in canopy biomass over archaeological features. Although some detection was achieved using metrics of the full waveform data, it was the multi-temporal method using discrete return data which showed the most potential in detecting and characterising archaeological vegetation marks.

5.5. Using SAR

Entrance points to cross border tunnels and urban tunnel networks change with time. Therefore, SAR change detection routines are a useful technique for identifying subsurface entry points, especially in regions where illicit subsurface activity is high. In particular, multi-date SAR products such as interferometric coherence and RGB multi-temporal composites are effective at monitoring this type of change (Chen et al., 2016). According to Tapete and Cigna (2019), one of the best methods to capture the dynamic change of a landscape is to ratio the radar backscatter signal between pairs of SAR scenes from a long time series. In turn, this will depict the spatial extent and distribution of any change. Alternatively, radar backscatter correlations around cross border tunnel sites could be calculated between pairs of SAR images, where correlation images are then generated (Table 2). High coherence values indicate high homogeneity and no change whereas low coherence could indicate the presence of clandestine activity along borders. This technique is more commonly termed 'Coherent Change Detection' (CCD), where both amplitude and phase are considered. However, 'Incoherent Change Detection' (ICD) also shows promise in identifying freshly buried objects (Airbus, 2022), where only changes in amplitude are analysed using high spatial resolution commercial SAR with short revisit times and low (penetrable) microwave frequency. Similar change detection techniques have also been used to locate anomalous change in soil moisture content, vegetation cover, roughness, elevation and geomorphology over archaeological sites and mining regions prone to looting (Comer et al., 2017).

Chen et al. (2014) highlight four surface characteristics from subsurface features that can be observed in SAR imagery. These are

"shadow marks", "crop marks", "soil marks" and "damp marks". Shadow marks are found where very steep slopes generate shadows or when surface roughness contrasts significantly with the flatter surroundings. Crop marks over buried features can be identified when backscattering anomalies appear during a temporal analysis of a plant's phenological cycle and soil and damp marks are found when strong, anomalous back scatter returns are seen from increased groundwater content over a subsurface discrepancy. Fig. 7 depicts the clear distinction of a backscattering anomaly in bare ground, imaged over a subsurface archaeological structure by the COSMO-SkyMed constellation.

6. Detecting soil matrix irregularities

6.1. Using multispectral imaging

High levels of mineralogical leaching and poor and/or excessive drainage conditions in the soil matrix above near subsurface objects (like buried archaeological features) can degrade soil quality and stunt the growth of overlying vegetation (Fig. 3). These irregularities in soil condition are frequently expressed in the health and reflectance characteristics of overlying vegetation and crops (Pascucci et al., 2010). Traditionally, these proxies have been documented in visible light as contrasting areas of grass or crop development, commonly referred to as cropmarks (James et al., 2020). However, a reliance on the visible electromagnetic spectrum has inherent limitations on what can be documented. Therefore, multispectral sensors which measure reflectance values outside visible bandwidths can enhance the detection of near subsurface anomalies under grassland (Bennett et al., 2012) and crops (Moriarty et al., 2019).

James et al. (2020) demonstrated this using two UAV mounted multispectral surveys over an archaeological site in eastern Scotland to produce vegetation index (VI) maps which assess the effectiveness of detecting anomalous crop responses in a temperate climate. The VI maps were analysed visually and statistically, comparing reflectance values on and off the buried archaeological foundations. Consequently, the VIs statistically showed the potential to detect general crop stress from archaeological features across the site (Table 3).

The timing of a multispectral survey is also important. For example, Agapiou et al. (2013a) suggest the optimal time-window for monitoring accentuated barley and wheat crop marks over subsurface anomalies in Cyprus (and the wider Mediterranean region) is the first 15 days of their boot stage, a critical juncture and growing stage in the barley and wheat reproductive phase (Fig. 8). They also use spectral separability indices (SSIs) like 'Euclidean Distance, 'Jeffries-Matusita (J-M) Distance', 'Mahalanobis Distance' and 'Cosine Similarity' to probabilistically assess the spectral separation of reflectance values from vegetation over known subsurface anomalies and those from the surrounding area (Table 3). The results indicate that spectral regions around the red edge and NIR spectrum (700 and 800 nm respectively) are the most effective at distinguishing soil matrix irregularities and crop marks from subsurface features in multispectral imagery.

Temporal observations were also recorded by Dana Negula et al. (2020), who monitored temporal changes in the Normalised Difference Vegetation Index (NDVI), the Simple Ratio (SR) vegetation index and the Normalised Difference Water Index (NDWI) over the Micia and Germisara archaeological sites in Romania using Sentinel-2A multispectral

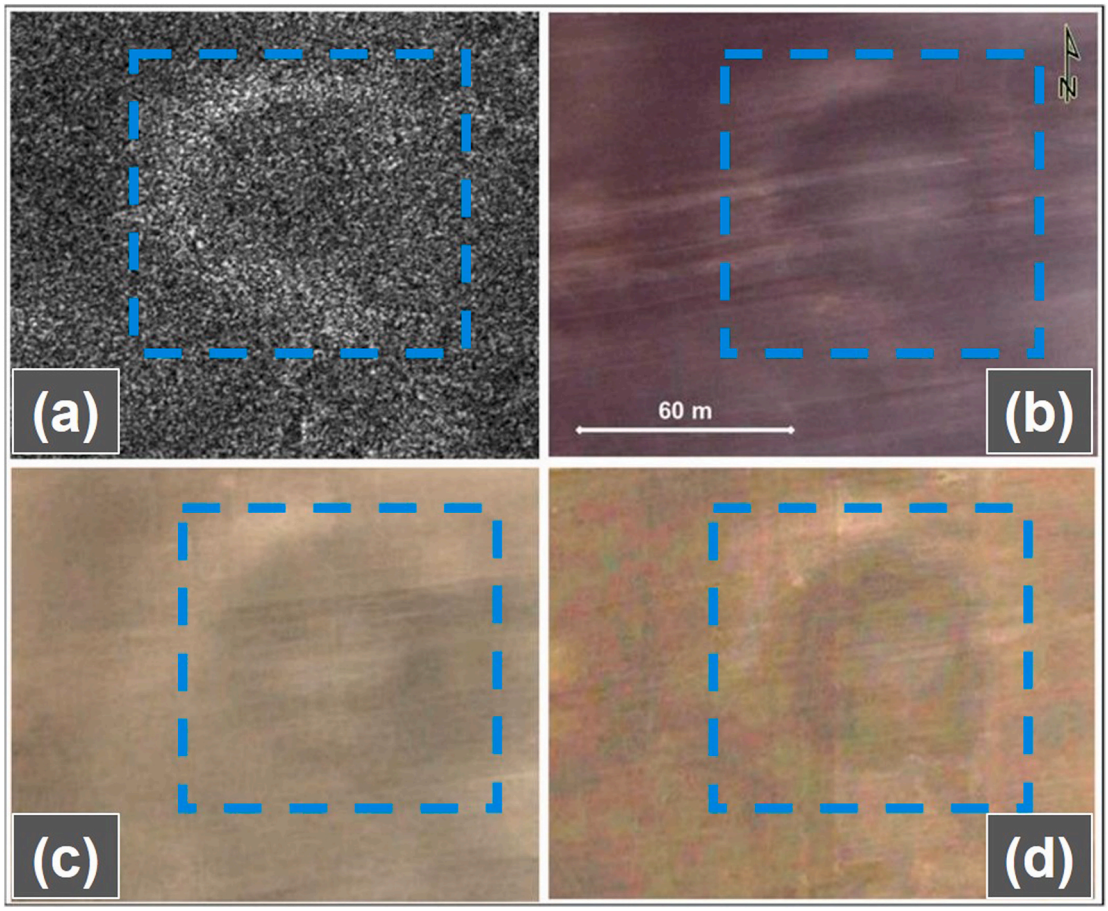

Fig. 7. (a). SAR backscatter anomaly from a partially buried archaeological structure, observed in a COSMO-SkyMed Enhanced Spotlight image at 1 m ground resolution and 39° incidence angle. The soil/damp mark is also visible in Maxar high-resolution optical satellite imagery acquired in (b) summer, (c) autumn and (d) winter. Blue dashed box contains location and circular shape of partially buried archaeological feature. Figure adapted from Tapete and Cigna (2019).

Table 3
Airborne and spaceborne remote sensing techniques used to detect *soil matrix irregularities*.

Investigable Feature	Sensor Type	Remote Sensing Detection Technique	Example References
• Anomalous change in soil condition and vegetation health • Contrasting areas of grass and crop development (crop marks) • Soil marks/ discolouration/ soil salinity • Anomalous concentrations of chemical compounds in soil e.g. Iron Oxide • Stressed vegetation and soil • Soil dielectric discontinuities in paleosols • Subsurface paleo-channels • Buried archaeological features in arid environments	Multispectral	1 Statistically analysing vegetation index (VI) maps 2 Temporal analysis and statistical separability indices (SSIs) of reflectance values from VIs "on" and "off" suspected subsurface features 3 Linear transforms/ orthogonal equations using spectral reflectance values 4 Integrating high-resolution data-sets from several multispectral sensors 5 Image enhancement in spatial domain using image fusion and pansharpening techniques 6 Bespoke spectral enhancement indices (e.g. chemical compounds, soil salinity etc) and edge detection spatial filtering	1 James et al. (2020) 2 Agapiou et al. (2013a); Dana Negula et al. (2020) 3 Agapiou et al. (2013b) 4 Calleja et al. (2018) 5 Lasaponara and Masini (2014); Dao et al. (2017); Perez et al. (2017); Kwan (2018) 6 Allbed & Kumar (2013); El-Behaedi (2021)
	Hyperspectral	1 Use spectral libraries to select optimal hyperspectral narrow bands for the identification of specific soil conditions and ground proxies 2 Examine spectral content for a "blue shift" of the Red Edge Inflection Point (REIP) and/ or 'Distribution Fitting' using Probability Density Functions (PDFs) 3 Examine VIs and statistically assess mutual dependence or correlation between vegetation anomalies and ground truth datasets 4 Calculate and assess Spectral Separability Indices (SSI) between reflectance profiles from pixels "on" and "off" suspected subsurface anomalies 5 Use Spectral Angle Mapper (SAM) or Spectral Mixture Analysis (SMA) to detect the likely presence of a subsurface anomaly	1 Thenkabail et al. (2014) 2 Doneus et al. (2014) 3 Cerra et al. (2018) 4 Bassani et al. (2009); Lasaponara et al. (2016) 5 Cavalli et al. (2009); Savage et al. (2012)
	SAR	1 Polarimetric data analysis using backscatter information from penetrable SAR bands 2 Accentuate backscatter anomalies from penetrable SAR bands by employing image stacking (image summation) techniques, noise reduction filters and a Grey Level Co-occurrence Matrix (GLCM) analysis 3 SAR image enhancement using multi-looking, multi-temporal aver-aging and specialist noise filtration algo-rithms e.g. nonlocal-SAR noise reduction	1 Grandjean et al. (2001); Patruno et al. (2013) 2 Wiig et al. (2018); Tapete and Cigna (2019) 3 Chen et al. (2016)

imagery. Due to stressed crop growth seen using the NDVI and SR, traces of a buried road were found connecting the Cigmău Fort to the baths in Geoagiu–Băi. The NDWI results were also useful, where the near-infrared (NIR) and short-wave infrared (SWIR) wavelengths were used to detect the north-east wall of the Micia Roman Fort. This latter index showcases the effectiveness of NDWI and the sensitivities of moisture content in plants and soil across a subsurface feature.

Agapiou et al. (2013b) take a slightly different approach, introducing linear orthogonal equations for several multispectral satellite sensors. Using PCA to create the initial eigenspace, eigenvalues were used to define the initial feature space before rotating into a new 3D orthogonal space. These linear transformations were able to re-project the initial VNIR bands of a satellite image to a new 3D coordinate system where the first component became the "crop mark", the second component "vegetation" and the third component "soil". In all trials conducted by Agapiou et al. (2013b), the proposed equations were able to enhance the detection of soil matrix discrepancies and their respective crop marks (Table 3).

Stepping away from spectral transformations, Calleja et al. (2018) consider a multi-acquisition approach for detecting anomalous change in soil matrix. Here, they combine the use of multispectral imagery from WV2 with RGB and NIR cameras on a UAV to detect buried archaeological remains across Llanera, an ancient Roman population centre on

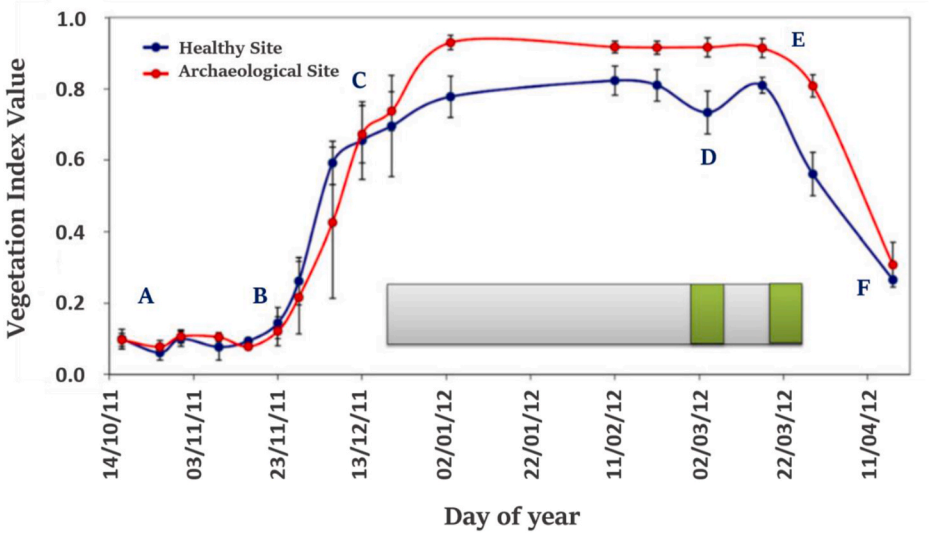

Fig. 8. Temporal variation in vegetation index values (Normalised Difference Vegetation Index - NVDI) at Alampra in Cyprus reveal the phenological cycle of barley crops. The optimal period for remotely detecting crop marks over buried archaeological features is indicated by the grey bar. This is where the separability of the phenological cycles over buried archaeological objects (red line) and regular, healthy soil and crops (blue line) are at their greatest. The best phenophase for detecting accentuated spectral responses from crop marks over subsurface anomalies is shown in green. The time between these green markers denotes the boot stage - where crop development is significant during the reproductive phase of barley. Figure adapted from Agapiou et al. (2013a).

the Iberian Peninsula in Spain. Dual mounted with a global navigation satellite system (GNSS), the UAV data was used to generate true colour composites and a high precision DSM which, in conjunction with WV2 NDVI calculations, generated an archaeological binary map. This archaeological binary map subsequently contained pixels of anomalous NDVI value and normalised threshold elevation value which were thought to represent the location of buried archaeological remains. In total, seven crop marks associated with buried Roman structures were identified, reliant on the premise that buried archaeological remains exist at locations that exhibit both crop and microrelief marks with a similar shape. Therefore, integrating high-resolution and very high resolution (VHR) multispectral sensors from air and space can significantly enhance subsurface detection routines.

If needed, high-resolution multispectral imagery can also be pan-sharpened to guarantee even higher spatial fidelity (Table 3). Further, image fusion with temporally rich sensors like those on a Planet Dove satellite could be used to generate several high-resolution multispectral images over short time periods (Dao et al., 2017; Perez et al., 2017).

Alternatively, spectral enhancement indices and edge detection filtering can be used to improve the spatial resolution of an image and the chances of successfully detecting a subsurface discrepancy (Table 3). El-Behaedi (2021) uses multispectral enhancement indices to detect ground matrix irregularities at the ancient Egyptian site of Hermopolis. Using WorldView-3 (WV3) satellite imagery and edge-detection spatial filtering, the study uses the WorldView New Iron Index to identify iron oxide anomalies across the site. According to Nicholson and Shaw (2009), unfired mudbrick was the most common building material in ancient Egypt and often used for the construction of various domestic installations. Sun-dried mudbricks comprise large amounts of clay, of which 5–6% is iron oxide (Fe_2O_3) (Hool and Johnson, 2010). Therefore, detecting the presence of iron oxide using multispectral imagery assisted El-Behaedi (2021) in the identification of seven subterranean structures. Similarly, Allbed and Kumar (2013) review several soil salinity indices which can be used to detect and map soil salinity and the anomalous groundwater behaviour above subsurface features. The indices have, according to Allbed and Kumar (2013), been employed with varying degrees of success although in general, a multispectral approach continues to showcase much promise in detecting halophytic plants, salt properties in soil and other salt-tolerant crops.

6.2. *Using hyperspectral imaging*

From studying the reflectance and emission spectrums over subsurface structures, hyperspectral radiance spectrums can be compared with spectra from the surrounding landscape to identify anomalies in reflectance or emission at particular wavelengths. This has numerous benefits in near subsurface exploration, where spectral returns in hyperspectral data can show anomalies in soil condition (Alexakis et al., 2009). These can be cross-referenced with various spectral libraries (Fig. D4, Appendix D) to determine specific ground conditions, chemical signatures and soil moisture properties (Thenkabail et al., 2014).

Doneus et al. (2014) explore this concept in detail, devising two new subsurface detection algorithms for hyperspectral imagery.

(i) The first algorithm, termed the Red Edge Inflection Point (REIP), identifies the wavelength, radiance value and maximum gradient in the 'Red Edge' transition zone for every pixel in a hyperspectral image. For healthy soil and vegetation, this transition zone is usually found at 700 nm, where a steep slope along the spectral reflectance curve denotes high absorption rates from chlorophyll pigments in the far-Red spectrum and high NIR reflection rates from spongy mesophyll (Doneus et al., 2014). However, when vegetation is stressed over subsurface objects, this 'Red Edge' transition shifts towards the shorter wavelengths, an effect which is more commonly termed a "Blue shift" of the 'Red Edge' (Horler et al., 1983; Gitelson et al., 1996). By identifying the location of the highest gradient in the Red Edge spectral profile for each pixel, the REIP algorithm can generate a three-band image visualising the optimal wavelength, steepest gradient and reflectance value of the REIP for every pixel in a scene (Doneus et al., 2014). In turn, this can delineate the location of stressed soil, stunted vegetation and anomalous subsurface entities (Table 3).

(ii) The second algorithm named 'Distribution Fitting' generates, for each hyperspectral pixel, a frequency histogram of the radiance values along the pixel's spectral signature, prior to fitting the histogram with a predefined Probability Density Function (PDF). In probability theory, various PDFs are used to mathematically describe the specific distribution of a random variable which in this case, are the reflectance values from the hyperspectral image. Once an optimal PDF is assigned across each pixel (e.g., Normal,

Gaussian, Rayleigh, Exponential, Weibull, Beta, Gamma), the algorithm parameterises the PDF and then the resultant parameters form the digital numbers (pixel values) of the newly generated image. Subsequently, the number of image layers equates to the number of parameters of the chosen PDF (Verhoeven et al., 2013). The resulting image can be used to depict clear contrasts between vigorous and stressed soil and in particular, vegetation and soil irregularities from buried objects (Doneus et al., 2014).

Studying VIs with hyperspectral data, Cerra et al. (2018) objectively estimate the suitability of several VIs for subsurface detection using Information Theory. They were able to compute the statistical mutual dependence between the extracted vegetation anomalies and a digital map (Table 3) which indicated the presence of buried archaeological structures from previous ground surveys. Based on the obtained scores over known archaeological features, the various VIs were ranked at each site and the most suitable were selected to assist in the discovery of previously undetected crop marks. Theoretical mutual information measurements using 'Shannon's Probabilistic Point of View' (Cover and Thomas, 1991) were then used to quantitatively estimate the mutual dependence of a given vegetation index and the location of buried archaeological features. Seen using a subset of the VI results from Selinunte in Sicily (Fig. 9), the results show a clear gradation in VI effectiveness.

Another method for determining hyperspectral bandwidths sensitive to soil condition and subsurface irregularity is the application of SSIs (Bassani et al., 2009; Lasaponara et al., 2016). Spectral Angle Mapper (SAM) and Spectral Mixture Analysis (SMA) can also be employed (Cavalli et al., 2009). The SAM determines spectral similarity on the basis of spectral shape, where the angular difference between the spectrum of every "quarantine pixel" and the spectrum of a pixel related to a subsurface feature is examined (Savage et al., 2012). Conversely, the SMA deconvolves an image using a spectral library over known buried objects to reveal a percentage of likelihood of a subsurface anomaly being present for every pixel in an image (Savage et al., 2012).

6.3. Using SAR

The penetration capabilities of microwaves for mapping subsurface heterogeneities in soil, lithology, moisture and sedimentary structure have been explored by several authors like Grandjean et al. (2001). Experimental sites like the mobile Pyla Dunes near Bordeaux in France are ideal for such analysis, where significant deposits of low-loss sandy material frequently form from the erosion of the Pyrénées and the Massif Central. This weathering activity can produce large subsurface targets featuring multiple paleosols at varying depths (Grandjean et al., 2001).

By conducting a polarimetric analysis of airborne SAR data in the L-band, Grandjean et al. (2001) detect subsurface scattering effects from soil dielectric discontinuities at several places across the Pyla Dune. A series of surface roughness profiles were generated across the sand dunes which were then augmented using ground penetrating radar (GPR). The subsurface structures revealed by the GPR were seen to align with those detected by subsurface scattering from the polarimetric data analysis, allowing them to characterise the geometric and dielectric properties of the subsurface soil structure. The observed GPR profiles were then matched with simulated GPR profiles to produce a subsurface dielectric model adequate for inserting into their SAR scattering model.

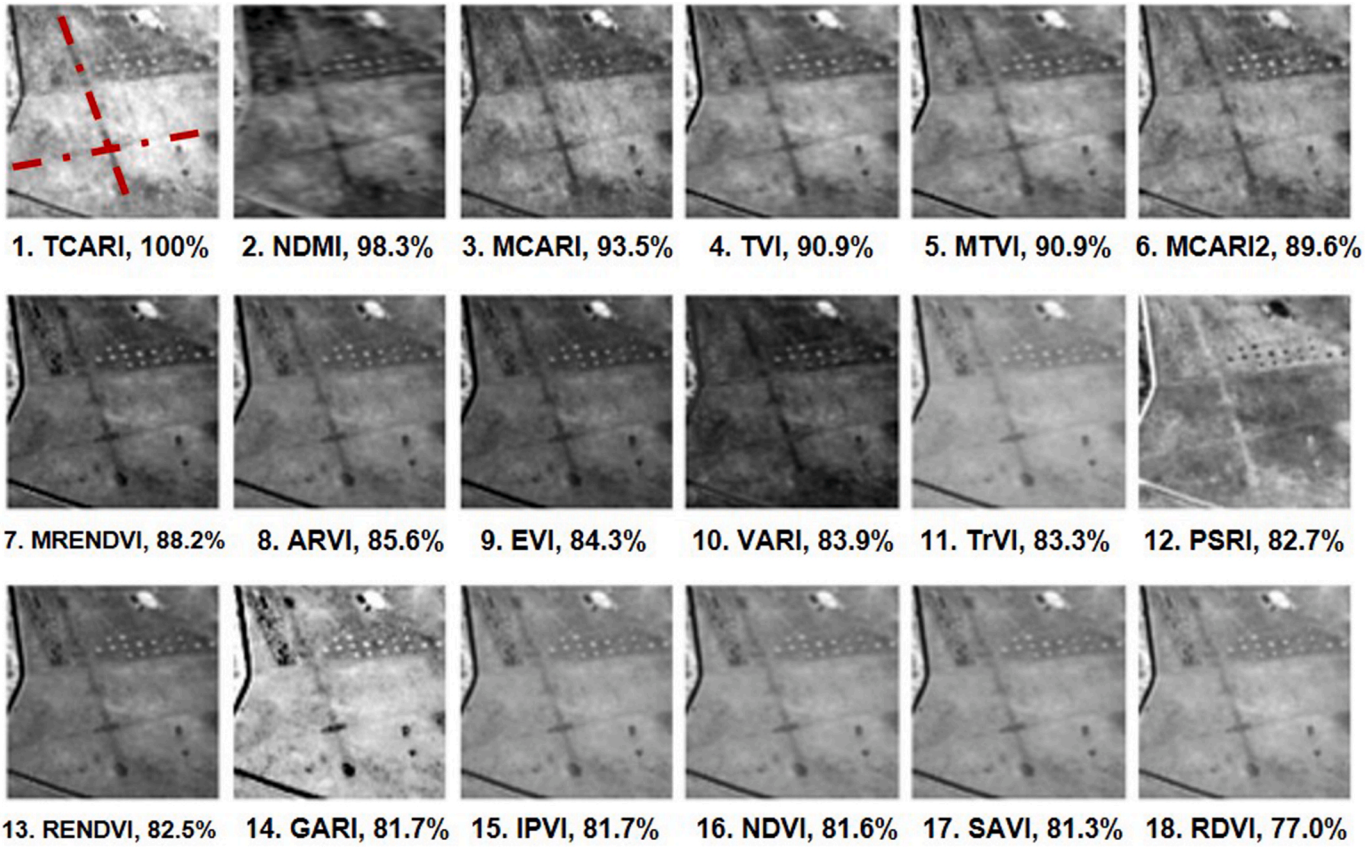

Fig. 9. Eighteen vegetation (spectral) indices ranked from most effective (1) to least effective (18) using Information theory and hyperspectral data over an area of an ancient buried crossroad at the Selinunte cultural heritage site in Sicily. An ancient crossroad (denoted by red dashed line in the TCARI image) is visible under the fields, detected when the mutual information value from the vegetation index scores highly and gradually becoming less evident as the mutual information value decreases. Figure adapted from Cerra et al. (2018).

Consequently, SAR penetration depths were estimated by inverting the SAR scattering model, proving the effective subsurface penetration of L-band SAR. In parallel, the study also revealed the ground moisture detection potential of lower frequencies like P-band, which is capable of detecting subsurface moisture discontinuities up to 10 m deep.

Spaceborne SAR has also been used for imaging ground matrix irregularities in arid regions, where archaeological prospecting is frequently undertaken using L-band SAR sensors (Chen et al., 2017). However, Wiig et al. (2018) demonstrate that shorter-wavelength SAR can also penetrate the subsurface. Using the C-band and X-band information from VV polarization TerraSAR-X bistatic and RADARSAT-2 images at low incidence angles (30–40°), they identify a subsurface paleo-channel 0.6 m–0.7 m deep at the Iron Age archaeological site of Uqdat al-Bakrah (Safah) in Oman. To visually enhance the subsurface anomaly, they sum the images to increase the signal-to-noise ratio, apply a low pass 3 x 3 pixel window filter and a Grey Level Co-occurrence Matrix (GLCM) texture analysis to reduce the speckle and accentuate the location of the subsurface paleo-channel (Table 3). To improve the resolution of the study, Wiig et al. (2018) also recommend a follow-up investigation using even higher spatial resolution C-band and X-band SAR data (from a staring spotlight acquisition mode) and several multi-polarized products.

According to Luo et al. (2019), numerous studies have used the frequency, polarization, incidence angle and scale of SAR to detect soil matrix irregularities and subsurface discrepancies. Both Patruno et al. (2013) and Chen et al. (2016) in Luo et al. (2019) trial different SAR bands, incidence angles and imaging modes for the polarimetric analysis and detection of buried archaeological features in arid environments. To reduce speckle and improve the visibility of these features, SAR image enhancement methods were then used, comprising multi-looking, multi-temporal averaging and image filtration (Table 3).

7. Detecting anomalous groundwater behaviour

7.1. Using photogrammetry and multispectral imaging

Several early attempts to detect geomorphic surface anomalies for natural resource exploration (e.g., Mahajan et al., 1984; Mitra and Agarwal, 1991; Berger, 1994) were conducted using multispectral imaging. Waters et al. (1990) used various photographic and multispectral imagery enhancement techniques to identify unique groundwater patterns, tones and textures that locate subsurface structures like faults, joints, ductile shears, folds, dyke intrusions and veins. An assured location of these geological subsurface structures can, in turn, increase the likelihood of performing a successful groundwater exploration survey. Waters et al. (1990) also describe early applications of multispectral imaging to locate shallow aquifers where, in arid and semi-arid regions, multispectral classification methods identified areas of anomalous vegetation vigour which subsequently represented the presence of near-surface aquifers and buried river channels. However, due consideration to the season of image acquisition should be considered, where the low sun elevation in winter imagery is particularly useful in emphasising ground structure, geomorphology and areas of sustained near-surface moisture.

More recently, Saha (2022) reviewed some applications of airborne multispectral imaging in hydrocarbon exploration. When combined with geophysical and geochemical surveys, the multispectral study successfully identified several anomalous geomorphic features and groundwater regimes related to subsurface reservoirs. The study used spatial filtering techniques, spectral band ratios and PCA to identify anomalous drainage patterns and surface lineament characteristics that delineated the surface expressions of hydrocarbon tied structural traps (faults, fractures and domes) and multiple fracture zones (Table 4).

Table 4
Airborne and spaceborne remote sensing techniques used to detect *anomalous groundwater behaviour*.

Investigable Feature	Sensor Type	Remote Sensing Detection Technique	Example References
• Underground drainage • Subsurface moisture system • Geomorphic surface anomalies (e.g. sinkholes, shake holes) • Anomalous drainage patterns • Buried stream channel (wet fill) • Underground drainage systems	Photographic	1 Image enhancement filters to identify unique groundwater shapes, patterns, tones and textures	1 Waters et al. (1990)
	Multispectral	1 Imagery enhancement using spatial filtering techniques 2 Multispectral classification, spectral band ratios and PCA	1 Waters et al. (1990); Berger (1994) 2 Saha (2022)
• Soil moisture anomalies • Karst sinkholes • Anomalous soil and damp marks over near-surface objects	Thermal Infrared	1 Time of image planned to maximise emissivity contrast between subsurface water/ moisture target and surrounding area	1 Abdel-Hardy (1970)
• Soil dielectric discontinuities and subsurface moisture variations in paleosols	Hyperspectral	1 Inspect spectral behaviour of SWIR bands between 1300 and 1670 nm for radiance anomalies	1 Finn et al. (2011)
• Ancient subsurface hydrological systems e.g. moats • Groundwater withdrawal; significant changes to groundwater level	Airborne LiDAR	1 Contour analysis 2 DEM sink-filling 3 umerical water flow simulation across DEM 4 LiDAR relief visualisation techniques	1 Hofierka et al. (2018)
	SAR	1 The identification of strong, anomalous backscatter returns from increased ground water content 2 Polarimetric data analysis using backscatter information from penetrable SAR bands 3 Building and analysing groundwater models using SAR derived DEMs and specialist GIS analysis tools 4 Time series Interferometric Synthetic Aperture Radar (InSAR) techniques	1 Chen et al. (2014) 2 Patruno et al. (2013) 3 Bubenzer and Bolten (2008); Luo et al. (2017) 4 Ghorbani et al. (2022)

7.2. Using thermal infrared

Abdel-Hardy (1970) illustrated several early applications of anomalous groundwater detection using airborne TIR imaging. One component of the study used an 8–14 μm TIR image of a buried wet stream channel under a field in the campus of the University of California Davis.

The TIR image depicted the outline of a buried stream channel which was bright and light in tone (high emissivity), contrasting with the darker tone (low emissivity) of the surrounding area. This revealed the higher specific heat capacity of the wetter soil in the buried stream channel, explaining why the channel remained warmer at night in comparison to the surrounding soil (which was drier and cooling at greater rates). Abdel-Hardy (1970) also presented similar thermal applications in the detection of underground water conduits for civilian and military reconnaissance. Here, a TIR image was recorded in the early evening using the 8–14 μm TIR range, revealing a buried water conduit under an interstate highway near Dallas in Texas, US. When inspecting the imagery, the conduit under the paved highway generated a surface temperature along the overlying ground that was different to the adjacent paved sections of the highway, visualised as a linear anomaly in surface emissivity (Table 4).

7.3. Using hyperspectral imaging

In 2011, hyperspectral sensors with high spatial resolution and narrow spectral bands were used to quantify soil moisture levels across the Little River Experimental Watershed in Georgia (Finn et al., 2011). Spectral observations from airborne hyperspectral data containing SWIR information were statistically correlated with soil moisture probe data at 5.08 cm, 20.32 cm and 30.48 cm in depth. Results showed that the SWIR bands could determine values and variations in soil moisture at depths to 5.08 cm but less likely at greater depths. In particular, SWIR wavelengths in the 1300 nm–1670 nm range were particularly sensitive to soil moisture levels (Table 4), achieving 'coefficient of determination' values (R^2 values) above 0.70 (Finn et al., 2011). Keller et al. (2018) then developed this further, using hydrological, geophysical and hyperspectral data in a supervised machine learning approach to estimate, with some success, the subsurface soil moisture across a grassland site in Linkenheim-Hochstetten, Germany (Keller et al., 2018).

7.4. Using airborne LiDAR

Given the breadth of visual and textural analysis tools available to LiDAR, Hofierka et al. (2018) adopt a combined visual and textural approach to locate and map karst sinkholes in the Slovak National Park in Slovakia. They considered four very different approaches: contour mapping, DEM sink-filling, numerical water flow simulation and a manual inspection of hillshaded DEMs (Fig. 10). Each method identified varying numbers of sinkholes with varying spatial extents. These detections were then verified with a supporting field investigation. Such ground reconnaissance is often crucial, especially when detecting generically shaped surface depressions across large study regions.

7.5. Using SAR

The identification of strong, anomalous backscatter returns from increased ground water content in SAR imagery can reveal the location of soil and damp marks over near-surface objects (Chen et al., 2014).

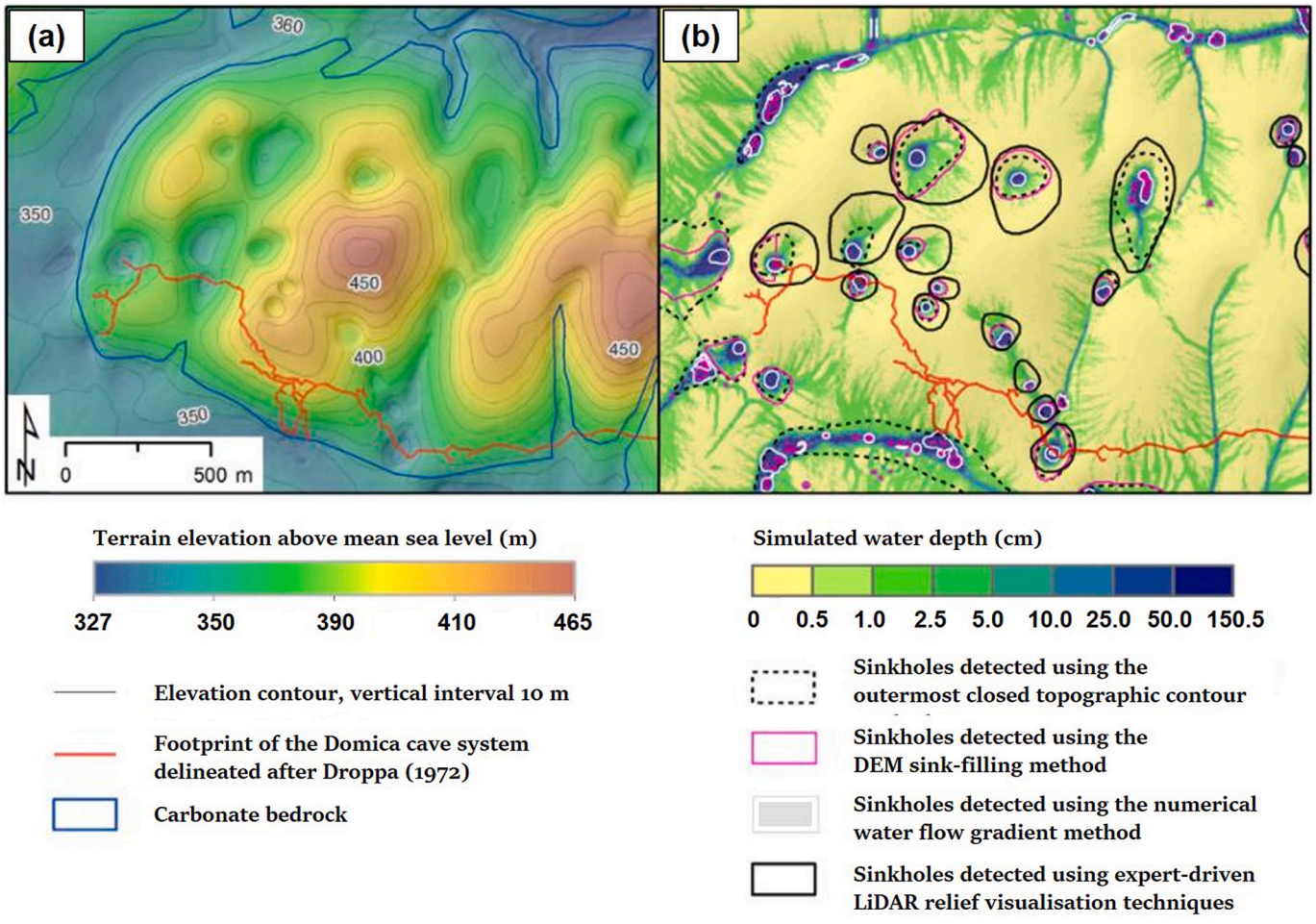

Fig. 10. Detecting sinkholes in a forested karst landscape in Slovak National Park using airborne LiDAR. (a). Hillshaded DEM of the study area showing contours at 10 m intervals, the footprint of the Domica cave system and the spatial extent of the carbonate bedrock. (b). Sinkholes detected in LiDAR derived DEM using four different methods: contour mapping (dashed polygons), DEM sink-filling (pink polygons), water flow simulation (polygons with white outline and light grey fill) and a manual inspection of hillshaded DEMs (black polygons). Figure adapted from Hofierka et al. (2018).

Also, polarimetric data analysis using backscatter information from penetrable SAR bands can detect anomalous subsurface moisture variations in and above subsurface anomalies (Grandjean et al., 2001; Patruno et al., 2013). A hydrological analysis using SAR-derived DEM products (Bubenzer and Bolten, 2008) could also be considered (Table 4). As an example, Luo et al. (2017) used a DEM derived from the Shuttle Radar Topography Mission (SRTM) to generate a groundwater model. They then use a series of GIS hydrological analysis tools to reveal an ancient moat system under the Panlongcheng archaeological site in China.

In contrast, Ghorbani et al. (2022) adopt a very different approach. They use an Interferometric Synthetic Aperture Radar (InSAR) technique to detect regional-scale land subsidence across the Ardabil Plain in Iran. This revealed significant groundwater withdrawal from reduced rainfall and active pumping. Similar InSAR techniques are also reviewed in Section 8.3.

8. Detecting surface elevation change

8.1. Using photogrammetry

Air and space photogrammetry allow an object's height to be determined using relief displacement from both a single vertical photograph and in the overlapping section of a stereopair. Topographic maps and DEMs can be generated from the same principle, producing useful products that can assist with the identification of subsurface features, especially when investigating localised changes in surface elevation and ground subsidence. Various DEM visualisation techniques can then be used to accentuate surface elevation change over subsurface features (Table 5). Such techniques include hillshade analysis, colour gradient elevation, slope analysis and shadow pattern analysis (Luo et al., 2019).

8.2. Using airborne LiDAR

Recent airborne LiDAR applications recognise the importance of filtering and classification of ground and non-ground data points, especially when detecting surface elevation change from subsurface features. In archaeological prospecting, small surface elevation discrepancies can reveal the presence of significant underground entities and it is therefore crucial to filter and classify the raw data correctly before generating accurate DTMs for subsurface interpretation. According to Meng et al. (2010), filtering methods can be grouped into six operating categories: segmentation-based, morphological-based, directional scanning, contour-based, triangulated irregular network (TIN)--based and interpolation-based. If specific characteristics of the study area are unknown, experimenting with all filtering modes is pragmatic, as is the experimentation with various interpolation methods used to create the DEM, DTM or DSM for analysis (Table 5). The most well practiced interpolation techniques for shallow subsurface detection include inverse distance weighting (IDW), kriging, minimum curvature, the modified Shepard's Method, natural and nearest neighbour, polynomial regression, radial basis function, triangulation with linear interpolation, moving average and local polynomial (Luo et al., 2019 and references therein). Again, the most suitable technique depends on specific research objectives and the physical characteristics of the study area.

If data availability allows, LiDAR derived DEMs can also be used temporally to detect and quantify changes in the three-dimensional position, shape and volume of objects and surfaces (Lillesand et al., 2015). By acquiring repeat LiDAR datasets over subsurface targets at multiple points in time, fine-scale topographic changes in land subsidence can be recorded (Table 5). Often termed 'DEMs of difference (DoD)', such techniques can be used to detect ground subsidence over near-surface tunnels, mining districts, sinkholes and shake holes (James et al., 2012). In the Bieszczady Mountains in Poland, many soil

Table 5
Airborne and spaceborne remote sensing techniques used to detect *surface elevation change*.

Investigable Feature	Sensor Type	Remote Sensing Detection Technique	Example References
• Buried archaeological feature/ infrastructure • Subsidence over sinkholes, shake holes and near subsurface tunnels and caves • Buried archaeological features • Buried ditches, pits and water channels • Vertical depressions e.g. sinkholes and sumps over near-surface tunnels • Horizontal and vertical cave entrances • River valley floors • Surface roughness from partially buried objects (e.g. archaeological) • Land subsidence in karstic environments, urban zones, mining districts and tunnel sites • Cave geometries with skylights in lava tubes and karstic sinkholes • Deformation typology of underground aquifers •Elevation change from groundwater extraction regimes	Photographic	1 DEM creation from stereopairs and DEM visualisation techniques (e.g. hillshade, colour gradient elevation, slope analysis etc)	1 Luo et al. (2019)
	Airborne LiDAR	1 Ground filtering of LiDAR point cloud data to determine returns from ground and non-ground surfaces 2 DEM, DTM and DSM generation using different interpolation algorithms 3 DEM subtraction (DEMs of difference) using multiple LiDAR derived DEMs from different acquisition dates or via "sink-filling" DEM prior to subtraction 4 Surface elevation detection techniques e.g. Topographic Position Index (TPI), Topographic Ruggedness Index (TRI), positive and negative openness indices (POI/NOI) and DEM convolution with small elevation templates of surface expression from subsurface target	1 Meng et al. (2010) 2 Luo et al. (2019) 3 James et al. (2012); Bernett-Jakiel and Jakiel (2021) 4 Weishampel et al. (2011); Trier and Pilø (2012); Bernett-Jakiel and Jakiel (2021)
	SAR	1 Generating radar backscattering models with variable radiometric conditions 2 Differential InSAR (DInSAR) and Advanced DInSAR (A-DInSAR) 3 Deep learning CNNs and DInSAR data for automated ground motion	1 Carrer et al. (2015) 2 Barla et al. (2016); Alberti et al. (2017); Bonì et al. (2017); Da Lio and Tosi (2018); Ammirati et al. (2020); Scoular et al. (2020); Aljammaz et al. (2021); Macchiarulo et al. (2021); Ramirez et al. (2022)

(*continued on next page*)

Table 5 (*continued*)

Investigable Feature	Sensor Type	Remote Sensing Detection Technique	Example References
		analysis and automated indicators and warnings for land subsidence	3 Anantrasirichai et al. (2021)

piping-related depressions were detected using these DEM subtraction techniques. Initially, a LiDAR derived DEM was "sink-filled" and then it was subtracted from the raw DEM (Bernatek-Jakiel and Jakiel, 2021) to reveal a series of prospective piping-related ground depressions (Table 5).

In karst landscapes, Weishampel et al. (2011) use LiDAR derived DEMs a little differently, using a 1-m resolution DEM of the ancient Maya site of Caracol in western Belize with a gradient elevation index (Topographic Position Index – TPI) to detect vertical depressions, shafts and cave entrances across 200 km^2 of densely forested landscape (Fig. 11). Weishampel et al. (2011) located 61 depressions with at least 10 m elevation change in circular areas of no more than 25 m radius. Trier and Pilø (2012) pursue similar objectives by convolving a DEM with small elevation templates of the surface expression of a subsurface target. This technique was put to good effect when they generated a series of hemispherical elevation templates of iron age pit structures which were convolved with a DEM to reveal the likely location of ancient pit structures across Oppland County, Norway. This process was acknowledged by the Norwegian Directorate for Cultural Heritage as a cost-effective method for detecting, monitoring and protecting cultural heritage sites from mining, agricultural production, urbanisation and national energy programmes.

8.3. *Using SAR*

The backscattering characteristics from air and spaceborne SAR can identify subsurface entry points across large study regions (Table 5). Carrer et al. (2015) explore this concept using high resolution commercial SAR data from the Capella Space X-band microsatellite radar

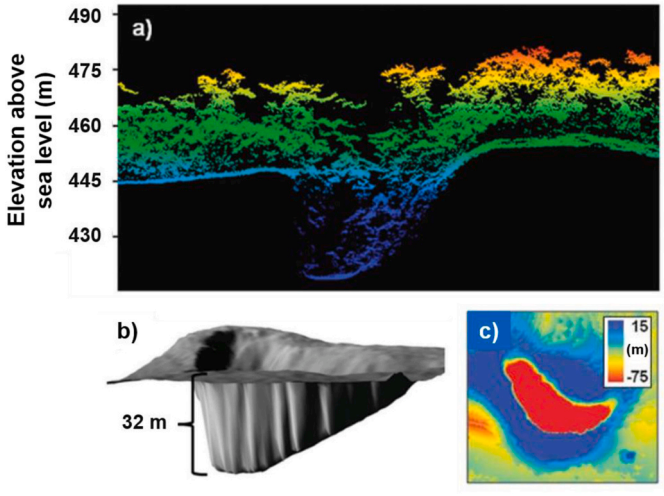

Fig. 11. (a). Airborne LiDAR point-cloud data of the ancient Maya site of Caracol in Belize, depicting the forest canopy and ground surface along a transect across one of 61 vertical depressions (caves, mines and sinkholes) discovered using the Topographic Position Index (TPI). (b). 3D rendering of LiDAR derived DEM around same depression. (c). Aerial view of the TPI image, depicting relative elevation of the same vertical depression in meters. Figure adapted from Weishampel et al. (2011).

constellation to resolve various cave geometries and accessibility characteristics across the Volcan de La Corona Region in Spain, the Volcan Wolf and Volcan Ecuador Region and the Sotano de la Lucha sinkhole in Mexico. The study was configured to detect cave systems with skylights, thereby making full use of SAR's side-looking acquisition geometry to determine whether the skylight can provide access to a cave or if in fact it simply represents a closed depression with no subsurface extension. They use a bespoke radar backscattering model and various radiometric conditions as defined by the reflected signal, backscattering coefficient, local incidence angle and slant range. As a result, quantitative metrics of the subterranean cave size were retrieved for caves accessible by skylights, allowing the authors to assess the feasibility of human or robotic access for geological and ecological research purists.

Phase information in SAR data can also be used to accurately measure changes in surface elevation using a process called SAR Interferometry (InSAR). This process generates a SAR interferogram by computing the phase difference between two SAR images of the same area at different dates and time. This SAR interferogram subsequently reveals changes in phase for each pixel in the image which in turn, depicts an increase or decrease in the distance from the ground pixel to the SAR platform along the acquisition platform's line of sight (Ferretti et al., 2021). A temporal analysis using successive interferograms (often phrased as differential InSAR - DInSAR) is then used to accurately measure the rate of ground subsidence over, for example, sinkholes and tunnels (Scoular et al., 2020) or groundwater extraction sites (Ng et al., 2018).

DInSAR has been used to preserve, manage and protect urban landscapes, mining districts, cultural heritage sites and various tunnels worldwide (Barla et al., 2016; Alberti et al., 2017; Da Lio and Tosi, 2018; Scoular et al., 2020; Aljammaz et al., 2021; Macchiarulo et al., 2021; Ramirez et al., 2022). For example, from knowing that ore bodies in soft rock can trigger unexpected surficial collapse at the surface, Ammirati et al. (2020) employed DInSAR to detect illegitimate gold mining in Ecuador. Using 89 ascending images and 51 descending images from Sentinel 1 data collected between 2015 and 2019, they generated 793 ascending interferograms and 271 descending interferograms which were then used to calculate ground subsidence from illegal artisanal mining in Zaruma, Ecuador.

Advanced DInSAR techniques (A-DInSAR) have also been used to detect subsurface features (Table 5). Bonì et al. (2017) evaluated these techniques over three test sites in Europe, where linear, non-linear and seasonal land subsidence anomalies were identified. Seasonal movements were detected using A-DInSAR in conjunction with a PCA, and new information about the deformation typology of the Alto Guadalentín aquifer in Spain was deduced. Another A-DInSAR approach was undertaken by Anantrasirichai et al. (2021), where deep learning CNNs were used with sparse satellite InSAR data to detect: several areas of coal mining subsidence, uplift due to dewatering, slate quarries, landslides and tunnel engineering works across the UK. A pre-trained CNN was adapted to detect the ground deformation from national scale ground velocity maps from 2015 to 2019. The sparsity of measurement points and the presence of spike noise was overcome using spatial interpolation, enhanced over-wrapping techniques and a synthetic training dataset of a UK velocity map. The results demonstrate much potential in the generation of automated ground motion analysis systems with CNNs.

9. Detecting heat retention anomalies

9.1. *Using thermal infrared*

Given the spatial resolution limitations of spaceborne thermal remote sensing, any heat retention anomaly detected from space must come from a significantly large subsurface feature or widespread underground activity (Sabins, 1997). That said, Van der Meer et al. (2014) undertook a comprehensive review on the TIR detection of geothermal resources. They explored various direct and indirect TIR detection

methods that were sensitive to specific geothermal surface proxies like alteration mineralogy, heat fluxes, geobotanical anomalies and Earth surface deformation. These surface manifestations revealed the approximate location and extent of geothermal reservoirs below ground, where meteoric water in the various permeable and porous rock formations is trapped.

Using a case study from the La Pacana caldera geothermal field in the Chilean Andes, Van der Meer et al. (2014) used daytime and night-time Advanced Spaceborne Thermal Emission and Reflection Radiometer (ASTER) imagery to conduct a comprehensive geologic interpretation of the mineralogy and emissivity. Geothermal anomalies were mapped using the night-time ASTER images, where the complexities of differential solar heating were reduced.

As expected, the tops of volcanoes showed low temperature values due to high altitude, and the steep flanks of the volcanoes showed higher temperature values due to residual differential heating from the day. To correct for these effects, Van der Meer et al. (2014) used an empirical topographic temperature correction from Ulusoy et al. (2012) which used terrain elevation, slope and aspect derivatives from SRTM data to develop empirical relationships between the topographic parameters and measured surface temperatures. The result was a relative temperature map (Fig. 12), where the effect of topography was suppressed and the temperature anomalies were made relative to the mean temperature, revealing several thermal anomalies from subsurface geothermal reservoirs near and under the salt flats (salars). In parallel, the daytime ASTER imagery was used to map clay, silica anomalies and other alteration minerals. By using various band ratio techniques to enhance absorption features (including the five TIR bands), and from studying pseudo reflectance curves, different mineral assemblages associated with near-surface thermal systems were identified across the caldera and consequently, the location of suspected geothermal reservoirs below ground were identified (Table 6).

Another common subsurface heat signature is underground coal fire, identified as both a heat source and a combustion site. The heat energy produced is transferred by air convection through cracks and holes in the ground and by conduction through bulk rocks, forming different types of thermal anomaly at the surface. Field observations and temperature measurements show that localized high-temperature thermal anomalies are typically related to holes and cracks (c.1–10 m long and c.1–30 cm wide) while low-temperature thermal anomalies are generated by thermal conduction, often producing regional scale thermal anomalies proportional to the size and depth of the underground fire (Wang et al., 2015).

In China, recent coal fire investigations have been undertaken from space. Du et al. (2022) use the TIR bands in night-time ASTER images of the Huangbaici and Wuhushan mining areas in the Wuda coalfield in Inner Mongolia, China, from 2002, 2003, 2005 and 2007 to understand and monitor the way underground coal fires spread across a region. An adaptive-edge-threshold algorithm was used to detect and perform a time-series analysis on the underground coal fires across the study area (Table 6).

China is also invested in thermal airborne surveys of archaeological sites. In 2002, a project entitled 'Synthetic Archaeological Studies with Remote Sensing and Geophysics Survey' on the Mausoleum of the Emperor Qinshihuang (MEQ) (259–210 BC) was incorporated into the National High Technology Research and Development Program of China (Tan et al., 2006). The project employed thermal remote sensing techniques and geophysical survey to map the distribution of various historic

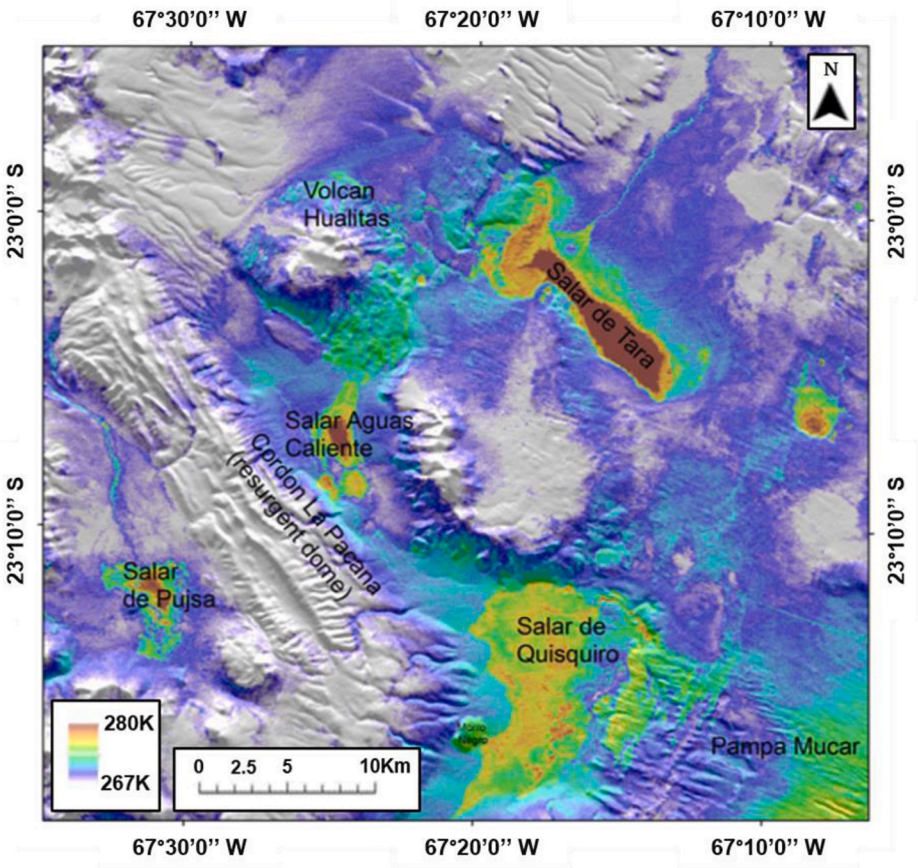

Fig. 12. Temperature anomaly map of the La Pacana caldera geothermal field, Chile. The empirical topographic temperature correction from Ulusoy et al. (2012) was used on ASTER night-time imagery to reveal the location of several thermal anomalies from subsurface geothermal reservoirs near and under the salt flats (salars). Figure adapted from Van der Meer et al. (2014).

Table 6
Airborne and spaceborne remote sensing techniques used to detect *heat retention anomalies*.

Investigable Feature	Sensor Type	Remote Sensing Detection Technique	Example References
• Geothermal reservoirs • Thermal plumes • Underground coal fires • Buried ditches and water channels • Caves • Buried archaeological features • Tunnels/conduits • Underground military facilities/ civilian infrastructure • Cave and mine entrances	Thermal Infrared	1 Collect thermal imagery when thermal inertia contrasts are high 2 Enhancement using TIR band ratios/edge enhancement filters 3 PCA on multi-band thermal images 4 Thermal image subtraction between different images in time 5 Oblique time-lapse recording 6 Empirical topographic temperature corrections 7 Slow and stable UAV collection platforms 8 Mission-planning software to program autonomous flights 9 Terrain analysis, terrain descriptors and pixel cluster analysis 10 Numerical simulation of heat transfer from distributed subsurface targets	1 Del Grande (2009); Casana et al. (2017) 2 Van der Meer et al., 2014; Du et al. (2022) 3 Hill et al. (2020) 4 Grande et al. (2013); Casana et al. (2017) 5 Hill et al. (2020) 6 Ulusoy et al. (2012) 7 Hill et al. (2020) 8 Casana et al. (2017) 9 Wynne et al. (2021) 10 Deng et al. (2022)
	Hyperspectral	1 Thermal emissivity contrasts and absorption line analyses in LWIR hyperspectral data cubes 2 Increased water vapour content in air pixels	1 Shen and Roettiger (2012)

artefacts and detect the architecture of an underground palace. In 2003 both daytime and night-time thermal images of the MEQ were acquired using an Operative Modular Imaging Spectrometer (OMISII) on a fixed wing aircraft. Thermal anomalies were identified over a pyramid shaped mound which were confirmed, using magnetics, to delineate the extent of the underground palace (Tan et al., 2006). Furthermore, the "thermal high" from the compacted soil which buried an ancient tomb was easily distinguishable from the surrounding soil matrix because the densely packed soil had a higher heat conductivity than the lightly packed soil in surrounding areas.

Casana et al. (2017) have also undertaken and reviewed several subsurface investigations using airborne TIR. They promote the efficiency of UAVs, using drones and specialist camera configurations for subsurface investigations. Here, the UAVs are flown at fixed altitudes and constant speeds whilst suppressing flight vibrations. They also use specialist software to control UAV speed, camera orientation and flight plans with Global Positioning System (GPS) guided waypoints (Table 6). Casana et al. (2014) trialled UAV thermal imaging over a pre-historic Chaco-period archaeological site named 'Blue J', located in New Mexico, US. They used Agisoft PhotoScan software to produce colour and thermal ortho-imagery via the extraction of numerous still images from video feeds recorded by the camera. The software used feature extraction and matching capabilities with traditional aero-triangulation to create accurate orthorectified thermal imagery and digital surface models from the overlapping two-dimensional imagery. These thermal products identified new archaeological features that were originally undocumented, including wall extensions, room block layouts and buried pit structures (Casana et al., 2014).

More recently, Hill et al. (2020) explored the utility of UAV-optimized radiometric thermal cameras for archaeological investigation, where in combination with VNIR multi-spectral sensors, they detect buried building foundations of several 18th Century Shaker buildings in New Hampshire, US. By flying fifteen UAV surveys over the Enfield Shaker Village on seven different occasions in several different seasons, they could monitor the localised temperature fluctuations across the diurnal and seasonal cycle and optimise their choice of imagery for subsurface detection. Various detection techniques were employed, including the generation and interpretation of a multi-band false colour composite, comprising data values from twelve different thermal surveys and four bands of multi-spectral data. They also derived the first three principle components of the same multi-band image as a false colour composite and performed a temperature difference study (thermal image subtraction) between thermal images recorded at different times of the day and/or the year (Table 6). A study over a suspected 18th Century building foundation under flat grassland using 'oblique time-lapse recording' of high-resolution thermal imagery delineated the building foundations in various tonal visualizations, and demonstrated the fluctuations in temperature contrast and thermal inertia throughout the night (Fig. 13).

Other subsurface structures susceptible to TIR imaging are caves and in particular, cave entrances. Cave entrances appear as warm features in night-time thermal imagery and cool features in daytime thermal imagery, explained by the stabilisation of deep interior cave temperatures (Thompson and Marvin, 2005; Wynne et al., 2008). Consequently, Wynne et al. (2021) explored thermal predawn, midday and image differenced airborne imagery for detecting caves and ascertained which image type was most effective. Using a thermal imagery dataset of the Pisgah Lava Field in the eastern Mojave Desert, California, US, they also examined the effectiveness of slope, TPI and curvature to detect lava tube caves across the study area using pixel level assessments. Pixels were grouped into spatial clusters to examine pixel aggregations of known caves and non-cave landscapes. Their cluster analysis showed predawn and difference imagery to be more effective than midday imagery and that cluster analysis is a necessary step to predict and identify cave locations in thermal imagery (Table 6).

Finally, numerical simulations have now been used to understand how TIR remote sensing can detect underground facilities like military installations in mountainous terrain (Deng et al., 2022). By assuming the heat transfer law of a distributed underground target in a mountain follows the mathematical model of heat conduction, the temperature field distribution of the Yujiashan mountain and its various underground targets was determined in China (Deng et al., 2022; Shi et al., 2022). Deng et al. (2022) showed that the thermal field from the superposition of the mountain and subsurface target can be mathematically expressed and that ultimately, the position of underground targets can be located using multi-temporal TIR images of the mountain, a high precision DSM and some grid level modelling of the direct solar radiation, scattered radiation and radiation from surface vegetation (Table 6).

9.2. *Using hyperspectral imaging*

In support of defence and security research, hyperspectral data has been used to detect the thermal signatures from several abandoned mine and cave entrances across the Skidoo Mining District in Death Valley National Park in California, US (Shen and Roettiger, 2012). Here, the thermal contrast between the mine or cave entrance and the ambient environment was regarded a discriminatory signature (Wynne et al.,

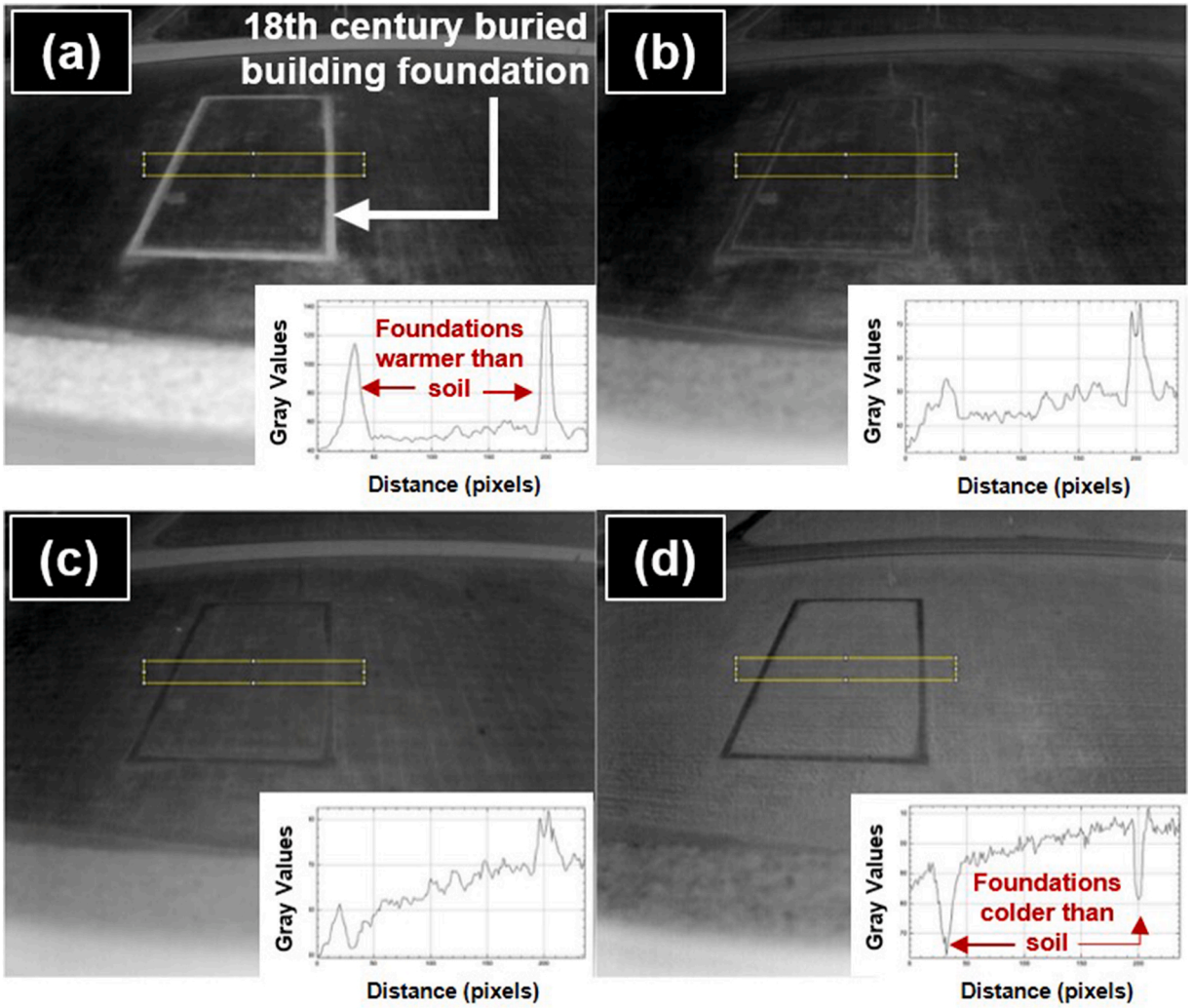

Fig. 13. Four airborne thermal images of an 18th Century buried building foundation in the Enfield Shaker Village in New Hampshire, US. All four images (a–d) were taken using thermal oblique time-lapse recordings from different times in the night. Inside the yellow box, a temperature profile has been recorded across the buried building foundation, with results shown in the respective line graphs. a). Image taken just after sunset when foundation stones are warmer than surrounding soil matrix; b). A few hours after sunset when foundation stones have cooled; c). Dew appears in early morning and thermal contrast is further reduced; d). Taken after dawn when foundation stones are colder than surrounding soil matrix. Figure adapted from Hill et al. (2020).

2008), in conjunction with a water vapour absorption line at 12.55 μm wavelength and a quartz absorption feature at 9.25 μm (Table 6). Using LWIR hyperspectral data from a Twin Otter aircraft, a temperature and emissivity separation algorithm was applied to the LWIR data to generate a temperature map and an emissivity data cube of the scene. Secondly, by knowing that cave and mine entrances exhibit cooler thermal properties than their surroundings during the day (Thompson and Marvin, 2005), the thermal contrasts derived from the temperature map were used to delineate several prospective cave and mine entrances across the study area. Thirdly, to increase confidence ratings, the emissivity of two absorption lines were used to reduce the number of false alarms in the dataset. The first absorption line was 9.25 μm where quartz, an abundant mineral in many mining areas, typically exhibits strong absorption features. However, soils near mine and cave entrances present an absorption deficit due to the disturbed nature of the ground. The second absorption line was 12.55 μm, where water vapour (i.e. humidity) in the vicinity of caves and mine entrances is higher than the surrounding area, generating greater levels of absorption in this range. Subsequently, Shen and Roettiger (2012) observed new cave and mine entrances outside of their ground truth dataset.

10. Detecting subsurface density anomalies

10.1. Using airborne gravity

Detecting subsurface density contrasts with airborne gravity is routine across academic and commercial applications. More recently, the use of airborne gravity was reviewed across the Jordan Dead Sea Transform (DST) Zone, where several potential field investigations of the Jordan DST were conducted to detect and evaluate the structural framework and lithologies across the region (El-Kelani, 2020). Airborne gravity data was collected to assist terrestrial gravity studies in revealing the geometry of the DST pull-apart basins, the depth of the basement and the dimensions of various magmatic intrusions and volcanic centres. Gravity data was also used to assess the spatial distribution of salt diapirism along the DST zone and the identification of underground salt structures in the Dead Sea basin (Choi et al., 2011). Additionally, gravity data was used to locate karst sinkholes and detect salt formations along the Dead Sea coast (Ezersky et al., 2013).

Most of this data was collected by the Natural Resources Authority (NRA) in Jordan and in total, 100,000 gravity stations were deployed and augmented by airborne gravity (Götze et al., 2010), reinforcing data coverage on both sides of the Dead Sea basin (Götze et al., 2007). To

enhance the various frequency components of the gravity fields, a variety of filtering techniques were employed (Table 7). Firstly, first and second derivatives of the residual Bouguer Anomaly (i.e. difference between observed and corrected gravity measurements and base station readings) were calculated to highlight the fault patterns around the Dead Sea basin and Lake Tabeires (Segev and Rybakov, 2011). Secondly, horizontal gradient analyses of the gravity field were applied to detect the discrete border of causative bodies at depth, revealing information about the deep structure of the Carmel fault zone (Achmon and Ben-Avraham, 1997). Thirdly, an isostatic regional gravity field of the southern transform region was produced, enhanced by the curvature analysis of local features in the isostatic residual gravity field (Götze et al., 2007). Finally, a wavelength filtering technique was used to separate the regional-residual gravity anomalies north of the Dead Sea basin. The residual field revealed a complex pattern of anomalies which were believed to correlate with the various geological structures associated with the origin of the Dead Sea (El-Kelani, 2020).

The importance of correcting observed gravity data before any further analysis and interpretation takes place cannot be overstated. Figure D5 (Appendix D) explains the importance of gravity data reduction (LaFehr and Nabighian, 2012) in detail, where several corrections are applied to observed gravity measurements before subsurface density assessments are performed. Opportunistically, if airborne gravity and LiDAR are collected in tandem, the relevant tiles of LiDAR derived DEMs and DTMs can be used to calculate highly accurate terrain corrections (Table 7). This is particularly useful for low flying gravity surveys over complicated terrain like highway tunnel projects in mountainous terrain and environmental surveys over rugged karst environments (Zahorec et al., 2019).

Jamaludin et al. (2021) use airborne gravity techniques to understand the shallow and deep subsurface structures in Central Luconia Province off the coast of Sarawak, offshore Malaysia. The raw gravity data was acquired using airborne gravimeters mounted on a Basler turbo BT-67 aircraft operated by Bell Geospace Ltd. The survey used an Airborne 'Full Tensor Gradiometry' (Air-FTG) gravity technique which comprised a multiple accelerometer moving platform that measured accelerations in the inline and cross sections from three gravity gradient instruments (GGI). These GGIs were used to calculate the various directional gravity gradients which then generate Tyx, Tyy, Tyz, Txz, and Tzz tensor components (Murphy, 2004). Each of these tensor components represents a gravity gradient in an independent direction and as a result, they can be used to recognise and classify different lineaments associated with structural or stratigraphic changes below ground (Table 7). Subsequently, the different gravity gradient tensor components were analysed using contrasting frequency slicing, representing different scales and target depths across the province (Murphy and Brewster, 2007). This resulted in the detection and classification of several faults and structural lineaments, where each lineament was inferred as a structural and stratigraphic change across the Luconia Province. Further, strike directions of the structural trends using Air-FTG interpretation were measured and plotted as rose diagrams to distinguish the relevant subsurface structural orientations for future hydrocarbon exploration programmes (Jamaludin et al., 2021).

Subsurface exploration using airborne gravity can also assist with the exploration and evaluation of geothermal potentials, much like the geothermal potential in the Siwa Oasis in the Western Desert, Egypt (Abdel Zaher et al., 2018). In this study, a 3D inversion of airborne gravity data from the African Gravity Project was used to delineate the depths to Precambrian basement rocks, while a power spectrum method was used on some mutually supporting aeromagnetic data to estimate the Curie Point Depth and provide geothermal gradients and heat flow maps under the Siwa Oasis. The inverted airborne gravity data was used to generate a 3D density model of the sediment-basement topography which produced a theoretical gravity anomaly that aligned with the measured gravity anomaly. The 3D inversion results showed that the Precambrian basement surface across the study area had intensive irregular topography, with depths ranging from 2 km to 5 km (Abdel Zaher et al., 2018). Here, a polynomial regression was used (Beltrão et al., 1991) to separate regions originating from long wavelength, deep-seated density sources and residual anomalies from shallow-seated density sources (Table 7).

Table 7
Airborne and spaceborne remote sensing techniques used to detect *subsurface density anomalies*.

Investigable Feature	Sensor Type	Remote Sensing Detection Technique	Example References
• Mineral ore deposits • Structural geology/faults • Sediment-Basement depths & topography • Magmatic intrusions • Geothermal potentials • Salt diapirs • Subsurface voids/karst cavities • Lithological contacts • Tectonic/karstic discontinuities	Airborne Gravity	1 First and second derivatives of the residual bouguer anomaly (incl vertical and horizontal gravity gradients) and wavelength filtering 2 Airborne Full Tensor Gradiometry (Air-FTG) 3 Upward and Downward Continuation/ Frequency Slicing 4 3D Gravity Inversion 5 Polynomial Regression	1 Achmon and Ben-Avraham (1997); Segev and Rybakov (2011); El-Kelani (2020) 2 Jamaludin et al. (2021) 3 Murphy and Brewster (2007); Braitenberg et al. (2016) 4 Abdel Zaher et al. (2018) 5 Beltrão et al. (1991)
• Magma chambers and volcanic conduits	Airborne LiDAR	1 LiDAR DEMs/ DTMs used to calculate accurate terrain corrections for gravity surveys	1 Zahorec et al. (2019)
• Chambers inside pyramids	SAR	1 SAR doppler tomography	1 Biondi (2022); Biondi and Malanga (2022)

10.2. Using SAR

Biondi (2022) detects subsurface density change using spaceborne SAR. By acknowledging the presence of several notable density changes inside a volcano, Biondi (2022) employs a SAR echography tomographic doppler imaging technique which uses the micro-acoustic motions present in a volcano and those generated from the Earth's underground heat to process and analyse the coherent vibrational information embedded in a single SAR image. The sound information in the SAR image is used to generate a series of tomographic maps that reveal the presence and location of the magma chamber and major volcanic conduits in Mount Vesuvius (Fig. 14).

Similar techniques (noted in Table 7) are also used by Biondi and Malanga (2022) to reveal the internal structure of the Great Pyramid of Giza. Much like the study of Mount Vesuvius, SAR data from the COSMO-SkyMed Second Generation satellite constellation in the single-look complex (SLC) configuration is used with background seismic waves from the natural environment (e.g., wind, River Nile etc) and the nearby city of Cairo to produce high-resolution 3D tomographic models of the Khnum-Khufu pyramid's interior.

11. Detecting magnetic field variation

11.1. Using aeromagnetics

Aeromagnetic surveys have been used extensively in the search for metalliferous mineral deposits. In 1966, total field aeromagnetic anomalies over the Eyre Peninsula in South Australia delineated the location of a large magnetic iron ore body, where the ratio of magnetite

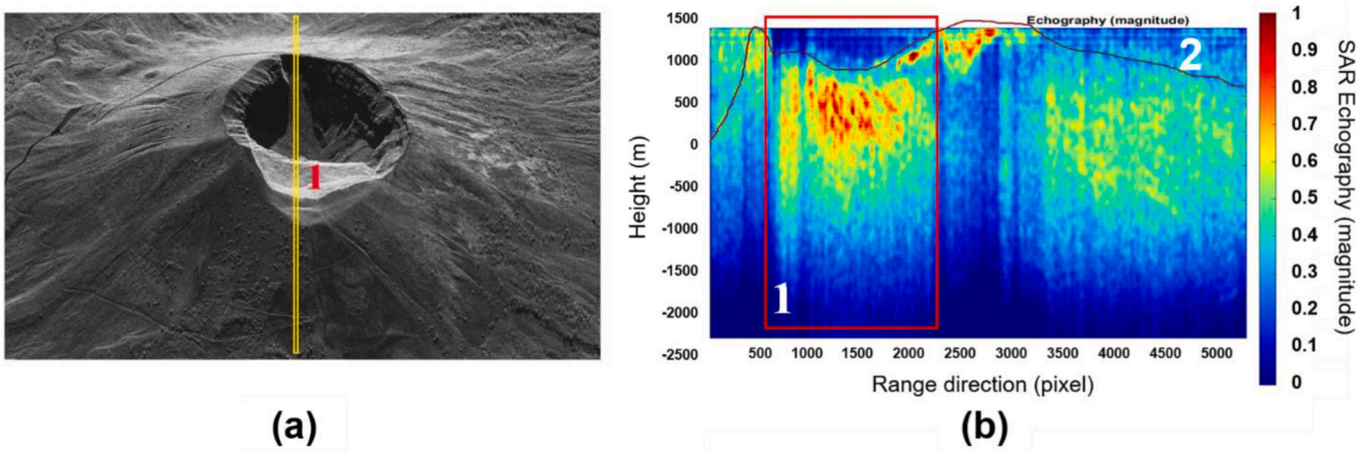

Fig. 14. Range-line SAR echographic tomography profile of Somma Vesuvius. (a). Single-look complex SAR image (magnitude only) with location of tomography profile (yellow line). (b). Tomographic image along tomography profile using magnitude information from SAR data. Area 1 (red box) contains the magma chamber under the crater and Area 2 is the tomography result under the western slope of Mount Vesuvius. Figure adapted from Biondi (2022).

(magnetic) to haematite (typically non-magnetic) was high enough to produce two pronounced anomalies (c.4000 nT) north of Warramboo (Webb, 1966). The geophysical principles used in this survey, and the widely acknowledged benefits of aeromagnetic mineral exploration are still employed today, where airborne surveys are often used in conjunction with ground survey and geochemical data to map ore deposits (Kharbish et al., 2022).

El-Raouf et al. (2023) successfully mapped the subsurface structure and location of several gold-ore mineralization deposits in ophiolitic assemblage rocks around the Wadi El-Saqia region in the Central Eastern Desert of Egypt. The aeromagnetic data was enhanced and interpreted using several edge-detection and edge-enhancement techniques (spatial derivative filtering) including the first-order vertical derivative (FVD), the analytic signal (AS), the total horizontal derivative (THD), the tilt derivative (TD), the tilt angle (TA), the theta filter and the Centre for Exploration Targeting (CET) grid analysis technique (Table 8). By employing each of these methods in turn, the subsurface study located the main structural lineaments and contacts associated with the distribution of hydrothermal alteration zones (Fig. 15), formed when ophiolitic-assemblage rocks contact meta-sediments and other similar rock units. Geochemical analyses were then undertaken using the mineral chemistry of pyroxene and plagioclase to describe the tectonic and magmatic evolution across the region. Subsequently, the airborne magnetic results revealed the prevalence of various structural orientations across the study area, with depths ranging from 50 m to 600 m. El-Raouf et al. (2023) then used geochemical sampling to reveal significant percentages of gold in pyrite, galena, pyrrhotite, and electrum. Therefore, the utility of various derivative filtering techniques with aeromagnetic data can significantly assist with the identification of hydrothermal alteration zones and in this specific case, locations for gold mineralization.

There are numerous examples showcasing the application of horizontal gradient filters on total-field aeromagnetic data, proving it an effective procedure for separating shallow and deep magnetic source anomalies while enhancing the visualisation of particular linear features (Table 8). Doing exactly this, Grauch (2002) enhanced the visualisation of basin-filled sedimentary structures in Nevada, US, where localized regions of high magnetic horizontal gradients revealed the location of several shallow buried faults. By design, this particular aeromagnetic survey was high resolution, guaranteeing the successful assessment of shallow faulting and the near subsurface flow of hot fluids. Of note, most of the faults within the basin were extremely shallow and therefore difficult to detect with alternative subsurface imaging techniques like seismic refraction and seismic reflection (Everett, 2013).

Table 8
Airborne and spaceborne remote sensing techniques used to detect *magnetic field variation*.

Investigable Feature	Sensor Type	Remote Sensing Detection Technique	Example References
• Ore mineralization deposits • Faults and fracture zones • Buried tunnel valleys • Geothermal Potentials • Stratigraphic boundaries • Fault zones • Karst development/ sinkholes • Underground utility pipes	Aeromagnetic	1 Image enhancement filtering/spatial derivatives of total magnetic field anomalies: First-order Vertical Derivative (FVD); Analytic Signal (AS); Total Horizontal Derivative (THD); Tilt Derivative (TD); Tilt Angle (TA); Theta filter; Centre for Exploration Targeting (CET) Grid Analysis 2 Upward continuation and low pass filtering/ Downward continuation and high pass filtering 3 Power Spectrum Method	1 El-Raouf et al. (2023) 2 Everett (2013); Ottesen et al. (2020) 3 Abdel Zaher et al. (2018)
	Airborne Electromagnetic	1 Spatially Constrained Inversion (SCI) 2 Ground-airborne frequency domain electromagnetic method (GAFEM), helicopter-borne time-domain electromagnetic method (HTEM) and semi-airborne transient electromagnetic method (SATEM)	1 Viezzoli et al. (2008) 2 Hartshorn et al. (2022); Sun et al. (2023); Zhang et al. (2023)

A similar approach was used in the North Sea where aeromagnetic data from the Geological Survey of Norway's (NGU) Crustal Onshore/ Offshore Project (COOP) was used with 3D seismic data to map over 2200 buried tunnel valleys (Ottesen et al., 2020). To support this study

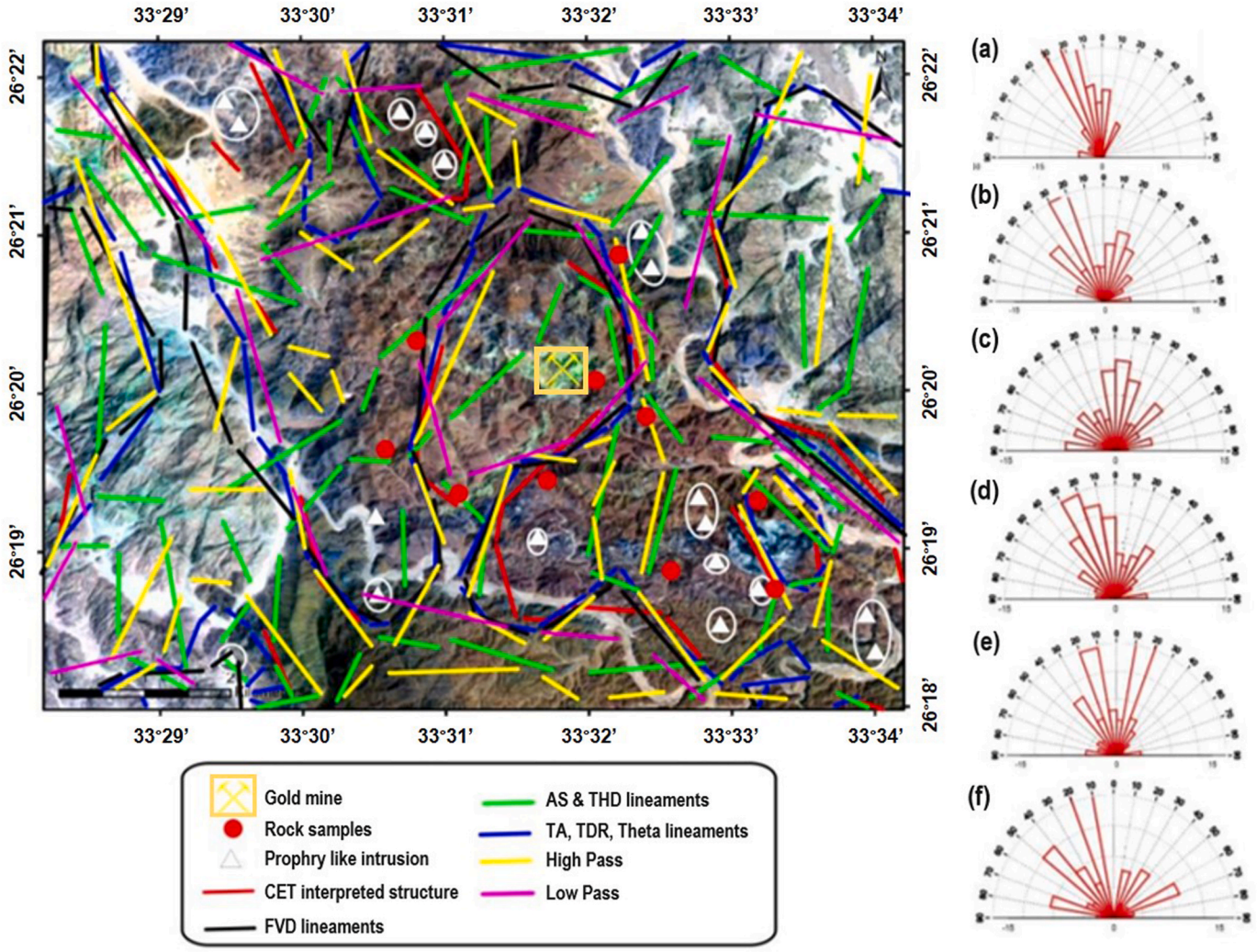

Fig. 15. Image map showing the faults, contacts and dykes associated with gold mineralization beneath the surface of the Wadi El-Saqia study region in the Central Eastern Desert, Egypt. The supporting rose diagrams display the primary and minor trends of subsurface lineaments for: (a) the CET grid analysis; (b) FVD; (c) AS and THD; (d) TA, Theta, and TD; (e) high-pass filter; (f) low-pass filter. The rose diagrams display the primary and minor trends of the subsurface lineaments. Figure adapted from El-Raouf et al. (2023).

and others, 82,000 km of aeromagnetic data was acquired across the Norwegian North Sea (in a regular line-tie-line configuration) by NGU's COOP and merged with existing magnetic data. High-pass filtering was applied to the new magnetic data to extract the magnetic signal from shallow sources and in particular, to highlight the magnetic signatures from the shallow buried tunnel valleys (Table 8). In total, 139 cross-cutting channel systems from the magnetic data were identified, most of which were 0.5–10 km wide, 80–100 km in length and 10s–100s of metres deep. In parallel, the 3D seismic data identified a further 2158 tunnel valleys. This combination of aeromagnetic and seismic analysis was able to reveal information on the past configuration and dynamics of the Scandinavian and British ice sheets and the processes by which sediment and meltwater were transported at the base of the ice-sheet during the Quaternary glacial periods. Albeit only 6 % of buried tunnel valleys were detected using airborne magnetics, Ottesen et al. (2020) prove that aeromagnetic data can provide a clear detection regime for buried tunnel valleys.

11.2. Using airborne electromagnetics

Very much reliant on magnetic behaviour, the utility of airborne electromagnetic (EM) surveying also warrants some consideration, although this survey technique is not a standalone airborne remote sensing method in this review.

Using the principles of EM induction in the subsurface, airborne EM is able to detect variations in electrical conductivity and resistivity across the subsurface (Milsom, 2003). Airborne EM methods are therefore sensitive to detecting subsurface structures which contain different fluid types, clay content and porosity. Subterranean targets responsive to EM induction are similar to those susceptible to aeromagnetic investigation and typically comprise buried trenches, pipelines, tunnels, caves, shallow faults and inorganic plumes (Reynolds, 1997).

During operation, the primary EM signal is already known and so, by employing a spatially constrained inversion (Table 8), it can be removed from the observed EM response in the receiver, leaving only the residual unknown target response from the subsurface (Viezzoli et al., 2008).

Airborne EM was recently used across the Huola Mountain Tunnel site in the Luntai County of the Mongolian Autonomous Prefecture of Bayingolin, central China (Zhang et al., 2023). This extremely large tunnel is part of the Cedaya-S340 Holgutu Highway Construction Project, where the tunnel is built inside a high mountain landform, creating a highway tunnel 8.5 km long and 1.3 km below ground. Prior to excavation and construction, an airborne EM survey was conducted using a ground-airborne frequency domain electromagnetic method (GAFEM) and a helicopter-borne time-domain electromagnetic method (HTEM). The EM survey identified the major stratigraphic boundaries and fault

fracture zones across the mountainous tunnel site (Table 8). Subsequently, the survey was able to evaluate the site for structural weakness, water content and karst development. The GAFEM revealed clear apparent resistivity profiles of deep sections across the tunnel site (200–2200 m in depth) whereas the HTEM generated high-resolution apparent resistivity images of shallow sections, ranging from 0 to 300 m in depth. The results were used to inform several geotechnical risk assessments prior to tunnel construction (Zhang et al., 2023).

An airborne EM survey was also conducted over the Damo Tunnel in Guangxi, southern China, where the tunnel site is known for its karst landforms. Here, Sun et al. (2023) use a UAV and a semi-airborne transient electromagnetic method (SATEM) for tunnel investigation (Sun et al., 2023). The SATEM requires a grounded-wire source to be placed along the ground surface above the tunnel, which transmits an electromagnetic field into the subsurface. Low resistivity targets near the tunnel are induced by the transmitter which produce secondary fields that are proportional to the size and location of the subterranean target. From above, an induction coil is carried by the UAV which acquires the first derivative of the secondary magnetic field with respect to time ($\partial B/\partial t$). The information collected by the airborne induction coil is then inverted and transformed into a series of 3D resistivity images across the tunnel site, depicting various underground electrical structures and the size and location of various subsurface conductors (Sun et al., 2023).

12. Verifying remote sensing observations of the subsurface

Subsurface detection from air and space needs validating, otherwise the techniques used to reveal subsurface irregularities from above the ground cannot be assured. This 'underground truthing' may constitute a number of forms, each with their own merits and each dependent on localised ground conditions, weather, time of year and the nature of the subterranean target being explored. In this appraisal, four verification practices are discussed, with one or more methods appearing in multiple papers from several authors.

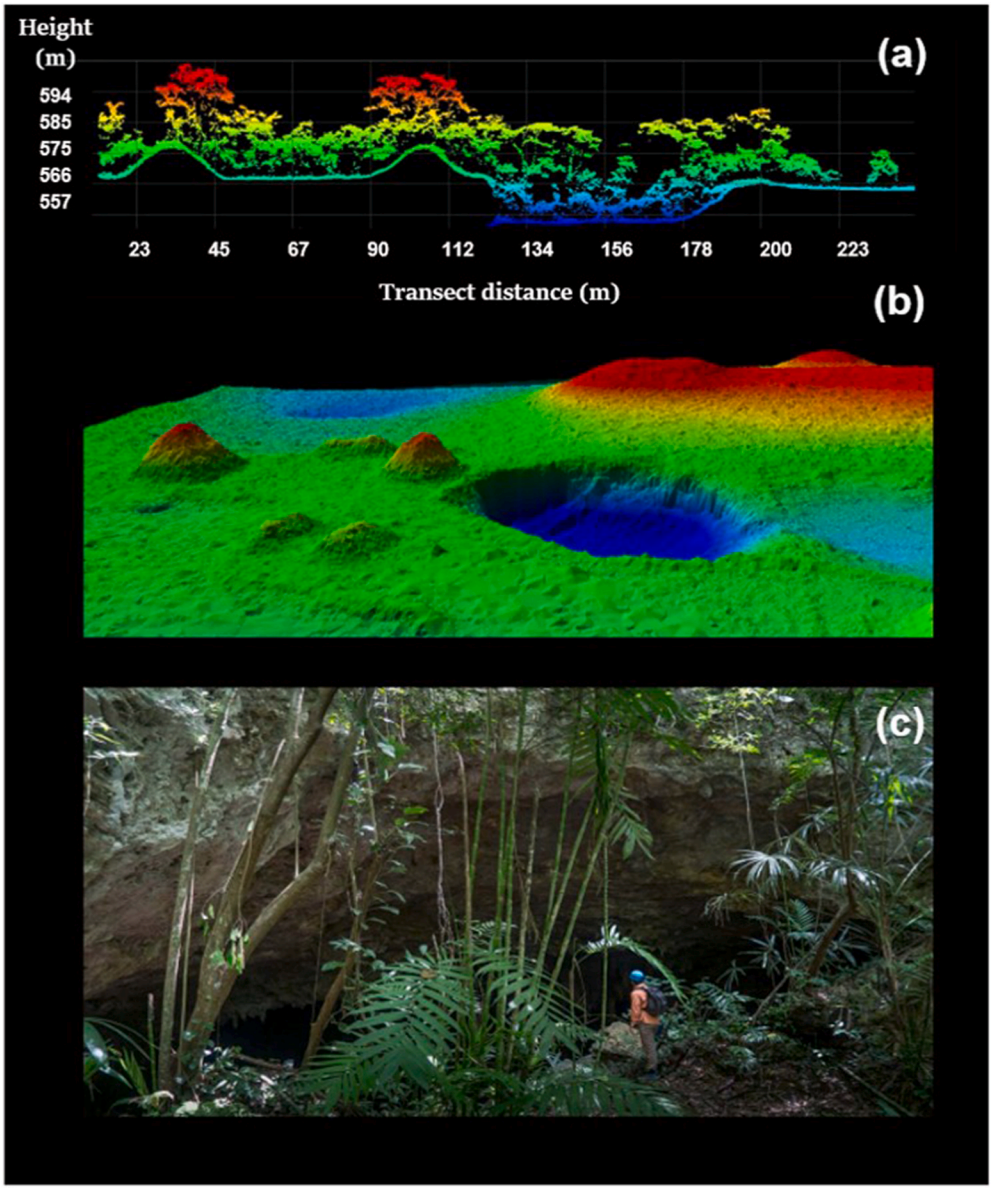

Fig. 16. A cave opening inside a sinkhole in the Las Cuevas study site in Belize (Moyes and Montgomery, 2019): a). Transect of an airborne LiDAR point cloud across a cave opening and sinkhole (in blue); colours represent surface elevation in metres. b). 3D DEM of sinkhole (in blue) and surrounding surface structures. c). Photo of a Las Cuevas cave entrance found at the base of the sinkhole during site reconnaissance.

12.1. Ground reconnaissance

The first technique in which to ground truth air and space remote sensing anomalies of the subsurface is ground reconnaissance. Often coined 'pedestrian survey', this technique requires GPS positioning on the site, a simple visual inspection and, on occasion, specialist cameras (Thompson and Marvin, 2005) and 3D modelling applications (Ekaran, 2022). Measurements can often accompany a pedestrian survey to validate any geometrical relationships and anomalous surface elevation configurations seen from air and space. Terrestrial laser scanning is also a useful ground survey technique, especially when there is a requirement to accurately model the above and below ground spatial characteristics of a subterranean site in three dimensions (Konsolaki et al., 2022; Wang et al., 2014).

Moyes and Montgomery (2019) undertook pedestrian surveys to validate the identification of several potential cave openings in the Chiquibul Forest Reserve in Belize, where local relief modelling from lidar-derived images was used to identify vertical and horizontal cave openings in valleys, depressions and side slopes. The LiDAR results steered their pedestrian survey efforts, reducing the time spent on the ground searching for particular cave sites in dense forest. The location of 14 ancient Mayan caves were confirmed in-person and a further 26 non-Mayan cave openings were proven to align with their airborne LiDAR analysis (Fig. 16), resulting in an 86% success rate. Furthermore, by visiting the caves in-person, the accuracy of their LiDAR detection routines could be evaluated. Similarly, Pisani and De Waele (2021) used a pre-existing cave register from the Atacama Desert and pedestrian survey to confirm the location of several candidate cave entrances across the Cordillera de la Sal (CDS) in Chile. These ground truthing methods verified the quality and reliability of their remote sensing derived cave entrances, where they used 600 km^2 of Pléiades imagery and several DTMs from stereographic couples to map the lithological units, the drainage network and the cave entrance points.

12.2. Field spectroscopy

Field spectroscopy is a terrestrial technique used to measure the reflectance properties of vegetation, soil, rock and water bodies in the natural environment, generally under solar illumination (Milton et al., 2009). Over a subsurface anomaly, it can be used to calibrate and validate the spectral observations recorded by an airborne or spaceborne multispectral or hyperspectral imaging system (Themistocleous et al., 2018). Typically, a field spectrometer will accurately record the intensity of reflected solar light at many different wavelengths in the EM spectrum, generating spectral reflectance profiles for specific objects with percentage reflectance values typically recorded from 300 nm to 2500 nm wavelengths (Milton et al., 2009). Therefore, pending the depth of the subterranean anomaly, reflectance spectrums of the ground matrix (soil/sand and overlying vegetation) above a subsurface structure are expected to yield different reflectance spectra to the surrounding landscape. These in situ reflectance spectrums are then compared with reflectance spectra from the airborne and spaceborne multispectral/hyperspectral imagery, calibrating the spectral resolution of the remote imaging sensor and validating the presence of a subsurface anomaly.

As an example, Agapiou et al. (2010) compare field spectroscopy observations over the Kouklia Palaepaphos archaeological site in Cyprus with magnetic anomalies in a previous geophysical survey. They used a GER 1500 field spectrometer to produce several spectral reflectance profiles across the site and in turn, observe multiple spectral vegetation anomalies over the buried archaeological features. They witnessed real benefits in incorporating field spectroscopy measurements with a multispectral time series analysis, where optimal time windows for vegetation reflectance anomalies could be determined using field spectroscopy prior to undertaking any imagery analysis of the subsurface across larger regions of the study site. Similar observations were also recorded by Melillos et al. (2019), who use a similar field spectroscopy method to verify and augment Sentinel-2A anomalies above underground military structures in Cyprus.

12.3. Geophysical Survey

To guarantee subsurface anomalies are present below ground, geophysical surveys are recommended. Many applied geophysical techniques exist, all responding to particular physical properties in the subsurface (Fig. 17). Much like air and space remote sensing, both active and passive methods exist. Active methods transmit artificially generated signals into the ground which are then modified in response to the characteristics of the materials in which they travel (Everett, 2013). Passive methods are those that detect variations in the Earth's natural fields (e.g., gravity and magnetics). All methods rely on specific physical properties in the subsurface, indicating that the optimal geophysical technique is very much dependent on the type of subsurface structure being investigated and the local ground conditions in which it rests (Butler, 2008). According to Fig. 17 (adapted from Reynolds (1997) and Morley (2011)), electromagnetics, resistivity, GPR and magnetic survey are the most versatile geophysical methods for subsurface detection, where each method is classified as a primary survey technique for at least 50% of the applications illustrated. Moreover, terrestrial gravity survey is also considered the most versatile augmentation (i.e., secondary) technique in any geophysical survey.

Butcher et al. (2006) made full use of gravity augmentation when they imaged the Lamb Leer cave system in the Mendip Hills in Somerset, UK. During the summers of 2004 and 2006 a series of resistivity and microgravity profiles were performed across the cave system, where the resulting gravity data disproved the presence of a significant mass deficiency in the vicinity of a resistivity "high" that was previously believed to be a large subsurface chamber. Instead, the combined resistivity and gravity data revealed this area as an isolated section of highly resistive limestone which, some time ago, had been re-positioned by a local fault.

By undertaking different geophysical techniques over the same subsurface target, confidence levels in the subsurface anomaly's location and character are enhanced, although these increased assurances must be carefully balanced with time, funding and resources (Berezowski et al., 2021). Several studies in this review use a multi-geophysical approach to verify subsurface observations (Berezowski et al., 2021; Ghezzi et al., 2019) although, as best practice, the pairing or grouping of such techniques should look to exploit different properties in the subsurface to optimise detection regimes and contextualise interpretation (Křivánek, 2017).

12.4. Integrated approach

A multi-sensor approach will increase subsurface detection assurances and evidently much work has been done to demonstrate this. For example, Lin et al. (2011) use high resolution GeoEye-1 satellite imaging, UAV photography and sub-surface geophysical investigation to detect ancient subsurface features at a Bronze Age burial mound, a Turkish period tomb and a steppe city fortification in northern Mongolia. Aerial photographs of the sites were obtained with two customized electric-powered UAVs (one fixed wing and one rotary) and geophysical investigation was conducted with a GSM-19 Overhouser gradiometer, an EM38 electro-magnetometer and an IDS Opera Duo GPR. The satellite imagery and aerial photographs were combined with the geophysical survey results and on-site reconnaissance to strengthen the reliability and accuracy of the detection regime and the location and nature of the ancient anomalies, all of which were depicted in multiple layers of data.

Similar sensor fusion techniques were also employed by Kalayci et al. (2017) who integrated electromagnetic induction, magnetic survey and GPR with historical aerial photography, multispectral imagery analysis

Geophysical Method	Physical Property	Subsurface Application (see key) 1	2	3	4	5	6	7	8	9	10
Gravity/Microgravity	Density	P	P	S	S	S	S	!	!	S	!
Magnetic Surveying	Susceptibility	P	P	P	S	!	M	!	P	P	!
Seismic Reflection	Elastic moduli; Density	P	P	M	P	S	S	!	!	!	!
Seismic Refraction	Elastic moduli; Density	P	P	M	S	S	M	!	!	!	!
Electrical Resistivity	Resistivity	M	M	P	P	P	P	P	S	P	M
Spontaneous Potential	Potential Differences	!	!	P	M	P	M	M	M	!	!
Induced Polarization	Resistivity; Capacitance	M	M	P	M	S	M	M	M	M	M
Electromagnetic Induction	Conductance; Inductance	S	P	P	P	P	P	P	P	P	M
Ground Penetrating Radar (GPR)	Permitivity; Conductivity	!	!	M	P	P	P	S	P	P	P
Magneto-telluric	Resistivity	S	P	P	M	M	!	!	!	!	!

Subsurface Application:

1 = Hydrocarbon Exploration
2 = Regional Geological Study
3 = Mineral Exploration
4 = Engineering Site Investigation
5 = Hydrogeological Investigation
6 = Subsurface Cavity Detection
7 = Leachate and Continental Plume Mapping
8 = Buried metal object detection
9 = Archaeogeophysics
10 = Forensic Geophysics

Key:

P = Primary Method
S = Secondary Method
M = May be used but not recommended
! = Unsuitable

Fig. 17. Principal geophysical methods and the subsurface properties they exploit. Each geophysical method is graded as either a primary (P), secondary (S), not recommended (M) or unsuitable (!) survey technique for ten subsurface exploration programmes listed on the right. Adapted from Reynolds (1997) and Morley (2011).

(from high-resolution WV2 and GeoEye-1 commercial satellite sensors) and a high resolution DTM from imagery taken by a UAV. Subsequently, this sensor rich and data heavy approach resulted in several comprehensive subsurface pictures of Neolithic settlements in Thessaly, Central Greece, revealing the dynamic character and structure of Neolithic enclosures, communal spaces and economic centres. More recently, Gaber et al. (2020) mapped groundwater potentials across the West Qena Area in Egypt by integrating an SRTM DEM with Landsat-8, ALOS/PALSAR-1 and Sentinel-1 imagery, geological data and soil maps. Furthermore, aeromagnetic data was processed to map the deep-seated structures across the same region, estimating the depth to the basement rocks that were believed to control the groundwater occurrence. Finally, vertical electrical sounding (VES) measurements were applied and calibrated with borehole data to delineate the subsurface geological and hydrogeological setting as well as the groundwater aquifers. Different geoelectric cross-sections and hydro-geophysical maps were then constructed using the borehole information and VES measurements to illustrate the lateral extension of the different lithological units, groundwater-bearing zones, water table and saturated aquifer thickness.

13. Future perspectives

This review identifies several promising research opportunities for the future. In particular, the spatial, spectral, radiometric and temporal integrity of high-quality airborne and spaceborne imagery now provides the data needed to perform VHR investigations of anomalous reflectance behaviour from vegetation and soil overlying near subsurface anomalies. Improved open access to high-resolution and VHR airborne and spaceborne remote sensing datasets is also encouraging, where the supremacy of deep learning techniques like multi-branch CNNs must continue to be employed on multi-sensor datasets, improving the likelihood and reliability of subsurface detection. We also identify the need to explore the detection sensitivities of active remote sensing techniques in variable potential fields. Revealing the subsurface density structure of semi-rigid structures using SAR tomography is of particular interest. Grouping these future research perspectives into three distinct study fields, we consider the detail of each.

13.1. Very high resolution (VHR) time series analyses

The ground conditions above and around subsurface structures continually change with time, and ground signatures from soil composition, heat retention, groundwater behaviour and surface elevation may be transformed and accentuated by natural and human processes. As we have demonstrated, airborne and spaceborne remote sensing applications may exploit such anomalous temporal behaviours, but are often limited by the spatial, temporal, radiometric and spectral resolutions of the sensor. Given recent advances in sensor technology and platform revisit times, we identify a need to further develop an understanding of the temporal behaviour of subsurface anomaly characteristics, with an emphasis on understanding how time affects the prominence of remotely sensed subsurface anomalies in contrast to the surrounding landscape or surface environment. In the future, investigations could entail a VHR multispectral, hyperspectral, TIR and/or LiDAR time series analysis of ground reflectance characteristics, soil matrix irregularity, thermal emissivity and land subsidence over near-surface tunnels and caves. Very high spatial, spectral and temporal resolution datasets are needed to achieve this, a demand which, for example, could be accomplished with high performing UAV-optimized imaging sensors and very high-resolution commercial satellites like Pléiades Neo and SatVu (for thermal change). When considering spaceborne observation, image fusion techniques with temporally-rich Planet images will generate numerous high-resolution multispectral images over short time periods, allowing the advantages of time-series analyses to accentuate any spectral anomalies over subsurface features (c.f. Agapiou et al., 2013a). The validity of such anomalies can then be correlated statistically with field spectroscopy, geophysical survey or integrated multi-sensor data.

13.2. Multi-branch convolutional neural networks (CNNs) on multi-sensor data

The multi-sensor integrated approach (reviewed in Section 12.4) is ready to evolve, where semi-automatic to fully automated subsurface detection routines are forged to make full use of the various airborne and spaceborne remote sensing datasets now available. Many more of the detection techniques presented in our technique tables (Tables 2–8) could be employed concurrently to increase the accuracy and reliability

of subsurface detection. Here, multi-sensor subsurface detection algorithms could be designed to systematically search for anomalies in the visual, spectral, thermal, spatial, gravitational and magnetic domains concurrently to assess the likelihood of subsurface anomalies existing in user designated locations. Object-based image analysis (OBIA) using multi-sensor datasets has already been well employed in archaeological prospecting (e.g., Davis, 2019; Freeland et al., 2016; Lasaponara and Masini, 2018) although much could still be done to incorporate this analysis with geophysical datasets, GIS analysis and machine learning. In the past, predictive models in GIS have been used, in conjunction with remote sensing datasets, to locate areas with high archaeological potential (Nsanziyera et al., 2018), high groundwater potential (Gaber et al., 2020) and high geothermal potential (Abuzied et al., 2020) but now, various machine learning techniques are well placed to forge a larger and more reliable integration platform (Shirmard et al., 2022). Xu et al. (2018) have already set a promising benchmark, successfully training a two-branch convolutional neural network (CNN) to "feature fuse" hyperspectral imagery with LiDAR data and then classify specific ground features, including that of surface proxies for subsurface anomalies (e.g., stressed grassland). Therefore, if optimal detection parameters are defined by subsurface target type and landscape condition (for multiple different sensor types), a multi-branch CNN could strive to statistically detect composite subsurface anomalies from the seven subsurface anomaly characteristics discussed in this paper.

13.3. Active remote sensing in variable potential fields

This review has identified the need for new and innovative approaches to remotely detect subsurface density changes and magnetic field variations from near-surface structures. As seen in Fig. 4, little airborne or spaceborne remote sensing methodology exists outside of traditional airborne gravity and magnetic survey to identify these subsurface characteristics. However, Biondi (2022) and Biondi and Malanga (2022) have begun to address this, showcasing SARs tomographic ability to image density variations inside volcanoes and ancient pyramids from space. We see potential in trialling similar techniques on semi-rigid structures like grass covered tors and caves, where SAR returns are typically less coherent. Such innovation uses photons as a carrier medium for phononic information, inviting readers to think about other ways in which photons could reveal the presence of subsurface anomalies, particularly when changes in the Earth's gravitational and magnetic field are present.

14. Concluding Remarks

Considering the use of eight different sensor types, this review identifies five principal motivations for remote sensing the subsurface from air and space. As illustrated in Fig. 2, these are: archaeological prospecting, environmental risk mitigation, natural resource exploration, defence and security and speleological research. The distinct ground indicators and potential field characteristics of a subsurface anomaly have also been categorised (Table 1 and Fig. 3), allowing the review to document all published use cases by sensor type, research motive and subsurface anomaly characteristic. By doing so, the review reveals that 78% of appraised photogrammetry papers exploit visible signatures across previously known archaeological sites; 43% of multispectral papers detect soil matrix irregularities over buried archaeological features; anomalous groundwater behaviour can be identified using all major sensor types less airborne gravity and aeromagnetics; heat retention anomalies are a suitable subsurface proxy for all research motives; changes in subsurface density are detected or assisted with airborne gravity, airborne LiDAR and SAR; 57% of LiDAR papers and 50% of SAR papers exploit changes in surface elevation (Fig. 4).

In total, over seventy air and space remote sensing techniques have been identified across the eight sensor types considered in this review (Tables 2–8), each designed to accentuate subsurface anomalies in the visible, spectral, thermal, spatial, gravitational or magnetic domains through the exploitation of a subsurface anomaly's visual markings, surrounding soil matrix, groundwater regime, surface elevation, heat retention, density distribution and magnetic susceptibility. By pooling these techniques together in seven technique tables that differentiate the subsurface anomaly characteristic being pursued, the investigable feature being detected and the remote sensor type used (Tables 2–8), the review exposes an extensive suite of tools and techniques for channelling subsurface detection studies with multiple sensors in different landscapes.

The importance of verifying remotely sensed observations of the subsurface from air and space has also been emphasised, recommending ground reconnaissance, field spectroscopy, geophysical survey and a multi-sensor integrated approach as the preferred means to calibrate and validate any prospective anomalies. Finally, the review considers future steps in remote sensing the subsurface, recommending the need for more VHR time series analyses over subsurface anomalies and further technical exploitation of CNNs, multi-sensor classification and quantum information protocols.

CRediT authorship contribution statement

Adam M. Morley: Writing – review & editing, Writing – original draft, Visualization, Resources, Project administration, Methodology, Investigation, Formal analysis, Conceptualization. **Tamsin A. Mather:** Writing – review & editing, Supervision. **David M. Pyle:** Writing – review & editing, Supervision. **J-Michael Kendall:** Writing – review & editing, Supervision.

Declaration of competing interest

The authors declare that they have no known competing financial interests or personal relationships that could have appeared to influence the work reported in this paper.

Acknowledgements

We thank those who authorised the use of copyrighted figures from other journals and in particular, the advice and permissions received from Elsevier and the National Speleological Society (NSS). We would also like to thank the British Army External Placements (Academic) programme and Dr Antony Butcher from the University of Bristol for their support during the review. Finally, we thank all reviewers and handling editors for their careful reading, useful advice and insightful feedback. This review did not receive any specific grant from funding agencies in the public, commercial or not-for-profit sectors.

Appendix A. Major spaceborne imaging sensors for passive Earth observation

Table A1
Table listing some of the major spaceborne imaging sensors for passive Earth observation, ordered by launch year. The list of panchromatic (PAN), multispectral (MSI) and thermal infrared (TIR) imaging sensors is not exhaustive; all entries are sourced from the European Space Agency's 'Satellite Mission Catalogue' on the eoPortal (ESA, 2023).

Satellite/Sensor	Sensor Type	No of Spectral Bands	Spectrum (nm)	Launch Year	Spatial Resolution (m)		Remarks
					PAN	VIS – NIR/ SWIR/TIR	
LANDSAT-1/MSS	MSI	7	500–1100	1972	N/A	79	Landsat was a pioneering land remote sensing programme, conceived by USGS and NASA. Landsat satellites 1–4 used a Multispectral Scanner (MSS).
LANDSAT-2/MSS	MSI	7	500–1100	1975	N/A	79	
LANDSAT-3/MSS	MSI	7	500–1100	1978	N/A	79	
LANDSAT-4/TM	MSI + TIR	7	450–12500	1982	N/A	30 + 120 (TIR)	Thematic Mapper (TM) is a multispectral mechanically scanning optical imager which images in the visible, infrared and thermal spectrum.
LANDSAT-5/TM	MSI + TIR	7	450–12500	1984	N/A	30 + 120 (TIR)	
SPOT-1/HRV	PAN + MSI	3	500–890	1986	10	20	Satellite Pour l'Observation de la Terre was a commercial earth-imaging satellite from CNES, the French Space Agency.
IRS-1A	MSI	4	450–860	1988	N/A	36	
SPOT-2/HRV	PAN + MSI	3	500–890	1990	10	20	
JERS-1/OPS	MSI	8	520–2400	1992	N/A	18.3	JERS-1 (Japan Earth Resources Satellite) generated data on geological phenomena, agriculture and forestry land usage, coastal regions and environment/disaster management. It features both optical and SAR instruments.
SPOT-3/HRV	PAN + MSI	3	500–890	1993	10	20	
IRS-P2	MSI	4	450–860	1994	N/A	23.5	
IRS-1C	PAN + MSI	4	500–1750	1995	5.8	23.5	IRS-1C and -1D are EO satellites from the Indian Space Research Organisation (ISRO).
IRS-1D	PAN + MSI	4	500–1750	1997	5.8	23.5	IRS-1C and -1D carried three pushbroom sensors. Two were optical imagers with different swaths and spatial resolutions: Linear Imaging Self Scanner-III (LISS-III) and Panchromatic Sensor (PAN). The other sensor was an imaging radiometer called WiFS (Wide Field Sensor).
SPOT-4/HRVIR	PAN + MSI	4	500–890	1998	10	20	
CBERS-1/CCD	PAN + MSI	4	420–890	1999	3	20	Operated as part of the China-Brazil Earth Resources satellite programme.
IKONOS - 2	PAN + MSI	4	450–900	1999	1	4	Launched by Space Imaging in 1999, Ikonos-2 was the world's first commercial high-resolution imaging satellite.
LANDSAT-7/ETM+	PAN, MSI + TIR	7	450–12500	1999	15	31 + 60 (TIR)	Landsat-7 features the Enhanced Thermal Mapper Plus (ETM+) developed by Raytheon SBRS (Santa Barbara Remote Sensing), building upon the Thematic Mapper (TM) onboard Landsat-4 & −5.
TERRA/ASTER	MSI + TIR	14	520–860	1999	N/A	15 + 30 (SWIR) + 90 (TIR)	Terra (formerly known as EOS/AM-1) is a joint mission within NASA's ESE (Earth Science Enterprise) programme between the US, Japan and Canada. The Advanced Spaceborne Thermal Emission and Reflection Radiometer (ASTER) is a Japanese sensor with visible, NIR, SWIR and TIR sensor range. TERRA also carries four additional remote sensors: CERES (Clouds and the Earth's Radiant Energy System); MISR (Multi-angle Imaging SpectroRadiometer); MODIS (Moderate-resolution Imaging Spectroradiometer); MOPITT (Measurements of Pollution in the Troposphere).
EO-1/ALI	PAN + MSI	8	433–890	2000	10	30	Managed and operated by NASA's Goddard Space Flight Centre, featuring the Advanced Land Imager (ALI) sensor.
QUICKBIRD −2	PAN + MSI	4	450–900	2001	0.61	2.4	DigitalGlobe (now Maxar Technologies), launched QuickBird-2 from California, USA in October 2001.
PROBA-1	PAN + MSI	62	450–1050	2001	5	18	The Project for On-Board Autonomy - 1 (PROBA-1) is a minisatellite technology demonstration mission in ESA's General Study Program, aiming to tackle issues related to the on-board operational autonomy of a generic platform. It features the Compact High-Resolution Imaging Spectrometer (CHRIS).
SPOT-5/HRG	PAN + MSI	4	480–1750	2002	5	10	
IRS-P6 (RESOURCESAT-1)/LISS-IV	MSI	3	520–860	2003	N/A	5.8	Indian Remote-Sensing Satellite-P6 (IRS-P6), renamed ResourceSat-1, was an optical imaging satellite operated by the Indian Space Research Organisation (ISRO).
ORBVIEW-3	PAN + MSI	4	450–900	2003	1	4	A US commercial high-resolution imaging minisatellite developed by Orbital Imaging Corporation. In 2006, ORBIMAGE merged with Space Imaging of Thornton, Colorado USA, to establish the commercial imaging company GeoEye.
NIGERIASAT-1	MSI	3	450–900	2003	N/A	32	

(*continued on next page*)

Table A1 (*continued*)

Satellite/Sensor	Sensor Type	No of Spectral Bands	Spectrum (nm)	Launch Year	Spatial Resolution (m)		Remarks
					PAN	VIS – NIR/ SWIR/TIR	
DMC-1G/SLIM6	MSI	3	520–900	2003	N/A	32	The Disaster Monitoring Constellation (DMC) is an international program initially proposed in 1996 and led by SSTL (Surrey Satellite Technology Ltd), Surrey, UK, to construct a network of five affordable LEO microsatellites. The objective is to provide a daily global imaging capability at medium resolution (30–40 m) in 3–4 spectral bands for rapid-response disaster monitoring and mitigation.
CBERS-2	PAN, MSI + TIR	4	420–890	2003	2.7	20 + 160 (TIR)	
IRS-P5/CartoSat-1	PAN	0	500–750	2005	2.5	N/A	IRS-P5 is a spacecraft of ISRO. The mission objectives included geo-engineering (mapping) applications, requiring high-resolution panchromatic imagery with high pointing accuracies. The spacecraft features two high-resolution panchromatic cameras that may be used for in-flight stereo imaging.
ALOS/PRISM + AVNIR-2	PAN + MSI	4	420–890	2006	2.5	10	Advanced Land Observing Satellite (ALOS) was a Japanese EO mission.
KOMPSAT-2/MSC	PAN + MSI	4	450–900	2006	1	4	Launched in July 2006, KOMPSAT-2 (Korea Multi-Purpose Satellite) was developed and operated by KARI (Korea Aerospace Research Institute).
IRS-P5/CartoSat-2	PAN	0	500–850	2007	1	N/A	
WORLDVIEW-1	PAN	0	450–900	2007	0.5	N/A	WorldView-1 (WV-1) is a commercial mission owned and operated by Maxar Technologies Inc. WV-1 is the successor to QuickBird-2 and aims to provide high spatial resolution imagery of the Earth's surface to defence, intelligence and commercial industries.
GEOEYE-1	PAN + MSI	4	450–920	2008	0.41	1.65	Included in the WorldView constellation and operated by Maxar.
PLANET - RAPIDEYE	MSI	5	440–850	2008	N/A	6.5	The RapidEye Earth observation system was a commercial constellation of five minisatellites, originally owned and operated by BlackBridge and acquired by Planet Labs in 2015.
WORLDVIEW-2	PAN + MSI	8	400–1040	2009	0.46	1.84	Launched October 2009, WorldView-2 (WV-2) is a commercial imaging satellite, owned and operated by Maxar Technologies Inc.
PLÉIADES-HR	PAN + MSI	4	430–915	2011	0.7	2.8	Pléiades 1A and 1B are a two-satellite environment focussed high resolution (HR) constellation from the French Space Agency, Centre National D'Etudes Spatiales (CNES).
NIGERIASAT-2	PAN + MSI	4	450–900	2011	2.5	5	NigeriaSat-2 is a Nigerian government imaging satellite and successor to NigeriaSat-1, produced by SSTL (Surrey Satellite Technology Ltd.) under a contract with the National Space Research and Development Agency (NASRDA) of Nigeria.
KOMPSAT-3/AEISS	PAN + MSI	4	450–900	2012	0.7	2.8	KOMPSAT-3 is a Korean Earth observation mission of KARI, funded by the Ministry of Education, Science and Technology and features an Advanced Electronic Image Scanning System (AEISS).
SPOT-6/HRG	PAN + MSI	4	455–890	2012	1.5	6	Owned and operated by Airbus Defence and Space.
GAOFEN-1/PMC	PAN + MSI	4	450–890	2013	2	8	Developed in Beijing by the China National Space Administration (CNSA).
LANDSAT-8/OLI	PAN + MSI	8	433–2300	2013	15	30	Features the Operational Land Imager (OLI) sensor.
LANDSAT-8/TIRS	TIR	2	10800–12000	2013	N/A	100	Features the Thermal Infrared Sensor (TIRS).
PLANET - SKYSAT	PAN + MSI	4	450–900	2013	0.86	1	The Planet SkySat constellation is comprised of 21 satellites which are tasked to image any point on Earth in very high resolution and at sub-daily frequency. They can also capture stereo imagery and video footage.
GAOFEN-2/PMC	PAN + MSI	4	450–890	2014	0.81	3.24	Developed in Beijing by the China National Space Administration (CNSA).
SPOT-7/HRG	PAN + MSI	4	455–890	2014	1.5	6	Owned and operated by Airbus Defence and Space.
WORLDVIEW-3	PAN + MSI	16	400–2365	2014	0.31	1.24	WV-3 also features 12 CAVIS (Clouds, Aerosols, Vapours, Ice, and Snow) bands which monitor the atmosphere and provide correction data to improve WV-3's high-resolution imagery through haze, soot and dust.
SENTINEL-2/MSI	MSI	13	450–2200	2015	N/A	10	Sentinel-2 is a constellation of two optical imaging satellites, which are a part of Copernicus - the European Union's Earth Observation (EO) programme.
PLANET - DOVES	MSI	4	450–900	2015	N/A	5	Planet Doves (CubeSats) are 10x10 × 30 cm in size.
DMC-3/SSTL 300 S1	PAN + MSI	3	450–900	2015	1	4	DMC-3 (Disaster Monitoring Constellation-3) is a constellation of three optical imagers owned and operated by DMCii (DMC International Imaging Ltd.). DMCii is a subsidiary of Surrey Satellite Technology Ltd. (SSTL), the world leader in small satellite technology.
WORLDVIEW-4	PAN + MSI	4	450–920	2016	0.31	1.24	WV-4 suffered a failure in one of its control moment gyroscopes in Jan 19 and operations ceased.

(*continued on next page*)

Table A1 (*continued*)

Satellite/Sensor	Sensor Type	No of Spectral Bands	Spectrum (nm)	Launch Year	Spatial Resolution (m)		Remarks
					PAN	VIS – NIR/ SWIR/TIR	
VISION-1	PAN + MSI	4	440–910	2018	0.87	3.48	
CBERS-4A/WPM	PAN + MSI	4	510–890	2019	2	8	The China-Brazil Earth Resources Satellite-4A (CBERS-4A) is an optical imaging satellite collaboratively operated by the China Centre for Resources Satellite and Data Application (CRESDA) and the Instituto Nacional del Pesquisas Espacias (INPE) - Brazil's National Institute of Space Research. CBERS-4A will be used to monitor water resources, agriculture, urban growth, and land use, with a large focus on the preservation of the Amazon rainforest.
PLANET - SUPER DOVES	MSI	8	430–885	2021	N/A	3.7	48 x Super Dove Planet satellites designed and configured to join the existing PlanetScope satellite constellation of c200 satellites.
PLÉIADES NEO	PAN + MSI	6	400–880	2021	0.3	1.2	Pléiades Neo is a constellation of very-high-resolution (VHR) optical satellites. The first two satellites were launched in 2021, and the final 2 satellites launched in 2022.

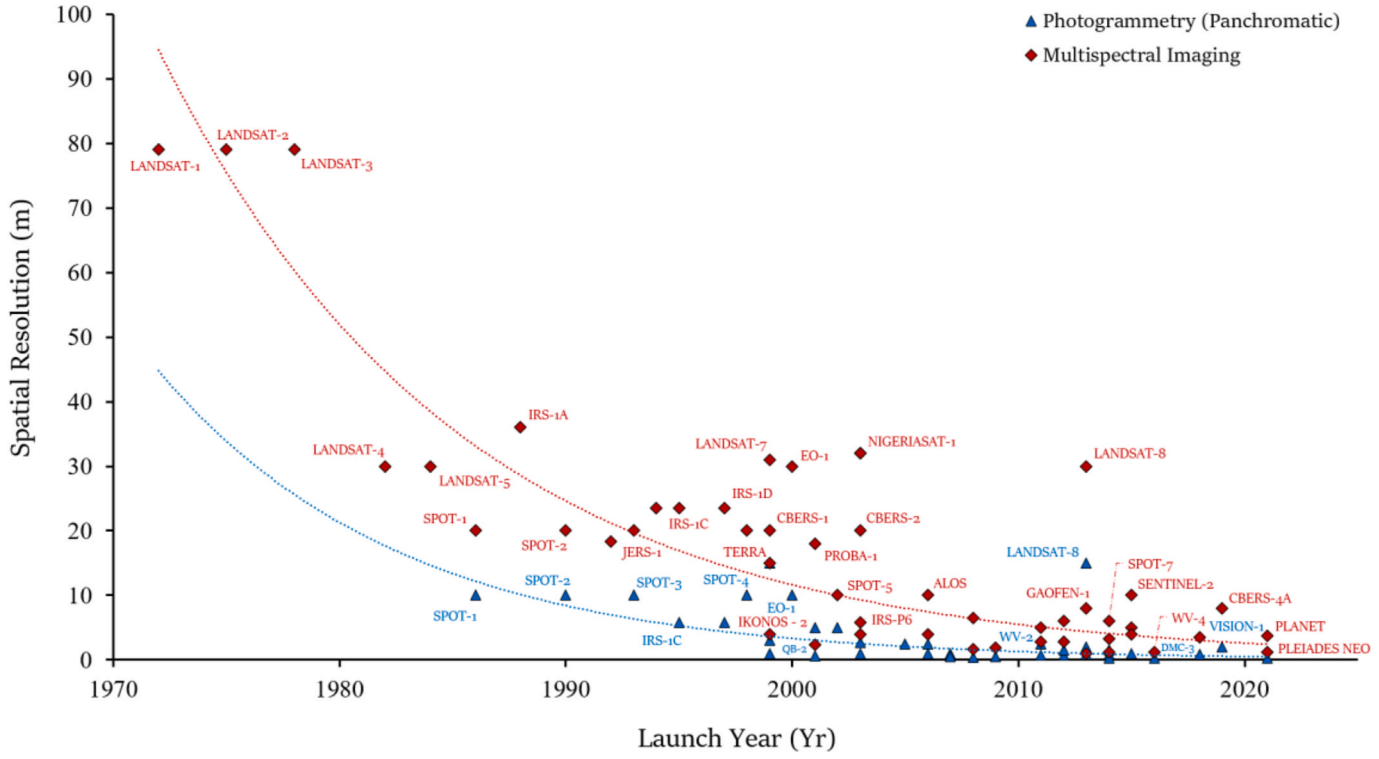

Fig. A1. Spatial resolution of passive spaceborne imaging sensors since 1972. The list of passive imaging sensors used in this scatter plot is not exhaustive; all data points are sourced from the European Space Agency's 'Satellite Mission Catalogue' on the eoPortal (ESA, 2023) and are tabulated in Table A1.

Appendix B. Major spaceborne imaging sensors for active Earth observation

Table B1
Table listing some of the major spaceborne imaging sensors for active Earth observation, ordered by launch year. The list of active imaging sensors (SAR sensors) is not exhaustive; all entries are sourced from the European Space Agency's 'Satellite Mission Catalogue' on the eoPortal (ESA, 2023).

Satellite/Sensor	Acquisition Mode	No of Bands	Polarization	Launch Year	Spatial Resolution (m)	Remarks
SEASAT	Active	1 (L)	HH	1978	25	SeaSat was a pioneering Earth observation experimental mission of NASA's Jet Propulsion Laboratory (JPL), demonstrating the viability of imaging radar for EO and becoming a precursor to many missions that investigated the Earth's oceans, land and ice.
SIR-A	Active	1 (L)	HH	1981	30	
SIR-B	Active	1 (L)	HH	1984	30	

(*continued on next page*)

Table B1 (*continued*)

Satellite/Sensor	Acquisition Mode	No of Bands	Polarization	Launch Year	Spatial Resolution (m)	Remarks
ALMAZ-1	Active	1 (S)	HH	1991	25	The Almaz programme (Russian for "diamond") was a military space programme of the former Soviet Union.
ERS-1	Active	1 (C)	VV	1991	30	The ERS-1 was the first environmental monitoring satellite developed by ESA. The mission detected land and ocean surface change and provided observation data on oceans, polar ice, vegetation, geology, meteorology and ecology.
JERS-1/SAR	Active	1 (L)	HH	1992	18	JERS-1 is a Japanese Earth Resources Satellite, designed to support a SAR and Optical mission - developed by The National Space Development Agency of Japan.
SIR-C/X-SAR	Active	3 (C, L, X)	All (L, C); VV (X)	1994	13 (L), 26 (C), 10 (X)	SIR-C/X-SAR (Spaceborne Imaging Radar C/X-band Synthetic Aperture Radar) was an imaging radar system developed by NASA, the German Space Agency (DLR) and the Italian Space Agency (ASI). It was used to obtain SAR imagery for scientific research, calibration, and technological experiments. SIR-C/X-SAR was a payload on the SRL-1 (Space Radar Laboratory-1) shuttle and the SRL-2 (Space Radar Laboratory-2).
ERS-2	Active	1 (C)	VV	1995	30	ERS-2 saw enhancements to the previous ERS-1 mission. ERS-2 provided microwave spectrum environmental monitoring across a range of disciplines including oceans, polar ice and forestry.
RADARSAT-1	Active (Scan SAR)	1 (C)	HH	1995	10	RADARSAT-1 was the first commercial Earth observation mission of the Canadian Space Agency (CSA). It used a microwave radar sensor to monitor environmental changes and Earth's natural resources, with applications in agriculture, land cover monitoring, forestry, disaster management, interferometry, cartography, hydrology, oceanography, ice studies and coastal monitoring.
SRTM	Active	2 (C, X)	HH + HV or VV + VH (C), VV (X)	2000	30	SRTM is a international shuttle mission between NASA, DoD/NGA (National Geospatial-Intelligence Agency), DLR (German Aerospace Center - Deutsches Zentrum für Luft- und Raumfahrt), and ASI (Agenzia Spaziale Italiana). The mission objective was to obtain single-pass interferometric SAR imagery to be used for Digital Elevation Model (DEM) generation. Coverage of the Earth's land surfaces is provided between the latitudes of -54° and $+60^{\circ}$, representing nearly 80% of the land masses.
ENVISAT/ASAR	Active (Image Mode)	1 (C)	HH or VV	2002	28	EnviSat was ESA's successor to ERS 1 & 2, designed to monitor the Earth's environment including: meteorology, climatology, environment, atmospheric chemistry, vegetation, hydrology, land use, and ocean and ice processes.
SAR - LUPE	Active (Spot Light)	1 (X)	VV	2006	0.5	SAR-Lupe is Germany's first satellite-based reconnaissance system, developed for the German Ministry of Defence. This SAR project consists of five identical satellites with the objective of providing high-resolution radar imagery to German defence forces.
ALOS/PALSAR	Active (Fine Beam)	1 (L)	HH or VV (single pol) HH + HV or VV + VH (dual pol)	2006	7	ALOS (Advanced Land Observing Satellite) was a Japanese Earth observation mission developed by JAXA (Japan Aerospace Exploration Agency). The mission's objectives required high resolution imagery for applications in cartographic mapping, regional observation, disaster monitoring and resource surveying. A PAN sensor (PRISM) and MSI sensor (AVNIR-2) were also part of the ALOS multi-sensor payload.
RADARSAT-2	Active	1 (C)	Fully polarimetric	2007	3	RADARSAT-2 is a jointly-funded satellite mission of CSA (Canadian Space Agency) and MDA (MacDonald Dettwiler Associates Ltd. of Richmond, BC), representing a Canadian government/industry partnership [or PPP (Public Private Partnership)] in a commercial venture. In Feb. 1998, CSA awarded a contract to MDA to build RADARSAT-2.
COSMO-SKY MED (CSK)	Active (Spot Light)	1 (X)	HH, VV, HV/VH	2007	1	COSMO-SkyMed (Constellation of Small Satellites for Mediterranean basin Observation - CSK) is a four-spacecraft constellation. The mission is jointly funded by the Italian Ministry of Research and the Italian Ministry of Defence and developed by Agenzia Spaziale Italiana (ASI) for both military and civil application. ScanSAR and StripMap acquisition modes also operational.
TERRASAR-X/TANDEM-X	Active (Spot Light)	1 (X)	(HH, VV), (HH/VV)	2007	1	TanDEM-X and TerraSAR-X are twin interferometric SAR satellites, funded in a public/private collaboration between the German Aerospace Centre (DLR) and Airbus Defence and Space. The satellites construct three-dimensional images of the Earth's surface in order to generate a World DEM; ScanSAR and StripMap acquisition modes are also operational.
SENTINEL-1	Active (Strip Map)	1 (C)	HH or VV (single pol) HH + HV or VV + VH (dual pol)	2014	5	Sentinel-1 is a constellation of two imaging radar satellites operated by ESA under the Copernicus programme. Sentinel-1B experienced an anomaly which rendered it unable to deliver radar data in December 2021, and the launch of Sentinel-1C is

(*continued on next page*)

Table B1 (*continued*)

Satellite/Sensor	Acquisition Mode	No of Bands	Polarization	Launch Year	Spatial Resolution (m)	Remarks
						planned for 2023. Interferometric Wide, Extra Wide and Wave acquisition modes are also operational on Sentinel-1A.
ALOS-2/PALSAR-2	Active (Spot Light)	1 (L)	VV/HH VV + HH	2014	1	ALOS-2 features PALSAR-2 (Phased Array type L-band Synthetic Aperture Radar-2) and a multi-purpose imaging vis/IR (visual/infrared) radiometer named CIRC (Compact InfraRed Camera). PALSAR-2 monitors Japanese natural disasters, land and agriculture and also explores natural resources in the ground and seabeds of Japan. The CIRC instrument measures land surface temperature and can detect and monitor active forest fires. ScanSAR and StripMap acquisition modes are also operational.
GAOFEN-3	Active (Spot Light)	1(C)	HH or VV	2016	1	Gaofen-3 is the third satellite in the China High-Resolution Earth Observation System (CHEOS) series. Developed by the China National Space Administration (CNSA), it is a civilian satellite and primary users include the State Oceanic Administration (SOA), the China Meteorological Administration (CMA), the Ministry of Civil Affairs and the Ministry of Water Resources.
ICEYE	Active (Spot Imaging)	1 (X)	VV	2018	1	The commercial ICEYE constellation is a constellation of X-band SAR Satellites. The ICEYE satellites provide high-resolution images the Earth's surface to enable better decision making based on the Earth observation data. Three other acquisition modes are employed; Spot extended area imaging, Strip imaging and Scan imaging.
PAZ	Active (High Res Spot Light)	1 (X)	HH or VV or VH or HV (single pol) HH + HV or VV + VH (dual pol)	2018	1	PAZ is an X band Synthetic Aperture Radar mission of Spain. It is a dual-use mission, aimed at serving the security and defence needs of the Ministry of Defence. PAZ is managed by Hisdesat, a Spanish commercial company that provides its service to the Ministry of Defence (who funded and own the satellite). Five other imaging modes are available.
SAOCOM	Active (Strip Map)	1(L)	HH or VV (single pol) HH + HV or VV + VH (dual pol) HH + HV + VV + VH (quad pol)	2018	10	Satélite Argentino de Observación COn Microondas (SAOCOM), which translates to Argentine MicroWave Observation Satellite, is a constellation of two satellites, SAOCOM-1A and SAOCOM-1B, owned and operated by the Argentinian Space Agency. The mission aims to provide effective Earth observation and disaster monitoring.
COSMO-SKY MED SECOND GENERATION (CSG)	Active (Spot Light)	1(X)	HH or VV or VH or HV (single pol) HH + HV or VV + VH (dual pol)	2019	0.35	The COSMO-SkyMed Second Generation (CSG) is a constellation of four satellites, aimed at enhancing the quality and capability of imaging of the original COSMO-SkyMed constellation (CSK). Ten different imaging modes are available.
CAPELLA X-SAR	Active (Staring Spot Light)	1(X)	HH	2021	0.3	Based in California, USA, the commercial start-up company Capella Space is developing the Capella X-SAR (Synthetic Aperture Radar) constellation consisting of 36 microsatellites to provide global high-resolution commercial SAR imagery. Imaging modes include Stripmap, multi-swath stripmap, staring spotlight and sliding spotlight.
Lu Tan-1 (LT-1)	Active (Strip Map)	1 (L)	HH or VV (single pol) HH + HV or VV + VH (dual pol)	2022	3	A Chinese satellite constellation consisting of two satellites: LT-1 A and LT-1 B. LT-1 is used for digital elevation model (DEM) generation and deformation monitoring. The constellation can also operate in ScanSAR imaging mode.

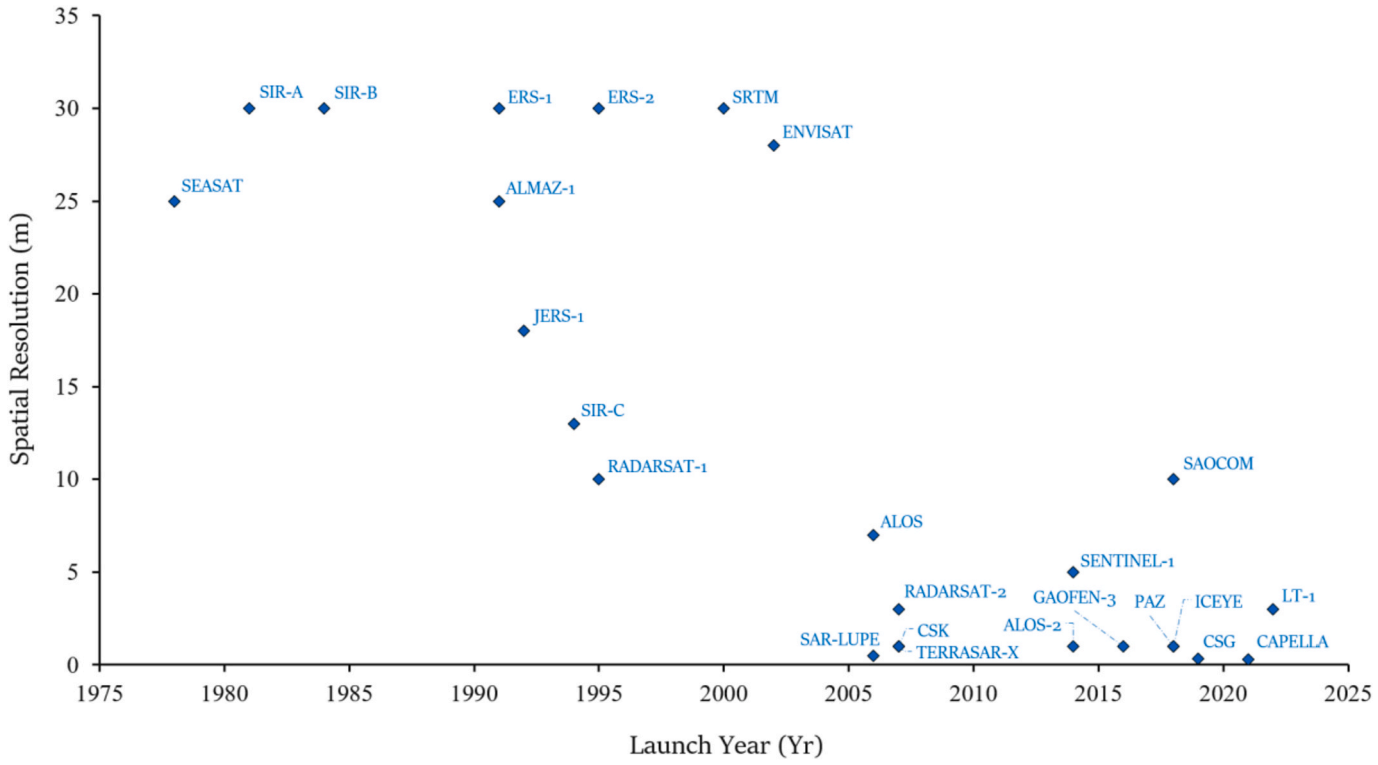

Fig. B1. Spatial resolution of active spaceborne imaging (i.e. SAR) sensors since 1978. The implementation of new SAR imaging modes from 2000 onwards has significantly increased the spatial resolution of spaceborne SAR. The list of SAR sensors used in this scatter plot is not exhaustive; all data points are sourced from the European Space Agency's 'Satellite Mission Catalogue' on the eoPortal (ESA, 2023) and are tabulated in Table B2.

Appendix C. Search strategy and paper statistics

The Google Scholar and Oxford University 'Search Oxford Libraries Online' (SOLO) databases were used to find and retrieve all papers examined in this review. The following search strings were used systematically to explore each database.

- **Search String #1**: [Reviewing/using] [remote sensing/insert sensor type] to find [tunnels/caves/mines/underground facilities/subsurface structures/underground cavities/underground voids]
- **Search String #2**: Remote sensing [tunnels/caves/mines/underground facilities/subsurface structures/underground cavities/underground voids] using (insert sensor type)

Each variable term in each search string was entered systematically to ensure all combinations of the search query were used in the Google Scholar and SOLO search engines. Results were filtered by "most relevant" in 'pass one' and "most recent" in 'pass two' for each string combination.

All papers reviewed were documented in a three-dimensional reference matrix (Figure C1) which registered the papers by the major sensor type used, the subsurface anomaly characteristic being investigated, and the authors' motivation for exploring the subsurface from air or space.

In total, 113 papers were reviewed in detail and 91 use cases (case studies) were appraised. Various percentages are calculated from Figure C1, acknowledging our assumption that the sample of papers reviewed is a fair and accurate representation of the entire population of subsurface remote sensing publications in circulation. Of note, 20% of all papers reviewed used LiDAR to detect subsurface features, followed by SAR (19%), hyperspectral imaging (15%), multispectral imaging (12%), thermal infrared (11%), airborne magnetics (10%), photogrammetry (8%) and airborne gravity (5%).

Also, of the 113 papers reviewed, 23% examined the visual indicators of near subsurface anomalies, 22% pursued surface elevation change, 17% identified soil matrix irregularities, 12% detected heat retention anomalies, 10% recorded magnetic field variations, 9% studied anomalous groundwater behaviour and 7% measured changes in subsurface density.

Finally, from an authors' motivational perspective, 38% used airborne and spaceborne remote sensing techniques to detect buried archaeological features, 31% were attempting to mitigate the risk from environmental hazards, 13% were finding natural resources, 11% were in support of defence and security activity and 7% were undertaking speleological research.

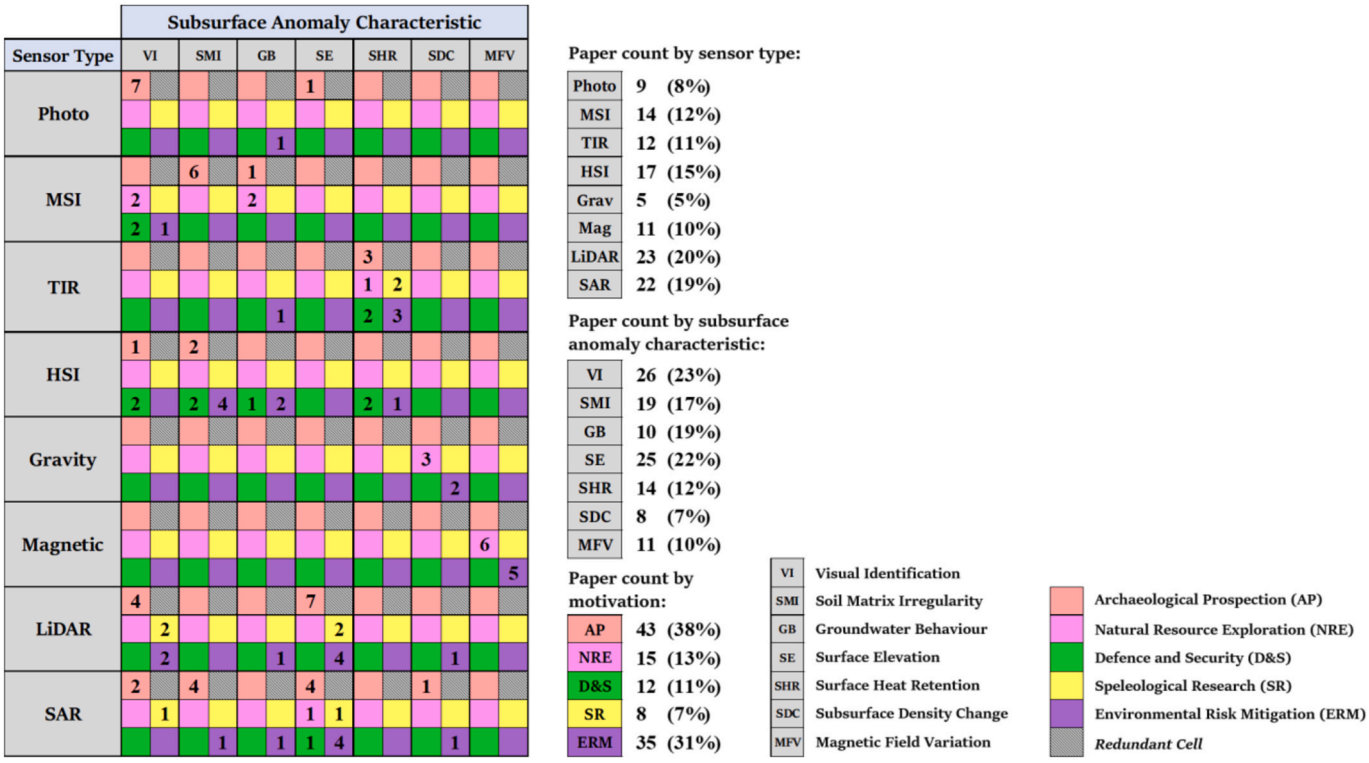

Fig. C1. Three-dimensional reference matrix for paper documentation and paper statistics. All papers reviewed were registered by the sensor type used, the subsurface anomaly characteristic being investigated and the author's motivation for exploring the subsurface from air or space. In total, and as documented above, 113 papers have been reviewed.

Appendix D. Principles of air and space remote sensors

Figures D1 to D8 are information flow graphics, each describing the fundamental principles that underpin the operation and application of each sensor type considered in this review. The arrows denote the logical flow of information, beginning with a baseline concept inside a coloured text box.

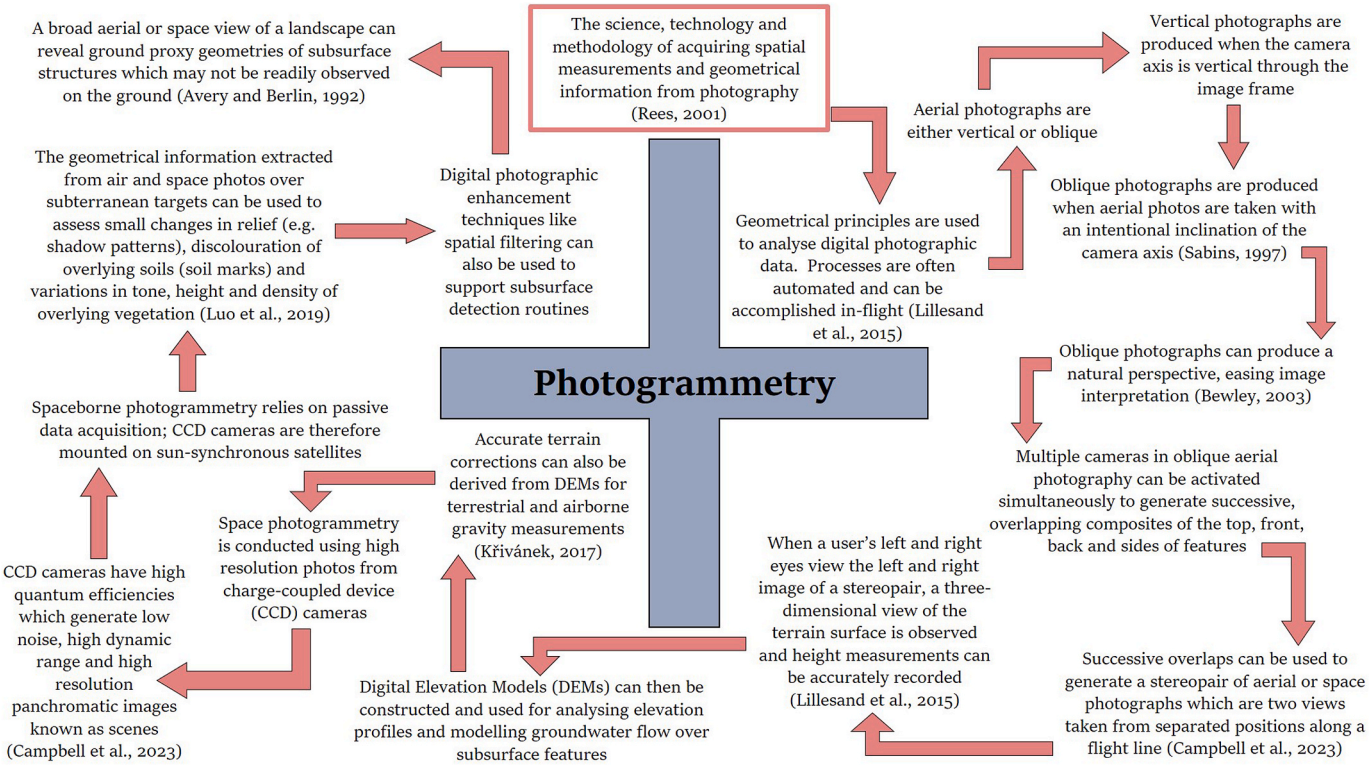

Fig. D1. Principles of air and space photogrammetry. Red box denotes beginning of flow graphic and red arrows depict flow of information.

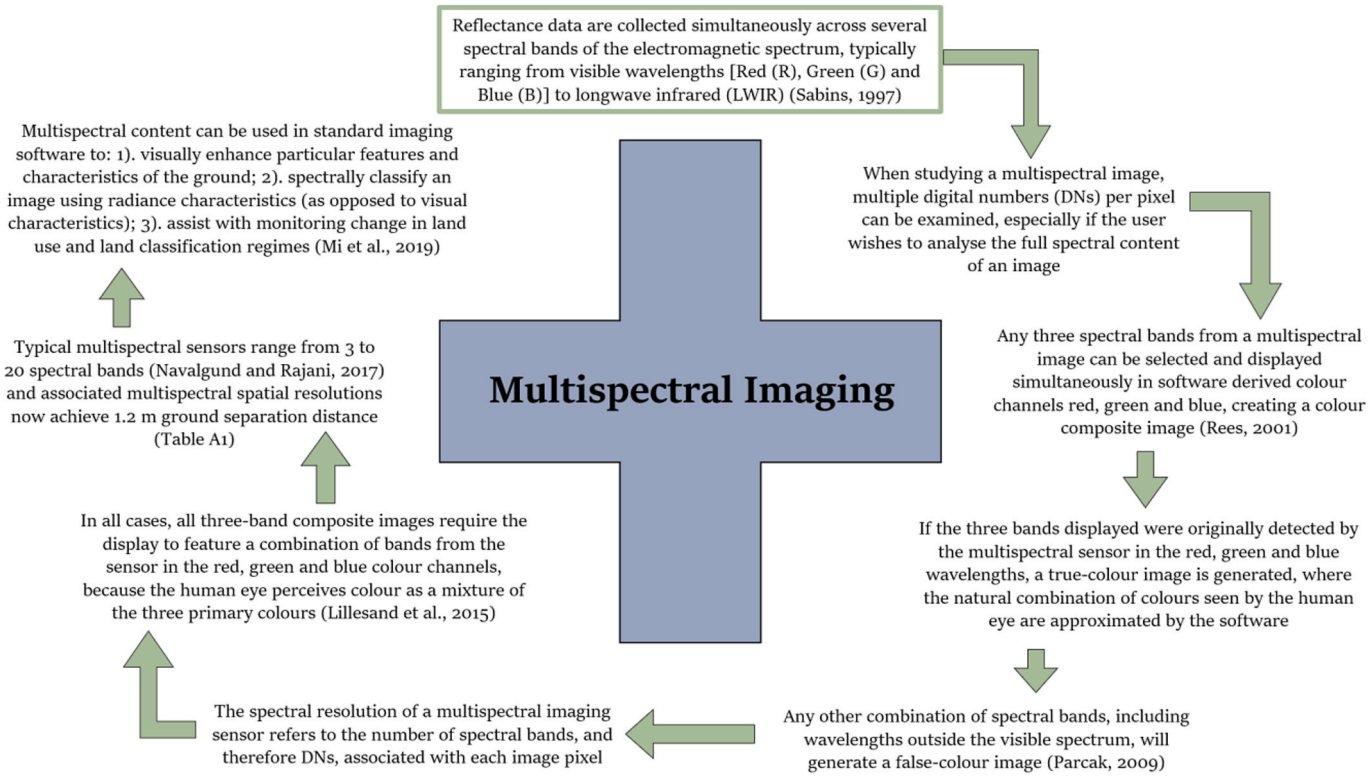

Fig. D2. Principles of multispectral imaging. Dark green box denotes beginning of flow graphic and dark green arrows depict flow of information.

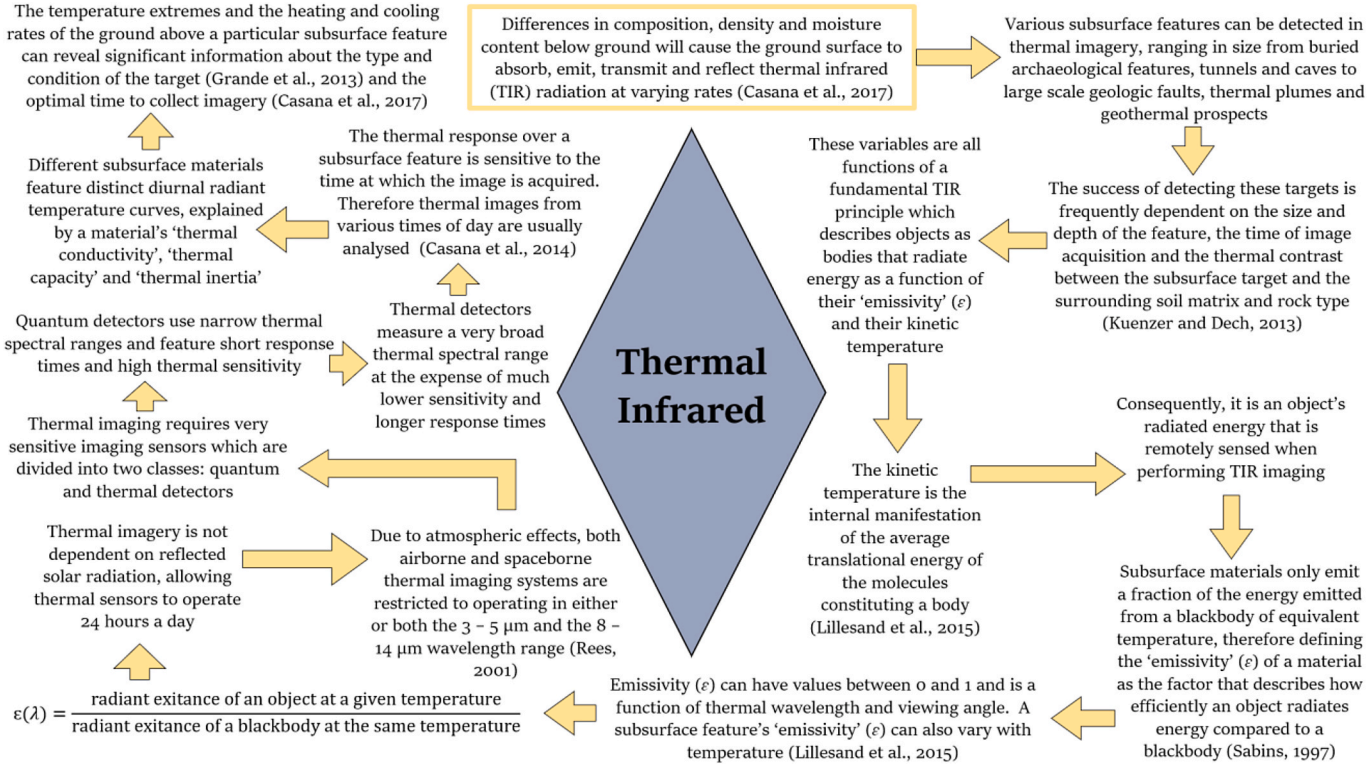

Fig. D3. Principles of thermal infrared imaging. Yellow box denotes beginning of flow graphic and yellow arrows depict flow of information.

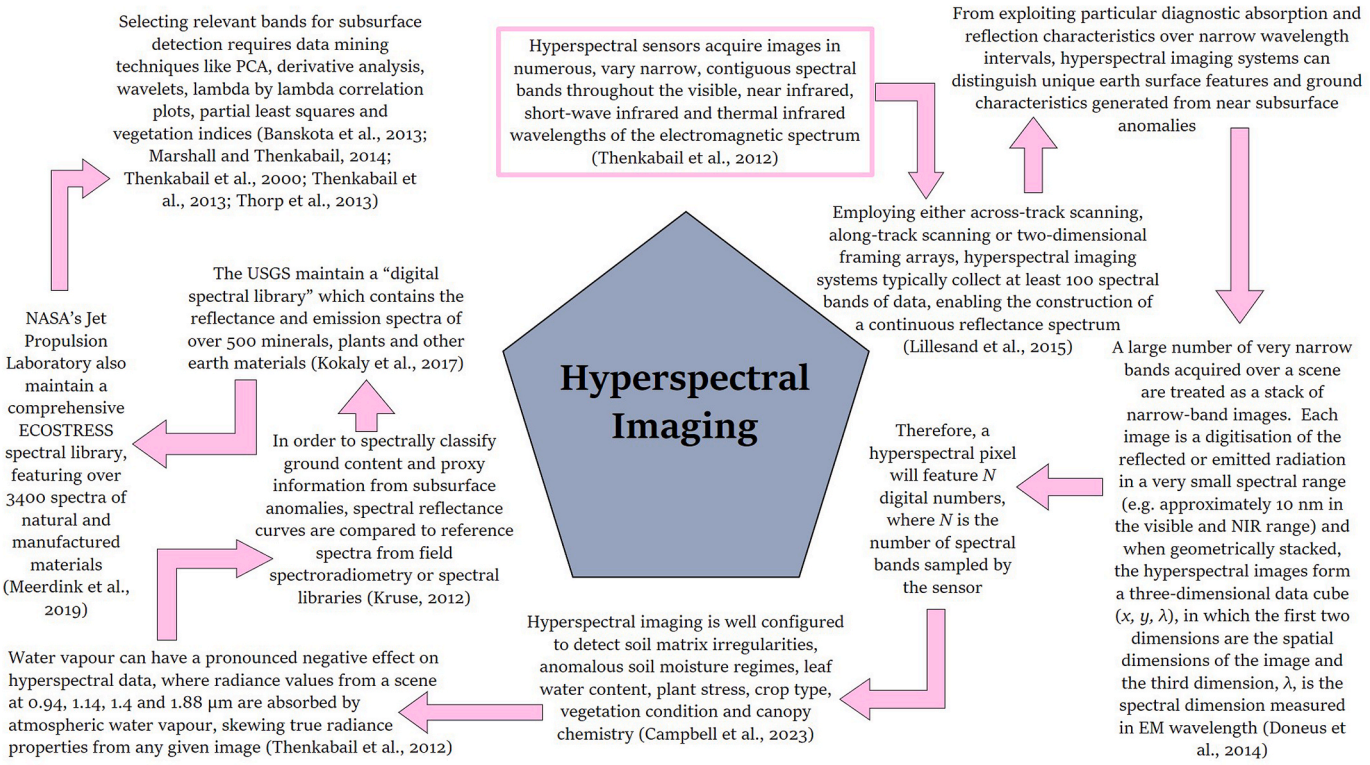

Fig. D4. Principles of hyperspectral imaging. Pink box denotes beginning of flow graphic and pink arrows depict flow of information.

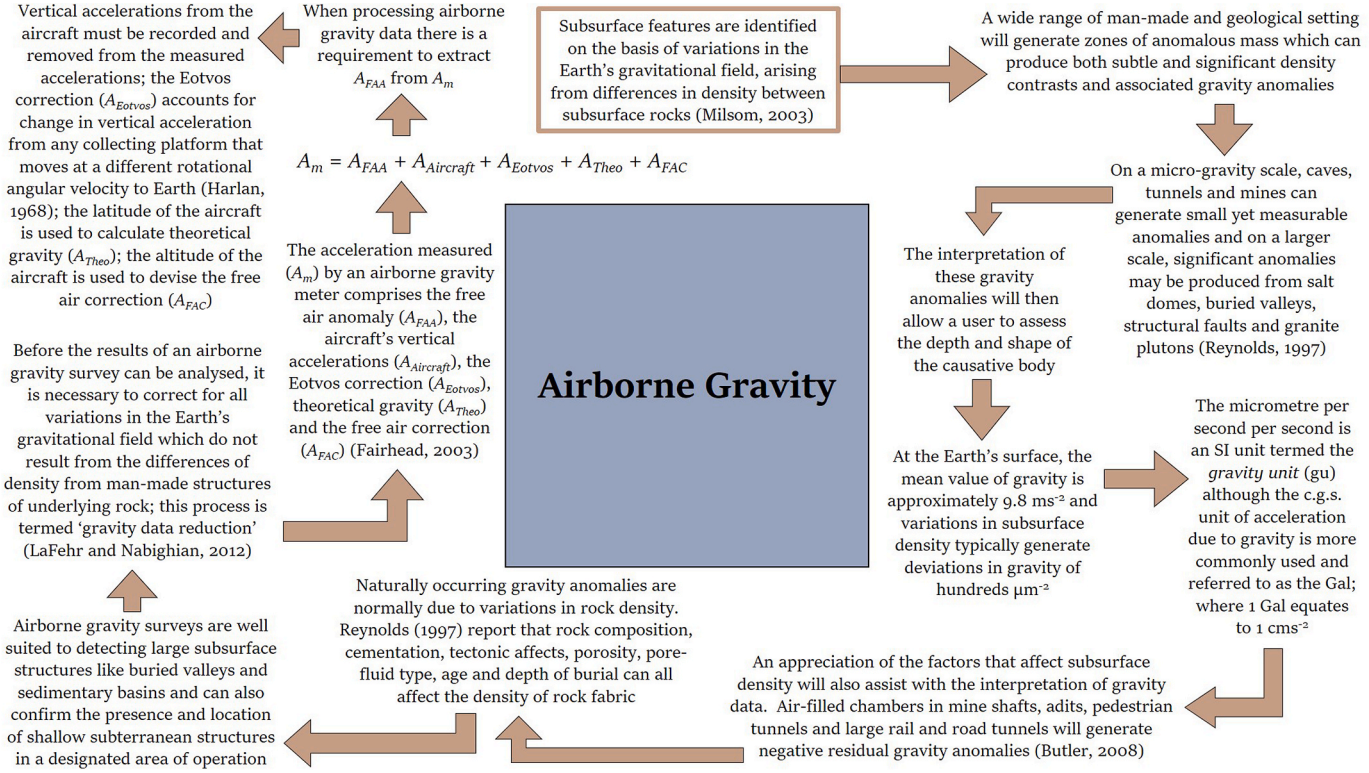

Fig. D5. Principles of airborne gravity. Brown box denotes beginning of flow graphic and brown arrows depict flow of information.

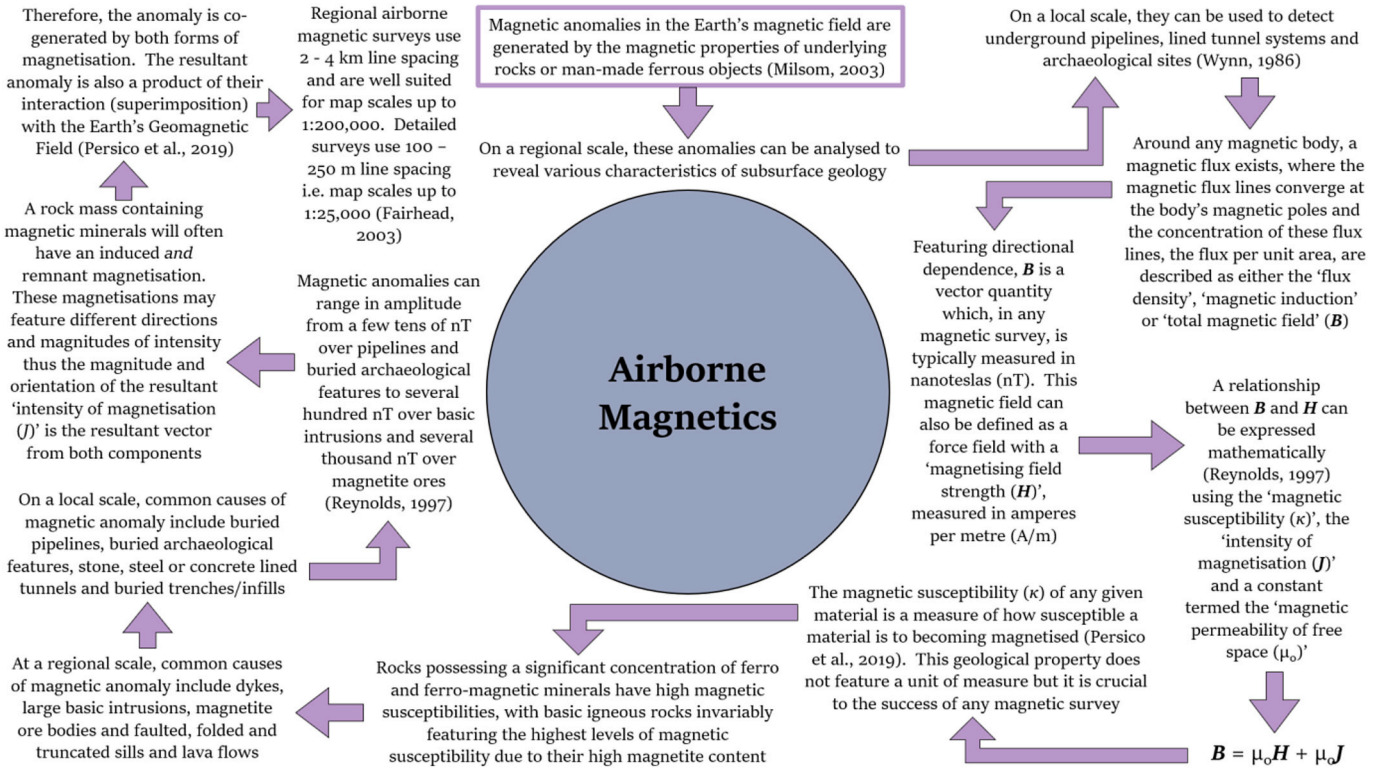

Fig. D6. Principles of airborne magnetics. Purple box denotes beginning of flow graphic and purple arrows depict flow of information.

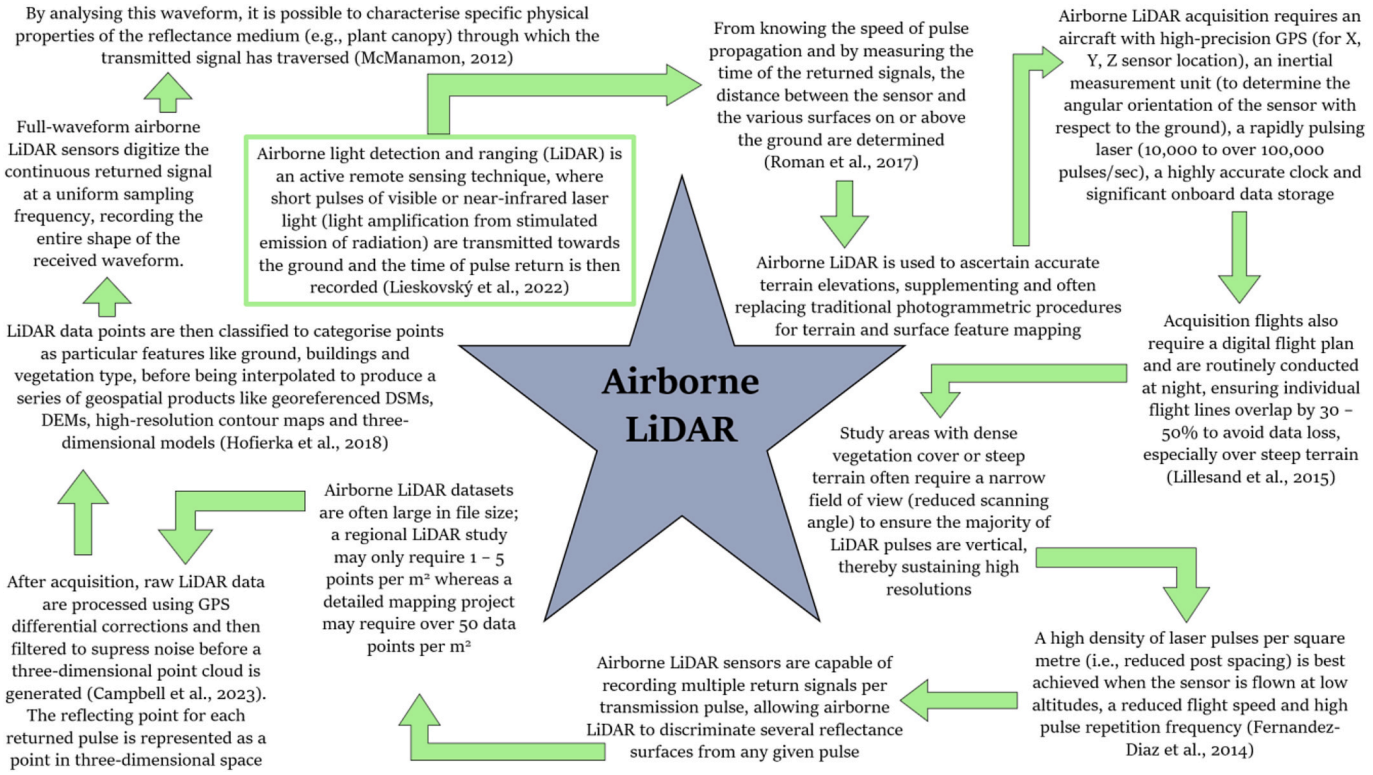

Fig. D7. Principles of airborne LiDAR. Light green box denotes beginning of flow graphic and light green arrows depict flow of information.

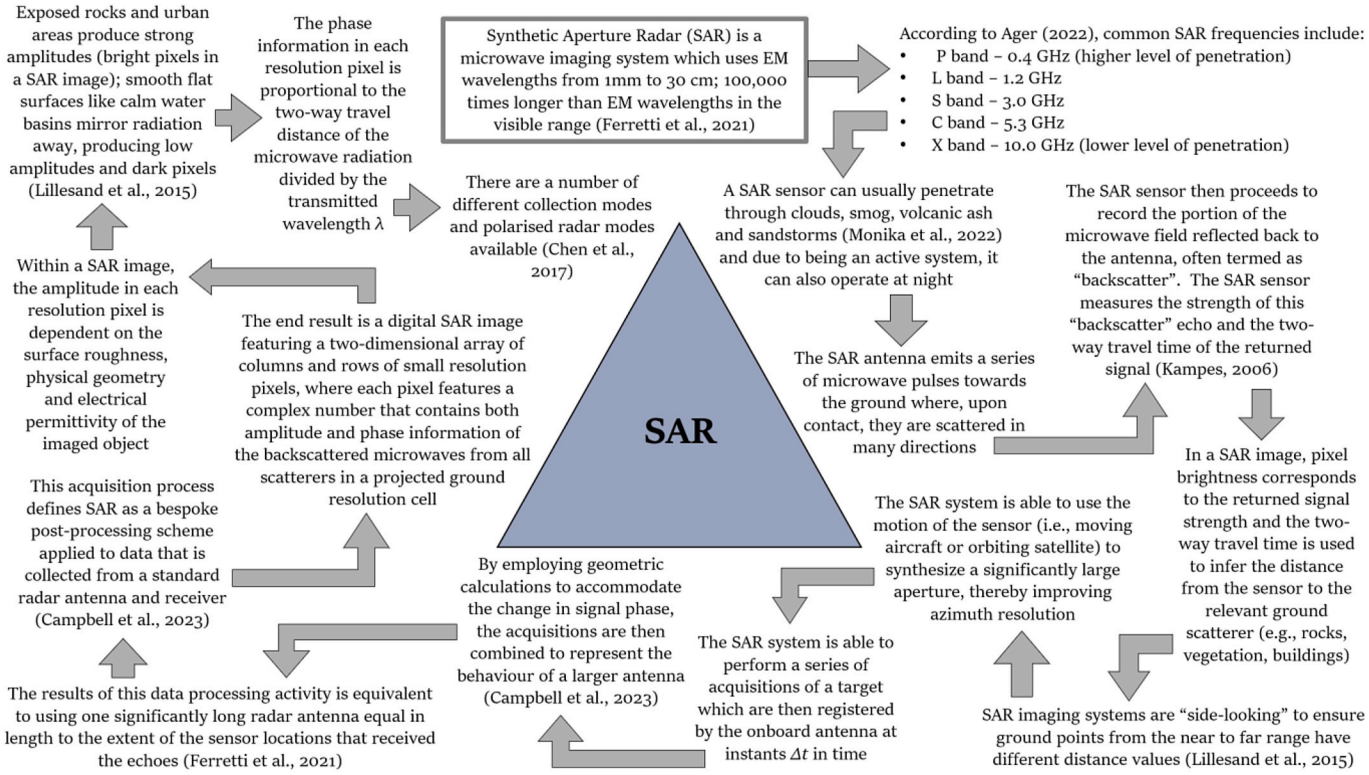

Fig. D8. Principles of synthetic aperture radar (SAR). Grey box denotes beginning of flow graphic and grey arrows depict flow of information.

Data availability

No data was used for the research described in the article.

References

Abdel Zaher, M., Saibi, H., Mansour, K., Khalil, A., Soliman, M., 2018. Geothermal exploration using airborne gravity and magnetic data at Siwa Oasis, Western Desert, Egypt. Renew. Sustain. Energy Rev. 82, 3824–3832. https://doi.org/10.1016/j.rser.2017.10.088.

Abdel-Hardy, M., 1970. Subsurface drainage mapping by airborne infrared imagery techniques. In: Proceedings of the Oklahoma Academy of Science, pp. 10–18.

Abuzied, S.M., Kaiser, M.F., Shendi, E.-A.H., Abdel-Fattah, M.I., 2020. Multi-criteria decision support for geothermal resources exploration based on remote sensing, GIS and geophysical techniques along the Gulf of Suez coastal area, Egypt. Geothermics 88, 101893. https://doi.org/10.1016/j.geothermics.2020.101893.

Achmon, M., Ben-Avraham, Z., 1997. The deep structure of the Carmel fault zone, northern Israel, from gravity field analysis. Tectonics 16, 563–569. https://doi.org/10.1029/96TC02912.

Agapiou, A., Hadjimitsis, D.G., Sarris, A., Georgopoulos, A., Alexakis, D.D., 2013a. Optimum temporal and spectral window for monitoring crop marks over archaeological remains in the Mediterranean region. J. Archaeol. Sci. 40, 1479–1492. https://doi.org/10.1016/j.jas.2012.10.036.

Agapiou, A., Alexakis, D., Sarris, A., Hadjimitsis, D., 2013b. Orthogonal equations of multi-spectral satellite imagery for the identification of un-excavated archaeological sites. Remote Sens 5, 6560–6586. https://doi.org/10.3390/rs5126560.

Agapiou, A., Hadjimitsis, D., Sarris, A., Themistocleous, K., Papadavid, G., 2010. Hyperspectral ground truth data for the detection of buried architectural remains. In: Ioannides, M., Fellner, D., Georgopoulos, A., Hadjimitsis, D.G. (Eds.), Digital Heritage, Lecture Notes in Computer Science. Springer, Berlin Heidelberg, Berlin, Heidelberg, pp. 318–331. https://doi.org/10.1007/978-3-642-16873-4_24.

Airbus, 2022. Using Synthetic Aperture Radar (SAR) to detect objects and dark vessels. Air and Space Remote Sensing of the Subsurface dated 29 November, 2022.

Alberti, S., Ferretti, A., Leoni, G., Margottini, C., Spizzichino, D., 2017. Surface deformation data in the archaeological site of Petra from medium-resolution satellite radar images and SqueeSAR™ algorithm. J. Cult. Herit. 25, 10–20. https://doi.org/10.1016/j.culher.2017.01.005.

Alexakis, D., Sarris, A., Astaras, T., Albanakis, K., 2009. Detection of neolithic settlements in thessaly (Greece) through multispectral and hyperspectral satellite imagery. Sensors 9, 1167–1187. https://doi.org/10.3390/s90201167.

Aljammaz, A., Sultan, M., Izadi, M., Abotalib, A.Z., Elhebiry, M.S., Emil, M.K., Abdelmohsen, K., Saleh, M., Becker, R., 2021. Land subsidence induced by rapid urbanization in arid environments: a remote sensing-based investigation. Remote Sens 13, 1109. https://doi.org/10.3390/rs13061109.

Allbed, A., Kumar, L., 2013. Soil salinity mapping and monitoring in arid and semi-arid regions using remote sensing technology: a review. Adv. Remote Sens. 2, 373–385. https://doi.org/10.4236/ars.2013.24040.

Ammirati, L., Mondillo, N., Rodas, R.A., Sellers, C., Di Martire, D., 2020. Monitoring land surface deformation associated with gold artisanal mining in the Zaruma city (Ecuador). Remote Sens 12, 2135. https://doi.org/10.3390/rs12132135.

Anantrasirichai, N., Biggs, J., Kelevitz, K., Sadeghi, Z., Wright, T., Thompson, J., Achim, A.M., Bull, D., 2021. Detecting ground deformation in the built environment using sparse satellite InSAR data with a convolutional neural network. IEEE Trans. Geosci. Rem. Sens. 59, 2940–2950. https://doi.org/10.1109/TGRS.2020.3018315.

Barla, G., Tamburini, A., Del Conte, S., Giannico, C., 2016. InSAR monitoring of tunnel induced ground movements. Geomech. Tunn. 9, 15–22. https://doi.org/10.1002/geot.201500052.

Bassani, C., Cavalli, R.M., Goffredo, R., Palombo, A., Pascucci, S., Pignatti, S., 2009. Specific spectral bands for different land cover contexts to improve the efficiency of remote sensing archaeological prospection: the Arpi case study. J. Cult. Herit., ICT and Remote sensing for Cultural Resource Management and Documentation 10, e41–e48. https://doi.org/10.1016/j.culher.2009.09.002.

Beltrão, J.F., Silva, J.B.C., Costa, J.C., 1991. Robust polynomial fitting method for regional gravity estimation. Geophysics 56, 80–89. https://doi.org/10.1190/1.1442960.

Bennett, R., Welham, K., Hill, R.A., Ford, A., 2010. Making the most of airborne remote sensing techniques for archaeological survey and interpretation (EAC Occasional Paper No. 5), Remote Sensing for Archaeological Heritage Management. 11th EAC Heritage Management Symposium. Reykjavik, Iceland.

Bennett, R., Welham, K., Hill, R.A., Ford, A.L.J., 2012. The application of vegetation indices for the prospection of archaeological features in grass-dominated environments: application of vegetation indices in grass-dominated environments. Archaeol. Prospect. 19, 209–218. https://doi.org/10.1002/arp.1429.

Berezowski, V., Mallett, X., Ellis, J., Moffat, I., 2021. Using ground penetrating radar and resistivity methods to locate unmarked graves: a review. Remote Sens 13, 2880. https://doi.org/10.3390/rs13152880.

Berger, Z., 1994. Satellite Hydrocarbon Exploration: Interpretation and Integration Techniques. Spinger-Verlag, Berlin.

Bernatek-Jakiel, A., Jakiel, M., 2021. Identification of soil piping-related depressions using an airborne LiDAR DEM: role of land use changes. Geomorphology 378, 107591. https://doi.org/10.1016/j.geomorph.2020.107591.

Bewley, R.H., 2003. Aerial survey for archaeology: aerial survey for archaeology. Photogramm. Rec. 18, 273–292. https://doi.org/10.1046/j.0031-868X.2003.00023.x.

Biondi, F., 2022. Scanning inside volcanoes with synthetic aperture radar echography tomographic Doppler imaging. Remote Sens 14, 3828. https://doi.org/10.3390/rs14153828.

Biondi, F., Malanga, C., 2022. Synthetic aperture radar Doppler tomography reveals details of undiscovered high-resolution internal structure of the Great pyramid of giza. Remote Sens 14, 5231. https://doi.org/10.3390/rs14205231.

Bonì, R., Meisina, C., Cigna, F., Herrera, G., Notti, D., Bricker, S., McCormack, H., Tomás, R., Béjar-Pizarro, M., Mulas, J., Ezquerro, P., 2017. Exploitation of satellite A-DInSAR time series for detection, characterization and modelling of land subsidence. Geosciences 7, 1–23. https://doi.org/10.3390/geosciences7020025.

Braitenberg, C., Sampietro, D., Pivetta, T., Zuliani, D., Barbagallo, A., Fabris, P., Rossi, L., Fabbri, J., Mansi, A.H., 2016. Gravity for detecting caves: airborne and terrestrial simulations based on a comprehensive karstic cave benchmark. Pure Appl. Geophys. 173, 1243–1264. https://doi.org/10.1007/s00024-015-1182-y.

Bubenzer, O., Bolten, A., 2008. The use of new elevation data (SRTM/ASTER) for the detection and morphometric quantification of Pleistocene megadunes (draa) in the eastern Sahara and the southern Namib. Geomorphology 102, 221–231. https://doi.org/10.1016/j.geomorph.2008.05.003.

Butcher, A., Murphy, P.J., Beaney, S., Clark, R., 2006. The search for palmer's chamber, Lamb leer, Somerset, United Kingdom. Cave Karst Sci. 33, 101–104.

Butler, D.K., 2008. Detection and characterization of subsurface cavities, tunnels and abandoned mines. -Surf. Geophys. Hum. Act 578–584.

Calleja, J.F., Requejo Pagés, O., Díaz-Álvarez, N., Peón, J., Gutiérrez, N., Martín-Hernández, E., Cebada Relea, A., Rubio Melendi, D., Fernández Álvarez, P., 2018. Detection of buried archaeological remains with the combined use of satellite multispectral data and UAV data. Int. J. Appl. Earth Obs. Geoinformation 73, 555–573. https://doi.org/10.1016/j.jag.2018.07.023.

Campbell, W.H., 2003. Introduction to Geomagnetic Fields, 2nd. Cambridge University Press, Cambridge ; New York.

Carrer, L., Castelletti, D., Pozzobon, R., Sauro, F., Bruzzone, L., 2015. A novel method for hidden natural caves characterization and accessibility assessment from spaceborne VHR SAR images. IEEE Trans. Geosci. Rem. Sens. 14, 1–11. https://doi.org/10.1109/TGRS.2022.3222991.

Casana, J., Kantner, J., Wiewel, A., Cothren, J., 2014. Archaeological aerial thermography: a case study at the Chaco-era Blue J community, New Mexico. J. Archaeol. Sci. 45, 207–219. https://doi.org/10.1016/j.jas.2014.02.015.

Casana, J., Wiewel, A., Cool, A., Hill, A.C., Fisher, K.D., Laugier, E.J., 2017. Archaeological aerial thermography in theory and practice. Adv. Archaeol. Pract. 5, 310–327. https://doi.org/10.1017/aap.2017.23.

Cavalli, R.M., Pascucci, S., Pignatti, S., 2009. Optimal spectral domain selection for maximizing archaeological signatures: Italy case studies. Sensors 9, 1754–1767. https://doi.org/10.3390/s90301754.

Cerra, D., Agapiou, A., Cavalli, R., Sarris, A., 2018. An objective assessment of hyperspectral indicators for the detection of buried archaeological relics. Remote Sens 10, 500. https://doi.org/10.3390/rs10040500.

Challis, K., Carey, C., Kincey, M., Howard, A.J., 2011. Airborne lidar intensity and geoarchaeological prospection in river valley floors. Archaeol. Prospect. 18, 1–13. https://doi.org/10.1002/arp.398.

Challis, K., Kincey, M., Howard, A.J., 2008. Airborne remote sensing of aggregate landscapes. Trent Val. Geoarchaeology.

Chase, A.S.Z., Chase, D.Z., Chase, A.F., 2017. LiDAR for archaeological research and the study of historical landscapes. In: Masini, N., Soldovieri, F. (Eds.), Sensing the Past, Geotechnologies and the Environment. Springer International Publishing, Cham, pp. 89–100. https://doi.org/10.1007/978-3-319-50518-3_4.

Chen, F., Lasaponara, R., Masini, N., 2017. An overview of satellite synthetic aperture radar remote sensing in archaeology: from site detection to monitoring. J. Cult. Herit. 23, 5–11. https://doi.org/10.1016/j.culher.2015.05.003.

Chen, F., Masini, N., Liu, J., You, J., Lasaponara, R., 2016. Multi-frequency satellite radar imaging of cultural heritage: the case studies of the yumen frontier pass and niya ruins in the western regions of the silk road corridor. Int. J. Digit. Earth 9, 1224–1241. https://doi.org/10.1080/17538947.2016.1181213.

Chen, F., Masini, N., Yang, R., Milillo, P., Feng, D., Lasaponara, R., 2014. A space view of radar archaeological marks: first applications of COSMO-SkyMed X-band data. Remote Sens 7, 24–50. https://doi.org/10.3390/rs70100024.

Choi, S., Götze, H.-J., Meyer, U., Group, D., 2011. 3-D density modelling of underground structures and spatial distribution of salt diapirism in the Dead Sea Basin: gravity modelling and salt diapirism in the DSB. Geophys. J. Int. 184, 1131–1146. https://doi.org/10.1111/j.1365-246X.2011.04939.x.

Comer, D., Chapman, B., Comer, J., 2017. Detecting landscape disturbance at the nasca lines using SAR data collected from airborne and satellite platforms. Geosciences 7, 106. https://doi.org/10.3390/geosciences7040106.

Cover, T.M., Thomas, J.A., 1991. Elements of information theory. Wiley Series in Telecommunications. Wiley, New York.

Da Lio, C., Tosi, L., 2018. Land subsidence in the Friuli Venezia Giulia coastal plain, Italy: 1992–2010 results from SAR-based interferometry. Sci. Total Environ. 633, 752–764. https://doi.org/10.1016/j.scitotenv.2018.03.244.

Dana Negula, I., Moise, C., Lazăr, A.M., Rişcuţa, N.C., Cristescu, C., Dedulescu, A.L., Mihalache, C.E., Badea, A., 2020. Satellite remote sensing for the analysis of the Micia and Germisara archaeological sites. Remote Sens 12, 2003. https://doi.org/10.3390/rs12122003.

Dao, M., Kwan, C., Koperski, K., Marchisio, G., 2017. A joint sparsity approach to tunnel activity monitoring using high resolution satellite images. 2017 IEEE 8th Annual Ubiquitous Computing, Electronics and Mobile Communication Conference (UEMCON), pp. 322–328. https://doi.org/10.1109/UEMCON.2017.8249061. IEEE, New York City, NY.

Davis, D.S., 2019. Object-based image analysis: a review of developments and future directions of automated feature detection in landscape archaeology. Archaeol. Prospect. 26, 155–163. https://doi.org/10.1002/arp.1730.

Del Grande, N.K., 2009. Thermal inertia contrast detection of subsurface structures. Thermosense XXXI. SPIE. 7299, 115–121. https://doi.org/10.1117/12.829407.

Deng, B., Guo, H.D., Wang, C.L., Nie, Y.P., 2010. Applications of remote sensing technique in archaeology: a review. J. Remote Sens. 14, 187–196.

Deng, W., Wang, K., Liu, X., Zhang, T., Liu, H., Liu, J., 2022. Research on remote sensing detection method for distributed subsurface targets inside mountain bodies. In: 2022 International Conference on Artificial Intelligence and Computer Information Technology (AICIT). Presented at the 2022 International Conference on Artificial Intelligence and Computer Information Technology (AICIT). IEEE, pp. 1–6. https://doi.org/10.1109/AICIT55386.2022.9930298. Yichang, China.

Devereux, B.J., Amable, G.S., Crow, P., 2008. Visualisation of LiDAR terrain models for archaeological feature detection. Antiquity 82, 470–479. https://doi.org/10.1017/S0003598X00096952.

Doneus, M., Verhoeven, G., Atzberger, C., Wess, M., Ruš, M., 2014. New ways to extract archaeological information from hyperspectral pixels. J. Archaeol. Sci. 52, 84–96. https://doi.org/10.1016/j.jas.2014.08.023.

Du, X., Sun, D., Li, F., Tong, J., 2022. A study on the propagation trend of underground coal fires based on night-time thermal infrared remote sensing technology. Sustainability 14, 14741. https://doi.org/10.3390/su142214741.

Ekaran, S., 2022. The 5 best 3D scanning apps for iPhone [WWW Document]. MUO. URL. https://www.makeuseof.com/best-3d-scanning-apps-iphone/. (Accessed 1 August 2023).

El-Behaedi, R., 2021. Detection and 3D modeling of potential buried archaeological structures using WorldView-3 satellite imagery. Remote Sens 14, 92. https://doi.org/10.3390/rs14010092.

El-Kelani, R., 2020. A review of gravity and magnetic studies in the Jordan Dead Sea Transform zone. Jordan Journal of Earth and Environmental Sciences 11, 1.

El-Raouf, A.A., Doğru, F., Abdelrahman, K., Fnais, M.S., El Manharawy, A., Amer, O., 2023. Using airborne geophysical and geochemical methods to map structures and their related gold mineralization. Minerals 13, 237. https://doi.org/10.3390/min13020237.

ESA, 2023. Satellite Missions catalogue - eoPortal [WWW Document]. Satell. Missions Cat. URL. https://www.eoportal.org/satellite-missions. (Accessed 1 August 2023).

Everett, M.E., 2013. Near-surface Applied Geophysics. Cambridge University Press, Cambridge ; New York.

Ezersky, M.G., Eppelbaum, L.V., Al-Zoubi, A., Keydar, S., Abueladas, A., Akkawi, E., Medvedev, B., 2013. Geophysical prediction and following development sinkholes in two Dead Sea areas, Israel and Jordan. Environ. Earth Sci. 70, 1463–1478. https://doi.org/10.1007/s12665-013-2233-2.

Fahnestock, J.D., Schowengerdt, R.A., 1983. Spatially variant contrast enhancement using local range modification. Opt. Eng. 22, 378–381. https://doi.org/10.1117/12.7973124.

Fairhead, J.D., Cooper, G.R.J., Sander, S., 2017. Advances in airborne gravity and magnetics. Proc. Explor. 17, 113–127.

Featherstone, R., Horne, P., Macleod, D., Bewley, R., 1999. Aerial reconnaissance over England in summer 1996. with reports by J. Collens and R. Philpott, D. A. Edwards, F. Griffith and W. Horner, S. Hartgroves, P. Markham, D. Motkin, C. R. Musson, F. Radcliffe, D. Strachan, B. Vyner and R. Yarwood Archaeol. Prospect. 6, 47–62. https://doi.org/10.1002/(SICI)1099-0763(199906)6:2<47::AID-ARP113>3.0.CO;2-Y.

Ferretti, A., Passera, E., Capes, R., 2021. End-to-end implementation and operation of the European ground motion service (EGMS): algorithm theoretical basis document. Technical Report EGMS-D3-ALG-SC1-2.0-006.

Finn, M.P., Lewis, M. David, Bosch, D.D., Giraldo, M., Yamamoto, K., Sullivan, D.G., Kincaid, R., Luna, R., Allam, G.K., Kvien, C., Williams, M.S., 2011. Remote sensing of soil moisture using airborne hyperspectral data. GIScience Remote Sens. 48, 522–540. https://doi.org/10.2747/1548-1603.48.4.522.

Freeland, T., Heung, B., Burley, D.V., Clark, G., Knudby, A., 2016. Automated feature extraction for prospection and analysis of monumental earthworks from aerial LiDAR in the Kingdom of Tonga. J. Archaeol. Sci. 69, 64–74. https://doi.org/10.1016/j.jas.2016.04.011.

Gaber, A., Mohamed, A.K., ElGalladi, A., Abdelkareem, M., Beshr, A.M., Koch, M., 2020. Mapping the groundwater potentiality of West Qena area, Egypt, using integrated remote sensing and hydro-geophysical techniques. Remote Sens 12, 1559. https://doi.org/10.3390/rs12101559.

Ghezzi, A., Schettino, A., Pierantoni, P.P., Conyers, L., Tassi, L., Vigliotti, L., Schettino, E., Melfi, M., Gorrini, M.E., Boila, P., 2019. Reconstruction of a segment of the UNESCO world heritage hadrian's villa tunnel network by integrated GPR, magnetic–paleomagnetic, and electric resistivity prospections. Remote Sens 11, 1739. https://doi.org/10.3390/rs11151739.

Ghorbani, Z., Khosravi, A., Maghsoudi, Y., Mojtahedi, F.F., Javadnia, E., Nazari, A., 2022. Use of InSAR data for measuring land subsidence induced by groundwater withdrawal and climate change in Ardabil Plain, Iran. Sci. Rep. 12, 13998. https://doi.org/10.1038/s41598-022-17438-y.

Gitelson, A.A., Merzlyak, M.N., Lichtenthaler, H.K., 1996. Detection of red edge position and chlorophyll content by reflectance measurements near 700 nm. J. Plant Physiol. 148, 501–508. https://doi.org/10.1016/S0176-1617(96)80285-9.

Gonzalez, R.C., Wintz, P., 1987. Image Transforms-Digital Image Processing. Addison-Wesley, N. Y.

Götze, H.-J., El-Kelani, R., Schmidt, S., Rybakov, M., Hassouneh, M., Förster, H.-J., Ebbing, J., 2007. Integrated 3D density modelling and segmentation of the Dead Sea

Transform. Int. J. Earth Sci. 96, 289–302. https://doi.org/10.1007/s00531-006-0095-5.
Götze, H.-J., Meyer, U., Choi, S., 2010. Helicopter gravity survey in the Dead Sea area. Eos Trans. Am. Geophys. Union 91, 109–110. https://doi.org/10.1029/2010EO120002.
Grande, N.K.D., Ascough, B.M., Rumpf, R.L., 2013. Thermal inertia mapping of below ground objects and voids. Detection and Sensing of Mines, Explosive Objects, and Obscured Targets XVIII, 313–322. https://doi.org/10.1117/12.2016144. SPIE.
Grandjean, G., Paillou, P., Dubois-Fernandez, P., August-Bernex, T., Baghdadi, N.N., Achache, J., 2001. Subsurface structures detection by combining L-band polarimetric SAR and GPR data: example of the Pyla Dune (France). IEEE Trans. Geosci. Rem. Sens. 39, 1245–1258. https://doi.org/10.1109/36.927447.
Grauch, V.J.S., 2002. High-Resolution Aeromagnetic Survey to Image Shallow Faults (Open-File Report No. 02–384), Open-File Report. USGS, Prepared for the U.S. Department of Energy.
Gruen, A., 2021. Everything moves: the rapid changes in photogrammetry and remote sensing. Geo-Spat. Inf. Sci. 24, 33–49. https://doi.org/10.1080/10095020.2020.1868275.
Hartshorn, C.A., Isaacson, S.D., Barrowes, B.E., Perren, L.J., Lozano, D., Shubitidze, F., 2022. Analysis of the feasibility of UAS-based EMI sensing for underground utilities detection and mapping. Remote Sens 14, 3973. https://doi.org/10.3390/rs14163973.
Hill, A.C., Laugier, E.J., Casana, J., 2020. Archaeological remote sensing using multi-temporal, drone-acquired thermal and near infrared (NIR) imagery: a case study at the Enfield shaker village, New Hampshire. Remote Sens 12, 690. https://doi.org/10.3390/rs12040690.
Hofierka, J., Gallay, M., Bandura, P., Šašak, J., 2018. Identification of karst sinkholes in a forested karst landscape using airborne laser scanning data and water flow analysis. Geomorphology 308, 265–277. https://doi.org/10.1016/j.geomorph.2018.02.004.
Hool, G.A., Johnson, N.C., 2010. Handbook of Building Construction: Data for Architects, Designing and Constructing Engineers, and Contractors. Nabu Press, New York, USA.
Horler, D.N.H., Dockray, M., Barber, J., 1983. The red edge of plant leaf reflectance. Int. J. Remote Sens. 4, 273–288. https://doi.org/10.1080/01431168308948546.
Jamaludin, S.N.F., Pubellier, M., Sautter, B., 2021. Shallow vs. Deep subsurface structures of central Luconia province, offshore Malaysia reveal by aeromagnetic, airborne gravity and seismic data. Appl. Sci. 11, 5095. https://doi.org/10.3390/app11115095.
James, K., Nichol, C.J., Wade, T., Cowley, D., Gibson Poole, S., Gray, A., Gillespie, J., 2020. Thermal and multispectral remote sensing for the detection and analysis of archaeologically induced crop stress at a UK site. Drones 4, 61. https://doi.org/10.3390/drones4040061.
James, L.A., Hodgson, M.E., Ghoshal, S., Latiolais, M.M., 2012. Geomorphic change detection using historic maps and DEM differencing: the temporal dimension of geospatial analysis. Geomorphology 137, 181–198. https://doi.org/10.1016/j.geomorph.2010.10.039.
Jia, J., Wang, Y., Chen, J., Guo, R., Shu, R., Wang, J., 2020. Status and application of advanced airborne hyperspectral imaging technology: a review. Infrared Phys. Technol. 104, 103115. https://doi.org/10.1016/j.infrared.2019.103115.
Kalayci, T., Simon, F.-X., Sarris, A., 2017. A manifold approach for the investigation of early and middle neolithic settlements in thessaly, Greece. Geosciences 7, 79. https://doi.org/10.3390/geosciences7030079.
Kalderis, D., Juhasz, A.L., Boopathy, R., Comfort, S., 2011. Soils contaminated with explosives: environmental fate and evaluation of state-of-the-art remediation processes (IUPAC Technical Report). Pure Appl. Chem. 83, 1407–1484. https://doi.org/10.1351/PAC-REP-10-01-05.
Kearey, P., Brooks, M., Hill, I., 2002. An Introduction to Geophysical Exploration, third ed. Blackwell Science, Malden, MA.
Keller, S., Riese, F.M., Allroggen, N., Jackisch, C., Hinz, S., 2018. Modeling Subsurface Soil Moisture Based on Hyperspectral Data - First Results of a Multilateral Field Campaign 15.
Kennedy, D., 1998. Declassified satellite photographs and archaeology in the Middle East: case studies from Turkey. Antiquity 72, 553–561. https://doi.org/10.1017/S0003598X0008697X.
Kharbish, S., Eldosouky, A.M., Amer, O., 2022. Integrating mineralogy, geochemistry and aeromagnetic data for detecting Fe–Ti ore deposits bearing layered mafic intrusion, Akab El-Negum, Eastern Desert, Egypt. Sci. Rep. 12, 15474. https://doi.org/10.1038/s41598-022-19760-x.
Konsolaki, A., Vassilakis, E., Kotsi, E., Kontostavlos, G., Lekkas, E., Stavropoulou, M., Giannopoulos, I., 2022. Introducing interdisciplinary innovative techniques for mapping karstic caves. Presented at the 16 Th International Congress of the Geological Society of Greece, Bulletin of the Geological Society of Greece, Patras, Greece, p. 2.
Křivánek, R., 2017. Comparison study to the use of geophysical methods at archaeological sites observed by various remote sensing techniques in the Czech republic. Geosciences 7, 81. https://doi.org/10.3390/geosciences7030081.
Kucukkaya, A.G., 2004. Photogrammetry and remote sensing in archeology. J. Quant. Spectrosc. Radiat. Transf. 88, 83–88. https://doi.org/10.1016/j.jqsrt.2003.12.030.
Kuzia, K., 2018. Utilisation of airborne laser scanning for monitoring of secondary impacts of underground mining exploitation. Q. Environ. Eng. Des. 172, 4–10.
Kwan, C., 2019. Methods and challenges using multispectral and hyperspectral images for practical change detection applications. Information 10, 353. https://doi.org/10.3390/info10110353.
Kwan, C., 2018. Remote sensing performance enhancement in hyperspectral images. Sensors 18, 3598. https://doi.org/10.3390/s18113598.
LaFehr, T.R., Nabighian, M.N., 2012. Fundamentals of Gravity Exploration. Society of Exploration Geophysicists.
Lasaponara, R., Leucci, G., Masini, N., Persico, R., Scardozzi, G., 2016. Towards an operative use of remote sensing for exploring the past using satellite data: the case study of Hierapolis (Turkey). Remote Sens. Environ. 174, 148–164. https://doi.org/10.1016/j.rse.2015.12.016.
Lasaponara, R., Masini, N., 2018. Space-based identification of archaeological illegal excavations and a new automatic method for looting feature extraction in Desert areas. Surv. Geophys. 39, 1323–1346. https://doi.org/10.1007/s10712-018-9480-4.
Lasaponara, R., Masini, N., 2014. Beyond modern landscape features: new insights in the archaeological area of Tiwanaku in Bolivia from satellite data. Int. J. Appl. Earth Obs. Geoinformation 26, 464–471. https://doi.org/10.1016/j.jag.2013.09.006.
Lasaponara, R., Masini, N., 2009. Full-waveform Airborne Laser Scanning for the detection of medieval archaeological microtopographic relief. J. Cult. Herit. 10, e78–e82. https://doi.org/10.1016/j.culher.2009.10.004.
Lasaponara, R., Masini, N., 2007. Detection of archaeological crop marks by using satellite QuickBird multispectral imagery. J. Archaeol. Sci. 34, 214–221. https://doi.org/10.1016/j.jas.2006.04.014.
Li, X., Yuan, Z., Wang, Q., 2019. Unsupervised deep noise modeling for hyperspectral image change detection. Remote Sens 11, 258. https://doi.org/10.3390/rs11030258.
Lieskovský, J., Lieskovský, T., Hladíková, K., Štefunková, D., Hurajtová, N., 2022. Potential of airborne LiDAR data in detecting cultural landscape features in Slovakia. Landsc. Res. 47, 539–558. https://doi.org/10.1080/01426397.2022.2045923.
Lillesand, T.M., Kiefer, R.W., Chipman, J.W., 2015. Remote Sensing and Image Interpretation, seventh ed. John Wiley & Sons, Inc, Hoboken, N.J.
Lin, A.Y.-M., Novo, A., Har-Noy, S., Ricklin, N.D., Stamatiou, K., 2011. Combining GeoEye-1 satellite remote sensing, UAV aerial imaging, and geophysical surveys in anomaly detection applied to archaeology. IEEE J. Sel. Top. Appl. Earth Obs. Remote Sens. 4, 870–876. https://doi.org/10.1109/JSTARS.2011.2143696.
Luo, L., Wang, X., Guo, H., Lasaponara, R., Zong, X., Masini, N., Wang, G., Shi, P., Khatteli, H., Chen, F., Tariq, S., Shao, J., Bachagha, N., Yang, R., Yao, Y., 2019. Airborne and spaceborne remote sensing for archaeological and cultural heritage applications: a review of the century (1907–2017). Remote Sens. Environ. 232, 111280. https://doi.org/10.1016/j.rse.2019.111280.
Luo, L., Wang, X., Liu, J., Guo, H., Zong, X., Ji, W., Cao, H., 2017. VHR GeoEye-1 imagery reveals an ancient water landscape at the Longcheng site, northern Chaohu Lake Basin (China). Int. J. Digit. Earth 10, 139–154. https://doi.org/10.1080/17538947.2016.1214983.
Lv, Y., Jiang, Y., Hu, W., Cao, M., Mao, Y., 2020. A review of the effects of tunnel excavation on the hydrology, ecology, and environment in karst areas: current status, challenges, and perspectives. J. Hydrol. 586, 124891. https://doi.org/10.1016/j.jhydrol.2020.124891.
Macchiarulo, V., Milillo, P., DeJong, M.J., González Martí, J., Sánchez, J., Giardina, G., 2021. Integrated InSAR monitoring and structural assessment of tunnelling-induced building deformations. Struct. Control Health Monit. 28, 1–26. https://doi.org/10.1002/stc.2781.
Mahajan, P.K., Venkatramaiah, S., Shaktawal, K.S., Ganju, J.L., 1984. Geomorphological evolution of Indian coast with spectial reference to hydrocarbon prospects. Unpubl. Rep. 85.
Mathew, S., MacBeth, C., Stevanovic, J., Mangriotis, M.-D., 2023. Detection of dynamic phenomena associated with underground nuclear explosion using multiple seismic surveys and machine learning. Pure Appl. Geophys. 180, 1287–1301. https://doi.org/10.1007/s00024-022-03145-2.
McFee, J.E., Achal, S., Ivanco, T., Anger, C., 2005. A short wave infrared hyperspectral imager for landmine detection. Detection and Remediation Technologies for Mines and Minelike Targets X. Presented at the Detection and Remediation Technologies for Mines and Minelike Targets X, 56–67. https://doi.org/10.1117/12.602637. SPIE.
Melillos, G., Agapiou, A., Themistocleous, K., Michaelides, S., Papadavid, G., Hadjimitsis, D.G., 2019. Field spectroscopy for the detection of underground military structures. Eur. J. Remote Sens. 52, 385–399. https://doi.org/10.1080/22797254.2019.1625075.
Meng, X., Currit, N., Zhao, K., 2010. Ground filtering algorithms for airborne LiDAR data: a review of critical issues. Remote Sens 2, 833–860. https://doi.org/10.3390/rs2030833.
Mi, J., Yang, Y., Zhang, S., An, S., Hou, H., Hua, Y., Chen, F., 2019. Tracking the land use/land cover change in an area with underground mining and reforestation via continuous Landsat classification. Remote Sens 11, 1719. https://doi.org/10.3390/rs11141719.
Milsom, J., 2003. Field geophysics. The Geological Field Guide Series, third ed. J. Wiley, Chichester, West Sussex, England ; Hoboken, NJ.
Milton, E.J., Schaepman, M.E., Anderson, K., Kneubühler, M., Fox, N., 2009. Progress in field spectroscopy. Remote Sens. Environ. 113, S92–S109. https://doi.org/10.1016/j.rse.2007.08.001.
Mitra, D.S., Agarwal, R.P., 1991. Geomorphology and petroleum prospects of cauvery basin, tamilnadu, based on interpretation of Indian remote sensing satellite (IRS) data. J. Indian Soc. Remote Sens. 19, 263–268. https://doi.org/10.1007/BF03023973.
Moriarty, C., Cowley, D.C., Wade, T., Nichol, C.J., 2019. Deploying multispectral remote sensing for multi-temporal analysis of archaeological crop stress at Ravenshall, Fife, Scotland. Archaeol. Prospect. 26, 33–46. https://doi.org/10.1002/arp.1721.
Morley, A., 2011. Exploring the Use of High Resolution Multispectral Satellite Imagery to Identify Subsurface Structures (MSc Thesis). Royal School of Military Survey, Defence Intelligence Security Centre, UK. Cranfield University.
Moyes, H., Montgomery, S., 2019. Locating cave entrances using lidar-derived local relief modeling. Geosciences 9, 98. https://doi.org/10.3390/geosciences9020098.
Murphy, C.A., 2004. The Air-FTG airborne gravity gradiometer system. Airborne Gravity 7–14.

Murphy, C.A., Brewster, J., 2007. Target delineation using full tensor gravity Gradiometry data. ASEG Ext. Abstr. 2007, 1–3. https://doi.org/10.1071/ASEG2007ab096.

Ng, A., Wang, H., Dai, Y., Pagli, C., Chen, W., Ge, L., Du, Z., Zhang, K., 2018. InSAR reveals land deformation at guangzhou and foshan, China between 2011 and 2017 with COSMO-SkyMed data. Remote Sens 10, 813. https://doi.org/10.3390/rs10060813.

Nicholson, P.T., Shaw, I. (Eds.), 2009. Ancient Egyptian Materials and Technology. Cambridge University Press, Cambridge ; UK.

Nsanziyera, A., Rhinane, H., Oujaa, A., Mubea, K., 2018. GIS and remote-sensing application in archaeological site mapping in the awsard area (Morocco). Geosciences 8, 207. https://doi.org/10.3390/geosciences8060207.

Olson, K.R., Speidel, D.R., 2020. Review and analysis: successful use of soil tunnels in medieval and modern warfare and smuggling. Open J. Soil Sci. 10, 194–215. https://doi.org/10.4236/ojss.2020.105010.

Omali, T.U., 2021. Utilization of remote sensing and GIS in geology and mining. Int. J. Sci. Res. Multidiscip. Stud. 7, 17–24.

Ottesen, D., Stewart, M., Brönner, M., Batchelor, C.L., 2020. Tunnel valleys of the central and northern North Sea (56°N to 62°N): distribution and characteristics. Mar. Geol. 425, 106199. https://doi.org/10.1016/j.margeo.2020.106199.

Pascucci, S., Cavalli, R.M., Palombo, A., Pignatti, S., 2010. Suitability of CASI and ATM airborne remote sensing data for archaeological subsurface structure detection under different land cover: the Arpi case study (Italy). J. Geophys. Eng. 7, 183–189. https://doi.org/10.1088/1742-2132/7/2/S04.

Patruno, J., Dore, N., Crespi, M., Pottier, E., 2013. Polarimetric multifrequency and multi-incidence SAR sensors analysis for archaeological purposes: the UNESCO sites of djebel barkal and samarra. Archaeol. Prospect. 20, 89–96. https://doi.org/10.1002/arp.1448.

Perez, D., Banerjee, D., Kwan, C., Dao, M., Shen, Y., Koperski, K., Marchisio, G., Li, J., 2017. Deep learning for effective detection of excavated soil related to illegal tunnel activities. In: 2017 IEEE 8th Annual Ubiquitous Computing, Electronics and Mobile Communication Conference (UEMCON). IEEE, New York City, NY, pp. 626–632. https://doi.org/10.1109/UEMCON.2017.8249062.

Persico, R., Piro, S., Linford, N. (Eds.), 2019. Innovation in Near-Surface Geophysics: Instrumentation, Application, and Data Processing Methods. Elsevier, Amsterdam, Netherlands ; Cambridge, MA.

Pisani, L., De Waele, J., 2021. Candidate cave entrances in a planetary analogue evaporite karst (Cordillera de la Sal, Chile): A remote sensing approach and ground-truth reconnaissance. Geomorphology 389, 107851. https://doi.org/10.1016/j.geomorph.2021.107851.

Pratt, W.K., 1991. Digital Image Processing. john wiley & sons. Inc, N. Y.

Ramirez, R.A., Lee, G.-J., Choi, S.-K., Kwon, T.-H., Kim, Y.-C., Ryu, H.-H., Kim, S., Bae, B., Hyun, C., 2022. Monitoring of construction-induced urban ground deformations using Sentinel-1 PS-InSAR: the case study of tunneling in Dangjin, Korea. Int. J. Appl. Earth Obs. Geoinformation 108, 102721. https://doi.org/10.1016/j.jag.2022.102721.

Reynolds, J.M., 1997. An Introduction to Applied and Environmental Geophysics. John Wiley, Chichester ; New York.

Richemond-Barak, D., 2018. Underground Warfare. Oxford University Press, New York, NY.

Roman, A., Ursu, T.-M., Lăzărescu, V.-A., Opreanu, C.H., Fărcaş, S., 2017. Visualization techniques for an airborne laser scanning-derived digital terrain model in forested steep terrain: detecting archaeological remains in the subsurface. Geoarchaeology 32, 549–562. https://doi.org/10.1002/gea.21621.

Rowlands, A., Sarris, A., 2007. Detection of exposed and subsurface archaeological remains using multi-sensor remote sensing. J. Archaeol. Sci. 34, 795–803. https://doi.org/10.1016/j.jas.2006.06.018.

Sabins, F.F., 1997. Remote Sensing: Principles and Interpretation, third ed. W.H. Freeman and Co, New York.

Saha, S.K., 2022. Remote sensing and geographic information system applications in hydrocarbon exploration: a review. J. Indian Soc. Remote Sens. 50, 1457–1475. https://doi.org/10.1007/s12524-022-01540-9.

Sakuma, A., Yamano, H., 2020. Satellite constellation reveals crop growth patterns and improves mapping accuracy of cropping practices for subtropical small-scale fields in Japan. Remote Sens 12, 2419. https://doi.org/10.3390/rs12152419.

Savage, S.H., Levy, T.E., Jones, I.W., 2012. Prospects and problems in the use of hyperspectral imagery for archaeological remote sensing: a case study from the Faynan copper mining district, Jordan. J. Archaeol. Sci. 39, 407–420. https://doi.org/10.1016/j.jas.2011.09.028.

Scoular, J., Ghail, R., Mason, P., Lawrence, J., Bellhouse, M., Holley, R., Morgan, T., 2020. Retrospective InSAR analysis of east London during the construction of the lee tunnel. Remote Sens 12, 849. https://doi.org/10.3390/rs12050849.

Segev, A., Rybakov, M., 2011. History of faulting and magmatism in the Galilee (Israel) and across the Levant continental margin inferred from potential field data. J. Geodyn. 51, 264–284. https://doi.org/10.1016/j.jog.2010.10.001.

Sharafi, M., Khazaei, S., 2013. Detection of high local groundwater inflow to rock tunnels using ASTER satellite images. Int. Arch. Photogramm. Remote Sens. Spat. Inf. Sci. XL-1/W3, 393–397. https://doi.org/10.5194/isprsarchives-XL-1-W3-393-2013.

Shen, S.S., Roettiger, K.A., 2012. Detection of abandoned mines/caves using airborne LWIR hyperspectral data. In: Shen, S.S., Lewis, P.E. (Eds.), Presented at the SPIE Optical Engineering + Applications, San Diego, California, USA, p. 85150D. https://doi.org/10.1117/12.946113.

Shi, X., Huang, J., Huang, B., 2022. An underground abnormal behavior recognition method based on an optimized alphapose-ST-GCN. J. Circuits Syst. Comput. https://doi.org/10.1142/S0218126622502140.

Shimoni, M., Haelterman, R., Perneel, C., 2019. Hypersectral imaging for military and security applications: combining myriad processing and sensing techniques. IEEE Geosci. Remote Sens. Mag. 7, 101–117. https://doi.org/10.1109/MGRS.2019.2902525.

Shirmard, H., Farahbakhsh, E., Müller, R.D., Chandra, R., 2022. A review of machine learning in processing remote sensing data for mineral exploration. Remote Sens. Environ. 268, 112750. https://doi.org/10.1016/j.rse.2021.112750.

Stott, D., Boyd, D., Beck, A., Cohn, A., 2015. Airborne LiDAR for the detection of archaeological vegetation marks using biomass as a proxy. Remote Sens 7, 1594–1618. https://doi.org/10.3390/rs70201594.

Štular, B., Kokalj, Ž., Oštir, K., Nuninger, L., 2012. Visualization of lidar-derived relief models for detection of archaeological features. J. Archaeol. Sci. 39, 3354–3360. https://doi.org/10.1016/j.jas.2012.05.029.

Sun, H., Zhang, N., Li, D., Liu, S., Ye, Q., 2023. The first semi-airborne transient electromagnetic survey for tunnel investigation in very complex terrain areas. Tunn. Undergr. Space Technol. 132, 104893. https://doi.org/10.1016/j.tust.2022.104893.

Tan, K., Wan, Y., Zhou, X., Song, D., Duan, Q., 2006. The application of remote sensing technology in the archaeological study of the Mausoleum of Emperor Qinshihuang. Int. J. Remote Sens. 27, 3347–3363. https://doi.org/10.1080/01431160600554389.

Tapete, D., Cigna, F., 2019. COSMO-SkyMed SAR for detection and monitoring of archaeological and cultural heritage sites. Remote Sens 11, 1326. https://doi.org/10.3390/rs11111326.

Themistocleous, K., Hadjimitsis, D.G., Melillos, G., 2018. Thermal remote sensing approach combined with field spectroscopy for detecting underground structures intended for defence and security purposes in Cyprus. In: Isaacs, J.C., Bishop, S.S. (Eds.), Detection and Sensing of Mines, Explosive Objects, and Obscured Targets XXIII, p. 1. https://doi.org/10.1117/12.2303835. SPIE, Orlando, United States.

Thenkabail, P.S., Gumma, M.K., Teluguntla, P., Awad, M., Jomaa, I., Arab, F., Zhang, C., Sánchez, N., Piles, M., Martínez-Fernández, J., Vall-llossera, M., Pipia, L., Camps, A., Aguasca, A., Pérez-Aragüés, F., Herrero, C.M., Marshall, M., Thenkabail, P., Saini, M., Christian, B., Joshi, N., Vyas, D., Marpu, P., Nadiminti, K., Aasen, H., Gnyp, M.L., Miao, Y., Bareth, G., Parshakov, I., Coburn, C., Staenz, K., 2014. 697 hyperspectral remote sensing of vegetation and agricultural crops. Photogramm. Eng.

Thompson, J., Marvin, M., Club-Fellow, E., 2005. Experimental research on the use of thermography to locate heat signatures from caves. National Cave and Karst Management Symposium, pp. 102–115.

Trier, Ø.D., Pilø, L.H., 2012. Automatic detection of pit structures in airborne laser scanning data: automatic detection of pits in ALS data. Archaeol. Prospect. 19, 103–121. https://doi.org/10.1002/arp.1421.

Trier, Ø.D., Zortea, M., Tonning, C., 2015. Automatic detection of mound structures in airborne laser scanning data. J. Archaeol. Sci. Rep 2, 69–79. https://doi.org/10.1016/j.jasrep.2015.01.005.

Ulusoy, İ., Labazuy, P., Aydar, E., 2012. STcorr: an IDL code for image based normalization of lapse rate and illumination effects on nighttime TIR imagery. Comput. Geosci. 43, 63–72. https://doi.org/10.1016/j.cageo.2012.02.012.

Ur, J., 2003. CORONA satellite photography and ancient road networks: a northern mesopotamian case study. Antiquity 77, 102–115. https://doi.org/10.1017/S0003598X00061391.

Verhoeven, G., Doneus, M., Atzberger, C., Wes, M., Ruš, M., Pregesbauer, M., Briese, C., 2013. New approaches for archaeological feature extraction of airborne imaging spectroscopy data. In: 10th International Conference on Archaeological Prospection. Austrian Academy of Sciences, pp. 13–15.

Van der Meer, F., Hecker, C., Van Ruitenbeek, F., Van der Werff, H., De Wijkerslooth, C., Wechsler, C., 2014. Geologic remote sensing for geothermal exploration: a review. Int. J. Appl. Earth Obs. Geoinformation 33, 255–269. https://doi.org/10.1016/j.jag.2014.05.007.

Verhoeven, G.J., 2012. Near-infrared aerial crop mark archaeology: from its historical use to current digital implementations. J. Archaeol. Method Theory 19, 132–160. https://doi.org/10.1007/s10816-011-9104-5.

Viezzoli, A., Christiansen, A.V., Auken, E., Sørensen, K., 2008. Quasi-3D modeling of airborne TEM data by spatially constrained inversion. Geophysics 73, F105–F113. https://doi.org/10.1190/1.2895521.

Wang, W., Zhao, W., Huang, L., Vimarlund, V., Wang, Z., 2014. Applications of terrestrial laser scanning for tunnels: a review. J. Traffic Transp. Eng. Engl. Ed. 1, 325–337. https://doi.org/10.1016/S2095-7564(15)30279-8.

Wang, Y., Tian, F., Huang, Y., Wang, J., Wei, C., 2015. Monitoring coal fires in Datong coalfield using multi-source remote sensing data. Trans. Nonferrous Met. Soc. China 25, 3421–3428. https://doi.org/10.1016/S1003-6326(15)63977-2.

Waters, C.N., Graham, C., Tapete, D., Price, S.J., Field, L., Hughes, A.G., Zalasiewicz, J., 2019. Recognizing anthropogenic modification of the subsurface in the geological record. Q. J. Eng. Geol. Hydrogeol. 52, 83–98. https://doi.org/10.1144/qjegh2017-007.

Waters, P., Greenbaum, D., Smart, P.L., Osmaston, H., 1990. Applications of remote sensing to groundwater hydrology. Remote Sens. Rev 4, 223–264. https://doi.org/10.1080/02757259009532107.

Webb, J.E., 1966. The search for iron ore, Eyre Peninsula, South Australia. In: Mining Geophysics Volume 1, Case Histories. Society of Exploration Geophysicists.

Weber, S.A., Yool, S.R., 1999. Detection of subsurface archaeological architecture by computer assisted airphoto interpretation. Geoarchaeology 14, 481–493. https://doi.org/10.1002/(SICI)1520-6548(199908)14:6<481::AID-GEA1>3.0.CO;2-3.

Weishampel, J., Hightower, J., Chase, A., Chase, D., Patrick, R., 2011. Detection and morphologic analysis of potential below-canopy cave openings in the karst landscape around the Maya polity of Caracol using airborne lidar. J. Cave Karst Stud. 73, 187–196. https://doi.org/10.4311/2010EX0179R1.

Wiig, F., Harrower, M., Braun, A., Nathan, S., Lehner, J., Simon, K., Sturm, J., Trinder, J., Dumitru, I., Hensley, S., Clark, T., 2018. Mapping a subsurface water channel with X-band and C-band synthetic aperture radar at the iron age archaeological site of 'Uqdat al-bakrah (safah), Oman. Geosciences 8, 334. https://doi.org/10.3390/geosciences8090334.

Wynne, J.J., Jenness, J., Sonderegger, D.L., Titus, T.N., Jhabvala, M.D., Cabrol, N.A., 2021. Advancing cave detection using terrain analysis and thermal imagery. Remote Sens 13, 3578. https://doi.org/10.3390/rs13183578.

Wynne, J.J., Titus, T.N., Chong Diaz, G., 2008. On developing thermal cave detection techniques for earth, the moon and mars. Earth Planet Sci. Lett. 272, 240–250. https://doi.org/10.1016/j.epsl.2008.04.037.

Xu, X., Li, W., Ran, Q., Du, Q., Gao, L., Zhang, B., 2018. Multisource remote sensing data classification based on convolutional neural network. IEEE Trans. Geosci. Rem. Sens. 56, 937–949. https://doi.org/10.1109/TGRS.2017.2756851.

Yokoyama, R., Shirasawa, M., Pike, R., 2002. Visualizing topography by openness: a new application of image processing to digital elevation models. Photogramm. Eng. Remote Sens. 68, 257–265.

Zahorec, P., Papčo, J., Vajda, P., Szabó, S., 2019. High-precision local gravity survey along planned motorway tunnel in the Slovak Karst. Contrib. Geophys. Geod. 49, 207–227. https://doi.org/10.2478/congeo-2019-0011.

Zakšek, K., Oštir, K., Kokalj, Ž., 2011. Sky-view factor as a relief visualization technique. Remote Sens 3, 398–415. https://doi.org/10.3390/rs3020398.

Zanni, S., De Rosa, A., 2019. Remote sensing analyses on sentinel-2 images: looking for roman roads in srem region (Serbia). Geosciences 9, 25. https://doi.org/10.3390/geosciences9010025.

Zeng, S., Jiang, Y., Wu, Z., Zhang, C., Lv, T., 2023. Declining trees growth and vegetation productivity resulting from decreasing soil water contents induced by tunnels excavation in karst mountain areas. Ecol. Indic. 154, 110555. https://doi.org/10.1016/j.ecolind.2023.110555.

Zhang, T., Zhang, C., Long, D., Wang, Y., Zhou, H., Wang, S., Li, G., Li, H., Zhou, F., Jiang, C., 2023. Application of helicopter-borne and ground–airborne electromagnetic detection to tunnel engineering investigation. Appl. Sci. 13, 1886. https://doi.org/10.3390/app13031886.

Further reading

Avery, T.E., Berlin, G.L., 1992. Fundamentals of Remote Sensing and Airphoto Interpretation. Macmillan 1943-Avery, T.E.

Banskota, A., Wynne, R., Thomas, V., Serbin, S., Kayastha, N., Gastellu-Etchegorry, J., Townsend, P., 2013. Investigating the utility of wavelet transforms for inverting a 3-D radiative transfer model using hyperspectral data to retrieve forest LAI. Remote Sens 5, 2639–2659. https://doi.org/10.3390/rs5062639.

Campbell, J.B., Wynne, R.H., Thomas, V.A., 2023. Introduction to Remote Sensing, 6. edition. Guilford Press, New York.

Fairhead, J.D., 2003. Gravity and magnetics in today's oil and mineral industry. GETECH, School of Earth Sciences University of Leeds, UK.

Fernandez-Diaz, J., Carter, W., Shrestha, R., Glennie, C., 2014. Now you see it… now you don't: understanding airborne mapping LiDAR collection and data product generation for archaeological research in mesoamerica. Remote Sens 6, 9951–10001. https://doi.org/10.3390/rs6109951.

Kampes, B.M., 2006. Radar interferometry: persistent scatterer technique. Remote Sensing and Digital Image Processing. Springer, Dordrecht, the Netherlands.

Kruse, F.A., 2012. Mapping surface mineralogy using imaging spectrometry. Geomorphology 137, 41–56. https://doi.org/10.1016/j.geomorph.2010.09.032.

Kuenzer, C., Dech, S., 2013. Remote sensing and digital image processing, pp. 1–26. https://doi.org/10.1007/978-94-007-6639-6_1.

Marshall, M., Thenkabail, P., 2014. Biomass modeling of four leading world crops using hyperspectral narrowbands in support of HyspIRI mission. Photogramm. Eng. Rem. Sens. 80, 757–772. https://doi.org/10.14358/PERS.80.8.757.

McManamon, P.F., 2012. Review of ladar: a historic, yet emerging, sensor technology with rich phenomenology. Opt. Eng. 51. https://doi.org/10.1117/1.OE.51.6.060901.

Meerdink, S.K., Hook, S.J., Roberts, D.A., Abbott, E.A., 2019. The ECOSTRESS spectral library version 1.0. Remote Sens. Environ. 230, 111196. https://doi.org/10.1016/j.rse.2019.05.015.

Navalgund, R., Rajani, M.B., 2017. The science behind archaeological signatures from space. Curr. Sci. 113, 1859. https://doi.org/10.18520/cs/v113/i10/1859-1872.

Parcak, S.H., 2009. Satellite Remote Sensing for Archaeology. Routledge, London ; New York.

Rees, G., 2001. Physical Principles of Remote Sensing, second ed. Cambridge University Press, Cambridge, U.K; New York, NY.

Thenkabail, P.S., Lyon, J.G., Huete, A. (Eds.), 2012. Hyperspectral Remote Sensing of Vegetation. CRC Press, Boca Raton, FL.

Thenkabail, P.S., Mariotto, I., Gumma, M.K., Middleton, E.M., Landis, D.R., Huemmrich, K.F., 2013. Selection of hyperspectral narrowbands (HNBs) and composition of hyperspectral twoband vegetation indices (HVIs) for biophysical characterization and discrimination of crop types using field reflectance and hyperion/EO-1 data. IEEE J. Sel. Top. Appl. Earth Obs. Remote Sens. 6, 427–439. https://doi.org/10.1109/JSTARS.2013.2252601.

Thenkabail, P.S., Smith, R.B., De Pauw, E., 2000. Hyperspectral vegetation indices and their relationships with agricultural crop characteristics. Remote Sens. Environ. 71, 158–182. https://doi.org/10.1016/S0034-4257(99)00067-X.

Thorp, K.R., French, A.N., Rango, A., 2013. Effect of image spatial and spectral characteristics on mapping semi-arid rangeland vegetation using multiple endmember spectral mixture analysis (MESMA). Remote Sens. Environ. 132, 120–130. https://doi.org/10.1016/j.rse.2013.01.008.

Wynn, J.C., 1986. A review of geophysical methods used in archaeology. Geoarchaeology 1, 245–257. https://doi.org/10.1002/gea.3340010302.

Kokaly, R., Clark, R.N., Swayze, G.A., Livo, K.E., Hoefen, T.M., Pearson, N.C., Wise, R.A., Benzel, W.M., Lowers, H.A., Driscoll, R.L., Klein, A.J., 2017. USGS spectral library version 7 data. https://doi.org/10.5066/F7RR1WDJ.

Monika, Govil, H., Kumar, S., 2022. Subsurface feature identification using L band synthetic aperture radar (SAR) data over jaisalmer, India. In: Radar Remote Sensing. Elsevier, pp. 109–122. doi:10.1016/B978-0-12-823457-0.00007-0.